Use of small unmanned aerial system for validation of sudden death syndrome in soybean through multispectral and thermal remote sensing

by

Nicholle M Hatton

B.S., Kansas State University, 2018

A THESIS

submitted in partial fulfillment of the requirements for the degree

MASTER OF SCIENCE

Department of Biological and Agricultural Engineering
College of Engineering

KANSAS STATE UNIVERSITY
Manhattan, Kansas

2018

Approved by:

Major Professor
Dr. Ajay Sharda

Copyright

Abstract

Discovered in 1971, sudden death syndrome (SDS), caused by the fungus *Fusarium virguliforme,* has spread from the US to South American and European countries. It has potential to infect soybean crops worldwide, causing yield losses of 10% to 15% and even 70% in extreme cases. There is a need for rapid spatial assessment of SDS. Currently, the extent and severity of SDS are scored using visual symptoms as indicators. This method can take hours to collect and is subject to human bias and changing environmental conditions. Color infrared (CIR) and thermal infrared (TIR) imagery detect changes in light reflectance (visible and near-infrared bands) and emittance (canopy temperature), respectively. Stressed crops may show deviations in light reflectiveness, as well as elevated canopy temperatures. The use of CIR and TIR imagery and flexible aerial remote sensing platforms offer an alternative for SDS detection and diagnosis compared to hand scoring methods.

Crop stress and diseases have been detected using manned and unmanned aerial systems previously. Yet, to date, SDS has not been remotely assessed using CIR or TIR imagery collected with aerial platforms. The following research utilizes high throughput CIR and TIR imagery collected using a small unmanned aerial system (sUAS) to detect and assess SDS. A comparative evaluation of ground-based and aerial CIR methods for assessing SDS was conducted to understand the effectiveness of novel aerial SDS detection methods. Furthermore, a TIR case study investigating the use of potential thermal canopy changes for SDS detection was conducted to investigate the possibility of using TIR as an SDS indicator.

CIR reflectance measured from a ground-based spectrometer and sUAS was collected data over a two-year period. Ground-based spectrometer data were collected weekly, while a sUAS collected aerial imagery late in the growing season each year before plant maturity. Pigment index (PI) values were derived from ground-based and aerial data. Results showed a strong negative correlation between SDS score and PI values. Aerial and ground-based data both showed strong correlations to SDS score, however, aerial data displayed a stronger relationship possibly due to minimal changes in environmental conditions. High SDS scores correlated strongly to aerial derived PI ($R^2 = 0.8359$). Rapidly assessed high SDS allows for accurate screening of SDS critical for soybean breeding. The second year of the study investigated each component of SDS score, severity, and incidence. PI proved to have the best correlation with severity ($R^2 = 0.6313$ and $\rho =$

-0.8016) rather than incidence or SDS score. PI also correlated to SDS scores with $R^2 = 0.6159$ and $\rho = -0.7916$.

A sUAS mounted TIR camera collected imagery four times during the growing season when SDS foliar symptoms were just starting to appear. At the start of the study period, the correlation between canopy temperature and SDS is low ($\rho = -0.2907$), but increases over the growing season as SDS prevalence increases ending with a strong correlation ($\rho = -0.7158$). Early identification of SDS leads to the implementation of mitigation practices and changes in irrigation scheduling before the disease reaches severe symptoms. Early mitigation of SDS reduces yield loses for farmers.

The use of both CIR and TIR aerial imagery captured using sUAS can provide rapid spatial assessments of SDS, which is required by both producers and plant breeders. PI derived from CIR imagery showing strong correlations to SDS score reinforce the idea of replacing the time-consuming traditional ground-based systems with the more flexible, faster, sUAS methods. TIR imagery was shown to be reliable in assessing SDS in soybeans further establishing another possible aerial method for early detection of SDS.

Table of Contents

List of Figures

List of Tables

List of Equations

Acknowledgments

My research would not have been possible without the help and support of my friends and family. First, I would like to thank Dr. Ajay Sharda, my advisor. Dr. Sharda provided invaluable insight and guidance throughout the duration of my project. His dedication of time, resources, and knowledge provided allowed me to grow personally and professionally. I would also like to thank my committee members: Dr. William Schapaugh Jr. and Dr. Deon van der Merwe. Both provided physical resources and countless hours of knowledge and guidance through the duration of my project. I have thoroughly enjoyed the opportunity to work with both of them.

The Kansas Soybean Commission supports this work and associated reports and papers.

I would also like to thank my family for supporting my learning from childhood to now. They have always pushed me to become better and provided me with the resources to achieve my goals. I want to give a special thank you to my father, Chris Hatton, and husband, Blake Walter. My dad reviewed and edited my thesis for grammatical, spelling and organizational errors. He has also never stopped believing in me. My husband put up with many long nights and missed meals while I was working to finish data analysis or stuck in the field finish one more flight. Thank you for your patience and support.

Finally, I want to thank my Lord and savior for the opportunities and skills that he has granted me throughout my life to get me to this point.

Preface

All work presented in this thesis was conducted at Kansas State University in Manhattan, KS in the Biological and Agricultural Engineering Department. The following thesis chapters were written for direct submission for individual publication.

Chapter 1 - Introduction

Soybeans are major crops within the United States. In 2017, the harvest value of soybean crops across the United States was estimated at $40 billion according to the USDA. These soybeans have a huge impact on the farmers and their families. Disease plays a large roll in soybean production by limiting yield in infected crops. Many diseases affect soybeans such as root rot, rust, downy mildew, and sudden death syndrome (SDS).

SDS is a concern because it can cause large yield losses but it also opens the field for nematode infections (Xing & Westphal, 2009). SDS infections caused $1.6 billion in yield losses in 2016 (Manage soybean risks, SDS and SCN with ILeVO.2016) almost 4% of the harvest value was lost. Losses have seen growth since the disease was discovered in 1971 and more area is affected each year by the disease.

SDS poses a large threat to soybean production not only within the US but also South America, Africa, and Malaysia. The spatial extent of SDS is not fully understood. Father, SDS prevention, and mitigation practices are limited and can be ineffective. Therefore, there is a need for rapid spatial assessment of SDS to understand the spatial extent of the disease, early symptom expression of the disease and early implementation of mitigation practices and the effect on yield. SDS has not been effectively evaluated for quantification of disease symptoms from an aerial platform. Small unmanned aerial systems (sUAS) could be used for the quantification of SDS.

Through the use of sUAS rapid spatial assessment can be achieved.. sUAS offer a flexible platform that can cover large amounts of area in a short amount of time but just as efficiently cover small areas. The high flight efficiency could be easily adapted to large-scale applications.

With the flexibility and adaptability of sUAS, a study was designed to quantify SDS on a spatial and temporal scale. The data gathered could be used to further develop breeding practices and for early implementation of SDS mitigation practices by farmers to minimize yield loss

The objective of this work is to develop systems and methods for the rapid spatial assessment of SDS in soybean. Modified broadband color infrared (CIR) and thermal infrared (TIR) sensors mounted to a sUAS will be used for assessment. One study will be conducted with each of the sensors. The following objectives were established for the research conducted over the two studies described above and included in this paper:

1. Determine if PI can be used for the assessment and quantification of SDS and assess the validity of each component of SDS score
2. Compare validity and accuracy of ground-based and aerial remote sensing methods for scoring of SDS to determine benefits of aerial remote sensing of SDS
3. Assess the use of PI for determination of maturity
4. Use a TIR sensor to assess plant health and vitality
5. Evaluate canopy temperatures over the growing season to quantify disease development

Chapter 2 - Multispectral remote sensing for vegetated areas: A review

Abstract

Remote sensing gathers data through monitoring and detection of an area by measuring reflected light and emitted radiation. Remote sensing is particularly important for precision agriculture, vegetation mapping, and land use assessments. Precision agriculture utilizes remote sensing for assessment of water stress, plant nutrients, disease, and photosynthetic activity. Land use assessments evaluate current and historical land use to better understand land use modifications occurring as the result of the anthropogenic or environmental change. Vegetative indices derived from remote sensing practices aid in the understanding of plant communities. These indices compare different portions of the electromagnetic spectrum for the assessment of plant health and vitality. Satellite, aerial, and ground remote sensing systems can achieve similar functions but produce very different data functions. The intended data product must be taken into consideration when choosing between the different platforms. This paper reviews remote sensing as it relates to its use for vegetative studies, examines different remote sensing platforms, and evaluates a variety of remote sensing applications.

Introduction

Remote sensing has enhanced many aspects of vegetation assessment including precision agriculture, field and stream monitoring (Flynn & Chapra, 2014) and forest reclamation (Ribeiro et al., 2018). The often fast-changing environments that remote sensing serves requires assessment methods that produce rapid, reliable, accurate and applicable data. Remote sensing allows for a noninvasive rapid assessment of specific areas through measuring the reflected and emitted radiation.

Remote sensing can be used at small spatial scales for monitoring health or water stress in plants (Jones et al., 2009; Suárez et al., 2008), large scales to assess burning patterns in the Amazon (Ribeiro et al., 2018) and change in wildlife behavioral patterns through the assessment of forest structure (Singh et al., 2018). Remote sensing assessment platforms range in size from a small-unmanned aerial system (sUAS) to a satellite with each platform possessing different sensing

capabilities and data collection procedures. Thus, the type of platform utilized is highly dependent on the desired outcome and study goals.

All remote sensing platforms have the ability to produce the same results even though their data collection methods vary. All remote sensing platforms can aid in the assessment of crop health. This becomes particularly important to farmers as the demand to feed a growing population increases causing farms to increase production. Remote sensing allows farmers and researchers to evaluate their crop and the effects water, nutrients, disease and other factors have on crop growth and yield. Through vegetative indices, farmers and researchers can assess and develop crops that are more drought and disease resistant producing higher yields (H. Zhang et al., 2017).

Vegetative indices are developed from the reflected radiation detected by remote sensing systems. Multispectral imagery is particularly suited for vegetative indices derivation as it can be altered for specific indices based on the platform sensor. Multispectral imagery is the process of measuring the reflectance across a given light (spectral) range. Indices calculated from reflectance measurements are used to evaluate vegetation and applied to improve management practices and track developmental or environmental changes. This literature review focuses on multispectral remote sensing as it relates to vegetation and vegetative areas and the large influences that multispectral remote sensing has had on precision agriculture and plant studies.

The following sections will review multispectral remote sensing relating to vegetation beginning with a fundamental understanding of the electromagnetic spectrum as it relates to vegetation. The establishment of the framework for remote sensing beginning with an understanding of resolutions followed by calibration and correction techniques and ending with the platforms used to complete remote sensing work will be discussed. Finally, applied remote sensing is reviewed beginning with vegetative indices and ending with a wide range of remote sensing work from past studies.

Fundamentals of light reflectance

Material objects naturally reflect, absorb, and transmit different regions of the electromagnetic spectrum at varying magnitudes. Remote sensing is particularly interested in measuring the amount of reflected light. The magnitude of reflectance depends on the physical and chemical composition of the target. Reflected light in the visible spectrum allows for the observation of color as detected by the human eye. Reflectance in the nonvisible region helps to infer, in the case of biological material such as plants, an understanding of processes, e.g. photosynthesis, homeostasis,

senescence, developmental stage. Measuring these reflectance patterns through the visible and color infrared (CIR) regions assessment of the vegetation health.

Collecting data from wavelengths outside the visible spectrum provide a broader range of information about a given subject. Infrared is particularly useful because vegetation is known for reflectance in the short-wave infrared (SWIR), near-infrared (NIR), and middle infrared (MIR) regions of the electromagnetic spectrum. Many vegetation studies focus on this region to assess plant health and vitality (Ali et al., 2017; Huang et al., 2010b; Lück-Vogel et al., 2016; Singh et al., 2018). Vegetation indices rely on CIR (encompassing both the SWIR, NIR, and MIR regions) as well as the visible wavelengths to generate ratios for the understanding plant health, vitality, and soil moisture to name a few (Ali et al., 2017; Huang et al., 2010b; Suárez et al., 2008).

Reflectance curves can vary greatly for plants. Differences in plant health, developmental stage, and genotype will cause reflectance variations across the electromagnetic spectrum. Healthy green vegetation exhibits a small peak in reflectance from 500 to 600 nm producing the characteristic green color. Healthy plants reflect very strongly in the NIR and MIR regions creating a plateau from 700 to 1300 nm with a slightly lower plateau from 1500 to 1800 nm (Chappelle et al., 1992). Plateaus occur because of the low absorbance by the pigments and subcellular particles as well as scattering occurring in the mesophyll cell wall (H. W. Gausman, 1977; H. W. Gausman, 1974; Slaton et al., 2001). There are two major dips in the curve at 1400 nm and 1900 nm where water absorbs the incoming light. Studying the amount of light reflected provides information that is used for identification of plant type and evaluation of plant nutrient and health requirements. For example, healthy green vegetation will express a very different reflectance curve compared with the same vegetation that has become water stressed or diseased (Datt, 1999; Garcia-Ruiz et al., 2013; Suárez et al., 2008; Yang et al., 2010). Reflectance patters from 400 to 1300nm not only reveal plant health but can also determine weed presence within a field (Tamouridou et al., 2017).

Plant health and maturation can be determined by analysis of the reflection of light caused by certain pigments within the plants. For instance, the pigments responsible for the plant's photosynthetic abilities, chlorophyll a and b, strongly absorbs wavelengths of 400-500 nm but reflects wavelengths of 500-600 nm. This pattern indicates healthiness among plant communities.

Other pigments commonly used in determining plant health, carotenoids and anthocyanin absorb and reflect similar wavelengths. The presence of these pigments indicates the degeneration of chlorophyll and onset of senescence. Studying the reflectance of pigments with plants allows

for the understanding of plant health and vitality. Application of pigment knowledge helps the user assess plant and crop growth.

Resolutions

Resolution is a key measure of performance in remote sensing. The resolution required to evaluate a subject largely determines the type of platform selected. Resolution measurements are divided into four categories: temporal, spatial, spectral, and radiometric. Resolution will vary based on the remote sensing platform and study area. Rarely, is there a sensor considered ideal for all spatial scales.

Temporal resolution

Temporal resolution assesses the rate at which remote sensing takes place. Remote sensing projects can range from a single data collection event to weekly data collection and in some cases, a year or more will elapse between data collection events. The time between data collection events is critical for accurate results. This is particularly important when considering the use of satellite imagery over a period, such as a plants growing season. Temporal resolution can affect the ability to monitor a process, behavior or treatment over a designated time (i.e. 3 weeks, 1 year or 10 years). Weather, technology limitation, and environmental factors can influence temporal resolution.

Weather can substantially limit the number of usable of images satellite imagery, in particular, are subject to weather influences. Satellites maintain a fixed orbit and as a result, revisit times can range from 3 days to 16 days. This can cause extended periods (months) where cloud cover interferes with imagery and renders the data unusable.

Manned aircraft and sUAS do not have the same temporal resolution restrictions that can restrict the use of satellite imagery. Manned aircraft and sUAS flight offer unique flexibility tied only to the pilot's schedule and local weather conditions. Likewise, Berdugo et al. (2014) utilized the temporal advantage of sUAS to determine the first signs of disease on cucumber leaves. Inoculated leaves were imaged every four days to determine the first emergence of symptoms. Barnes et al. (2000) utilized weekly imagery to assess the difference between nitrogen and water stress in cotton.

Spatial resolution

Spatial resolution is critical in capturing detail within an image. The sensor size (number of available pixels) and the distance between sensor and target to establish the potential spatial resolution. The calculated spatial resolution, based on distance from image sensor to target and sensor size is a theoretical maximum influenced by the image quality of the camera. For example, a camera not in focus is not capable of reaching the calculated spatial resolution because pixels are indistinguishable from one another. Pixels must be distinguishable from one another to reach the maximum spatial resolution. For the same sensor size (and in focus camera), the more area imaged the coarser the resolution will be. Thus, high altitude flights will have a lower resolution compared to low altitude flights given the same sensor array.

Low altitude flights with a sUAS can reach sub-centimeter resolutions, whereas satellites are limited to kilometer or meter resolutions. Spatial resolution is a key consideration when determining the platform, based on studies spatial scale. For small-scale studies interceded in individual plant leaves, a very fine resolution will be required. In contrast, large-scale or continental, vegetation monitoring will utilize more coarse imagery.

Spectral resolution

Spectral resolution refers to the sensors ability to detect specific wavelength ranges of the electromagnetic spectrum. The addition of filters changes the wavelengths of light that interact with the sensor to record images. Cameras, multispectral and broadband, can cover a variety of wavelengths depending on the filters applied to the sensor and the sensor material. Multispectral and broadband sensors often cover visible and NIR ranges, from about 400 nm to 1150 nm. Multispectral and broadband sensors can detect a minimum of two wavelength ranges, or bands, within a larger wavelength range, such as the NIR or visible region. An important distinction exists between multispectral and broadband cameras. Multispectral cameras sense discrete bands. Broadband cameras use overlapping bands with different peak sensitivities to generate color information over relatively wide spectral ranges (e.g. the whole visible spectrum). Common multispectral camera includes five band cameras (i.e. Mikasense) and OEM cameras, while most consumer cameras are broadband cameras. Broadband cameras can be modified by using filters.

Modified cameras can have practical advantages over multispectral cameras, including relatively low cost, high image quality, and user-defined options. Modification involves removing

IR blocking filters and installing filters that block specific spectral regions. Removal of filters can allow the full potential spectral range, including the NIR region, to interact with the sensor. Adding filters can block specific spectral regions, such as the region that normally registers in the red or blue channels of an unmodified camera. Those channels can then be used to register NIR light.

Five band and OEM multispectral cameras capture each band individually and can be used to form a final composite image that has distinct spectral bands for each channel. This can allow for the use and assessment of more types of indices, including the replication of indices traditionally generated from satellite images, or indices that target the transition between visible red and NIR referred to as the "red edge". However, disadvantages of multispectral cameras include higher cost, complexity associated with combining bands from separate sensors into a single image, and the relatively low signal to noise ratio associated with lower numbers of useable photons in narrow spectral bands compared to broad bands. Multispectral cameras often compensate for the lower photon numbers in narrow spectral bands by using low pixel density sensors that provide more surface area for each pixel.

Radiometric resolution

Radiometric resolution is an important consideration when determining the level of detail desired in the image. Radiometric resolution is a measure of the sensors ability to capture the number of distinguishable values in channel or band, represented as a bit. An 8-bit image will have 256 (2^8) values per channel while a 16-bit image will have 65,536 (2^{16}) values. The bit count or channel value is a theoretical maximum. Noise within the system does not allow the full range to be met. The signal to noise ratio determines the usable range within each band. Increasing the signal to noise ratio and thus the radiometric resolution can be done by manipulating three aspects of the camera: aperture, shutter speed, and sensor size. Often in remote sensing, the shutter speed has a maximum speed to achieve a clear image with no blur thus manipulation of aperture and sensor size achieve higher signal to noise ratios.

The larger the radiometric resolution, the larger the data storage requirements. Many satellites have between 8 and 14 bits of potential resolution. In contrast, ground deployed systems have lower potential radiometric resolutions of 8 bits or fewer. Technological change continues to support improved radiometric resolution and radiometric properties of sensors.

Radiometric resolution can have an effect on vegetative indices and vigor maps generated from satellite and aerial platforms. Radiometric differences in platforms are not negligible (Borgogno-

Mondino et al., 2018). Strong differences in NDVI and enhanced vegetation index (EVI) for 8-bit and 11-bit satellite imagery show the importance of radiometric resolution (Alonso et al., 2017). Certain wavelengths exhibit significant differences in radiometric resolution. Alonso et al. (2017) found significant differences in blue and green bands when comparing 8-bit and 11-bit imagery. They also found that red and NIR band were not statistically different. The effect radiometric resolution has on specific bands is an important consideration when determining platform and vegetative index for a study.

Calibration and correction in multispectral imagery

The remote sensing process collects data from the three-dimensional (3D) world and projects them on to a two-dimensional (2D) surface. Calibration is therefore required when projecting the 3D world on to a 2D surface so that the geometric measurements are accurate. Inherent distortions in the collected image require correction to compensate and improve data usability. Sensor noise, atmospheric interference, and lens distortion are other common challenges that require correction.

Noise calibration

Noise is random and systemic errors caused by inaccurate sensor measurements generated autonomously during data collection (Al-amri et al., 2010; J. Kelcey & Lucieer, 2012a; J. Kelcey & Lucieer, 2012b; Mansouri et al., 2005b). Bias in the value and spatial properties cause systemic noise. Systemic noise is predictable and repeatable making it easier to recognize and calibrate. Random noise, in contrast, varies over time and is not reproducible or associated with data or the system. Random noise is nearly impossible to isolate because of its inconsistencies and variation. Corrections are usually applied to offset the amount of noise rather than removal of noise because of the unpredictability of random noise and removal risks altering valid data collected. Dark offset subtraction is commonly used for the offset of noise (J. Kelcey & Lucieer, 2012a; J. Kelcey & Lucieer, 2012b) produced by specific hardware.

Dark offset subtraction

Dark offset subtraction is an image-based approach of reflectance calibration that exploits the difference in signal produced from the camera. The method provides a per-pixel noise estimation by recording variation without incoming light (J. Kelcey & Lucieer, 2012b). Subtraction of the value gathered using dark offset is applied to compensate for the effect of noise on reported reflectance values.

Two methods are used for dark offset subtraction; the first utilizes artifacts within captured images the second capture images in a dark room for calibration. Once an image is captured, black objects within the image can be used to calibrate the noise. The black object's values are measured in each channel and the average for each channel is then subtracted from the remaining pixels in the image to offset noise. The second method of dark offset subtraction requires complete darkness to measure. A dark room with a Gore-Tex hood can be used to eliminate light (J. Kelcey & Lucieer, 2012b) for optimal noise measurement. Each channel or band of the equipment must have imagery generated and noise estimated. Multiple images are collected at a set exposure and averaged to create a per pixel subtraction offset (J. Kelcey & Lucieer, 2012b). Subtraction of the average offset in each channel from the desired image achieves the final reflectance calibration. It is important to remember that this method must be repeated when introducing new system hardware.

Vignette

Vignetting occurs from the uneven distribution of light throughout an image. It begins at the principal point (center) and extends radially to the edges of the image. The stronger the angle of incoming light the stronger the effect (J. Kelcey & Lucieer, 2012b). The aperture and focal length are major contributors to the severity of the vignette as they determine how light reaches the sensor. Smaller apertures and longer focal lengths allow for sharper angles causing less light to reach all points of the image; thus, producing the vignette effect. Vignetting can be corrected using image-based correction or modeling of the optical pathway (J. Kelcey & Lucieer, 2012a).

Image-based corrections or flat field derived correction look-up tables are based on per pixel values of correction (J. Kelcey & Lucieer, 2012a; Yuanjie Zheng et al., 2009). Flat fields exhibit Lambertian properties (Mansouri et al., 2005a). This method is simpler and provides a more accurate correction to the image than modeling the optical pathway. Image-based corrections assume the brightest pixel (at or near the principal point) exhibit the true radiance measurement (J. Kelcey & Lucieer, 2012a). Kelcey and Lucieer (2012a) describe the equations and methodology for creating the correction using a white artist canvas as the Lambertian surface. Optical pathway modeling uses sensor characteristics and light interaction to model how light disperses across the sensor to produce the vignette. The results can be applied to imagery to eliminate the vignette effect.

Atmospheric correction

Atmospheric correction is required for any instance where large amounts of atmosphere are between the camera lens and the target. This effect is especially pronounced for satellite imagery. Rayleigh, Mei, and non-selective scattering occur from lights interaction with atmospheric particles. This can lead to distortions and affect the recording of specific wavelengths by the sensor. Absorption, scattering, and refraction of light can be additive or multiplicative of atmospheric effects causing major distortions in an image. All three effects are wavelength dependent. Scattering affects shorter wavelengths more (specifically Rayleigh) than longer wavelengths. Transmittance, caused by both scattering and absorption, has a multiplicative effect that can be difficult to correct for (Chavez, 1996). Absorption, scattering, reflectance, and transmission of light are all location and atmospheric condition dependent. Because conditions change quickly it is important to consider the time of year, location, and atmospheric and environmental conditions when working with imagery.

Radiative transfer codes

Radiative transfer codes (RTC) are an atmospheric correction method based on sensor measurements, such as optical depth and zenith angle recorded at the time of imagery collection. RTC creates a relationship between the surface reflectance and radiance at the sensor allowing for accurate correction. This measurement procedure requires expensive equipment and is time-consuming. The procedure cannot be used on historical data or data from different locations unless RTC were taken at the time of imaging (Moran et al., 1992).

Substitution of RTC with simulated atmospheric data based on time of year and geographic location is possible in certain instances. In other cases, derived data from the image itself acts as a substitution to the RTC. Both methods depend on the imagery and are less accurate than collecting RTC data during image collection (Moran et al., 1992).

Dark object subtraction

A second atmospheric correction is dark object subtraction (DOS). This method first introduced by Vincent (1972) is an image-based method of deriving atmospheric data and is commonly used for visible bands (Chavez, 1996). DOS allows for extraction of path radiance based on the darkest object in an image. Ideally, the object would be completely and perfectly

black. This condition, however, does not occur in nature and a one-percent minimum reflectance is assumed (Chavez, 1996; Vincent, 1972).

DOS ignores the transmittance and downwelling irradiance that is required for RTC correction. Moran et al. (1992) found that in some cases the DOS method causes more error than an uncorrected image. The low accuracy of the DOS method results from correction of additive scattering only, while disregarding multiplicative transmittance. DOS is not suitable for medium to bright reflectance values and when reflectance values exceeded 15%, the accuracy of the model is no longer acceptable (Chavez, 1996).

DEF TAUs and COST

The DEF TAUs and COST model is an image-based atmospheric correction method that derives the multiplicative transmittance effect using two techniques, developed by Chavez (1996). The first technique (DEF TAUs) uses the solar zenith angle, optical thickness, and the viewing angle to generate an empirical relationship. The range for the solar zenith angle is 30 to 55 degrees. The second technique (COST) takes the cosine of the solar zenith angle, substantially improving the DOS method. Both methods generate accuracies similar to RTC correction without the equipment expense. This method has been found to have an error of approximately 30%. The COST model has been proven accurate in semi-arid/arid environments (Chavez, 1996).

Radiometric calibration and correction methods

Radiometric calibration is a calibration technique for the measurement and detection of electromagnetic radiation. Artifacts, gain, and inconsistencies within the sensor or sensor surface cause inaccurate reflectance data implicating the need for radiometric calibration. Radiometric calibration occurs in three instances: preflight, onboard/airborne, and vicariously. The preflight calibration looks specifically at the sensors. Airborne calibration implements checks during image acquisition and vicarious calibration involves radiance and reflectance for field operations (Dinguirard & Slater, 1999). Calibration ensures that the hues maintain the same digital number (DN) within the image and from image to image.

Empirical line

The empirical line method is a radiometric calibration method that does not require atmospheric data. The alternative calibration methods, at the time of the empirical line methods development, required atmospheric data collection. Historical atmospheric data cannot always be

obtained. The empirical line method operates on the assumption that targets within the image have different reflectance characteristics over a large spectral range (Smith & Milton, 1999). This image-based radiometric correction method identifies the relationship between DN values and the reflectance of a given target (J. Kelcey & Lucieer, 2012b). The method is difficult to apply because illumination and atmospheric effects must be considered for each waveband. The empirical line method does not take into consideration bi-directional reflectance which can cause inaccurate data (Smith & Milton, 1999).

Targets can be any object that is smooth, flat, and bare such as natural objects like snow, or manmade objects like roadways or survey panels. Optimal targets produce minimal error and have low spectral variation over all wavelengths. Other materials such as concrete and asphalt can cause contamination-reducing reflectance. One target is required to utilize the most simplistic form of the method and to assume that "zero reflectance will produce zero radiance at the sensor and there is a linear relationship between radiance and reflectance" (Smith & Milton, 1999). One target is, however, not ideal because the simplistic approach results in errors ranging from 15% to 20%. If there is a large spectral contrast between them, the use of two targets decreases the error while also eliminating the assumption of linearity. The use of four targets is ideal reducing error to a few percent and displaying the nonlinearity that exists in each waveband (Smith & Milton, 1999).

Linear calibration and correction methods

Linear calibration and corrections are beneficial to improving data quality because nonlinear optimization is not required. All intrinsic and extrinsic model parameters become linear when ignoring lens distortion. Many of the models are matrix transformations and solved with a least square solution. Linear correction has been further developed to include lens distortion resulting from geometric inaccuracies. However, consideration of lens distortion converts linear corrections into nonlinear optimizations. Linear corrections also have many unknown variables, which exceeds the degrees of freedom. This can limit the accuracy in noisy circumstances because of the erroneous combination of parameters.

Direct Linear Transformation (DLT)

First developed by Abdel-Aziz and Karara (2015), DLT is a linear calibration and correction method based on a pinhole camera model, which ignores nonlinear components, such as lens distortion. DLT uses a two-step approach commonly applied to metric and non-metric

photogrammetry. The first step transforms the comparator coordinates to image coordinates to calibrate and measure the fiducial marks. The second step transforms the image coordinates to object coordinates by utilization of a homogeneous 3 x 4 matrix and iterative solution. Typical errors that occur when applying this method include uncertainties in comparator measurements and object space coordinate error for control points. The method also does not consider radial and tangential lens distortion and the method experiences errors in the iteration criteria and neglecting of second and higher terms in the linearization (Abdel-Aziz & Karara, 2015; Heikkila & Silven, 1997).

Sutherland

Sutherland (1974) developed a linear correction method utilizing a five-step procedure for outlining the conversion of a 3D perspective into 2D image coordinates. The method utilizes a large tablet for the use of multiple views of an object. Two pens are used to infer the view used and apply transformations to derive a 3D image from the points indicated in the 2D image. Several views of an object generate the 3D view. This method has been applied successfully in graphics applications (Sutherland, 1974).

Yakimovsky and Cunningham

Yakimovsky & Cunningham (1978) developed a linear correction method using an accurate 3D measurement from a pair of stereo cameras. The Mars rover and remote processing system applied this method. The method assumes that the cameras are geometrically linear. Lens distortion is ignored because of the highly-linear lens and large object distance and an accuracy of +/- 5mm at 2 m were reported (Yakimovsky & Cunningham, 1978).

Non-linear calibration and correction methods

Nonlinear calibration and corrections methods allow for easy adaptation and accuracy for complex models. Nonlinear models are complex and require several iterations after valid initial estimates in order to obtain results (Tsai, 1987). These correction methods, in contrast, can produce a RMS accuracy of 0.1 mils (Faig, 1975). Several techniques exist to complete nonlinear corrections presented below.

Faig (1975) develop a nonlinear calibration and correction method that utilized 17 unknowns for each photo analyzed. The high number of unknowns led to a very high accuracy for his final

images.* A high accuracy was obtained because large high-definition image allows for higher resolutions than those possible with a solid-state charge-coupled device (CCD) (Faig, 1975).

Adjustment of the direct linear method to a nonlinear method occurs if lens distortion is considered. In the original model (as mentioned in linear calibration), ignoring lens distortion allows a linear model to be formed (Carbonnell et al., 1979). Sobel (1974) develop a method and describe 18 optimization parameters using nonlinear equations. His method is similar to that developed by Faig.

Lens correction

Lens distortion often referred to as geometric correction and is caused by lens imperfections, misalignment of the lens and sensor, or misalignment of compound lenses. Lens distortion affects the physical geometry of the image rather than the radiometric qualities of the image as seen types of distortion.

The physical nature and correction methods of the lens distortion requires that it be the last applied correction (Del Pozo et al., 2014). Misalignment of compound lenses can create color aberration. This occurs when the focal planes for each wavelength of color is slightly offset causing color shifts and sometimes halos to appear throughout the image. The only solution for this is replacement of the lens.

Lens distortion can also result in geometric shifts in the resulting image. This distortion can be viewed two ways, radially and tangentially (J. Wang et al., 2006). Radial distortion occurs when the object appears shifted closer (negative displacement) to or further (positive displacement) from the center of the image (J. Kelcey & Lucieer, 2012a). Tangential distortion occurs primarily because of sensor misalignment resulting in a planar shift (J. Wang et al., 2006). Correction of lens imperfections and lens/sensor misalignment can typically be accomplished with the Brown-Conrady model (Prescott & Mclean, 1997; J. Wang et al., 2006).

The Brown-Conrady corrects for radial and tangential distortions by considering the intrinsic and extrinsic coefficients of the sensor (De Villiers et al., 2010; J. Kelcey & Lucieer, 2012a; J. Kelcey & Lucieer, 2012b; J. Wang et al., 2006). Intrinsic properties are specific to the sensor of the camera while extrinsic properties take into consideration the three-axis orientation and spatial position of the camera (Del Pozo et al., 2014). The correction utilizes a board with known geometric features, which serves as a calibration panel for the distortion assessment. Sensor

coefficients arise from calculations of the known panel properties and properties produced by the lens and sensor system (J. Kelcey & Lucieer, 2012a; J. Wang et al., 2006).

Other calibration and correction methods

A less frequently used calibration method corrects for asymmetric projections commonly used for circular features, but also easily applied to any shape. Heikkila and Silven (1997) introduced the correction method while describing their calibration method. The principal is simple, two and three-dimensional objects distort when projected on to a non-zero plane. The angle and displacement between the object and the surface are major factors that lead to the distortion. The only time that distortion does not occur happens when both the image and plane are parallel (Heikkila & Silven, 1997). Perfectly parallel flight is often not practical or possible, as only the principal point will achieve this (assuming the camera is parallel with the earth when taken), and therefore other areas in the image will have slight distortions. The distortion may be small, but they can have a great impact on the final product (Heikkila & Silven, 1997).

A second less common calibration method is the two-plane method. The two-plane method differs from pinhole models in the fact that lines of sight are not projected through the same point of the lens center. Two points from the image plane are computed in separate calibration frames. Independent formulas are used to calculate a calibration for each plane. Intrinsic parameters including linear, quadratic, and linear spline are not required for this calibration method. The linear method expresses a linear combination of image coordinates using a minimum of three points per plane. Quadratic methods take a second order approximation for each plane utilizing a minimum of six points per plane. The linear spline method uses the closest three points per plane to create a triangle of the point to be interpolated. The vertices compute a local linear approximation per plane. Each method requires a minimum of 12 parameters per plane with the exception of the quadratic, which requires 24 parameters. The linear spline and quadratic methods produce the best results. The methods, however, are empirical and require a large number of parameters to complete the calibration (Izaguirre et al., 1987; Martins et al., 1981).

Tsai (1987) developed a method that uses a four-step pinhole method transformation for calibration from the 3D world to computer image coordinate. This is a simple nonlinear optimization with only four parameters required to capture lens distortion (Tsai, 1987). The first step consists of rigid body transformation from the object world coordinate system to the 3D camera coordinate system. The second step is the transformation from the camera 3D coordinates

to the ideal image coordinates using the perspective projection. A radial lens distortion correction is applied and then finally a real image coordinate to computer image coordinate conversion is applied resulting in the final image.

Platforms

The versatility of remote sensing allows users to select from a suite of platforms, each capturing imagery and producing data products unique to that system. Which platform to use, requires prior knowledge of the platform's capabilities, data product characteristics, and the limitations of both platform and data product. Remote sensing platforms can range from satellites arranged in carefully coordinated groups or constellations, to sUAS or at its simplest form ground systems. There are several major factors to consider when selecting a platform. Some of which include:

- End goals of the work
- Spatial scale
- Altitude
- Spatial resolution
- Spectral resolution
- Temporal resolution

Platform sensors can have varied resolution and no one sensor can capture a combined maximum spectral, spatial, and radiometric resolution. Typically, the higher the spatial resolution, the lower the radiometric resolution. Satellites, for example, have high radiometric and spectral resolutions but decreased spatial resolution. Maximization of the essential resolutions for the project is important.

Remote sensing platforms can be categorized into satellite, aerial (manned or unmanned), and ground systems. Before selection of a platform, it is important to understand the general set up, advantages, disadvantages, and data product of each category. Presented below is a detailed discussion of satellite, aerial (manned and unmanned) and ground methods of remote sensing methods.

Satellite

Satellite remote sensing has developed from a single satellite to several satellites creating constellations that work together to deliver imagery through the visible, IR, and thermal regions of the spectrum. Satellite coverage varies greatly among different systems. MODIS satellites cover

the entire world in a single day, but with a coarse spatial resolution. Whereas, moderate resolution satellites, such as Landsat, have a revisit time of 16 days. Satellites are equipped with two scanner types, referred to as across-track and along-track.

Across-track scanners, the most common scanner used in today's satellites, operate using a single sensor and mirror that oscillates perpendicular to the direction of travel. These types of scanners are common because of the wide range of sensors available and high spectral resolution. These scanners, however, require a substantial amount of power to operate to maintain the correct oscillation speed and frequency. The mechanical nature of these scanners makes them prone to failure and mirror distortion. Landsat 7 is a great example of an across-track scanner failure. Since 2003, Landsat 7 has operated with a broken scan line corrector (SCL) (U.S. Geological Survey, 2017). The SCL compensates for the forward movement of the satellite in the calibration of the images. The resulting images, without the SCL correction, have missing data on the outside edges as seen in Figure 2.1. Corrections for this error occur with manual manipulation of the image, but overall the resulting data and images are less accurate data.

Along-track sensors contain multiple sensors aligned linearly. These sensors are stationary while collecting data along the flight line of the satellite. They allow for finer resolution, consume less power, and lack mirror distortion common with across-track scanners. They have a limited spectral range and require cooling to produce accurate images. The physical limitations of data collected in the spectral range make them less desirable than those collected with an across-track scanner.

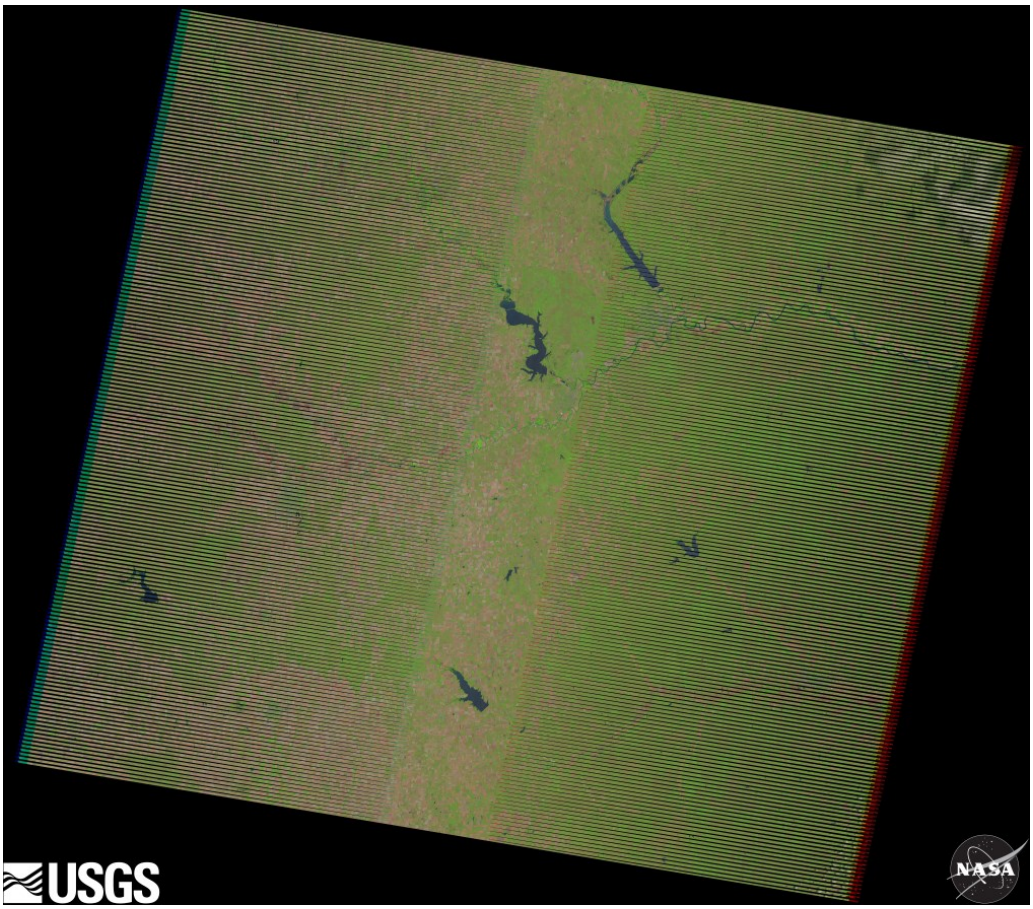

Figure 2.1 - Example of Landsat 7 failure (Courtesy of the U.S. Geological Survey)

Variation in sensor type and resolution characteristics makes satellite platforms versatile remote sensing tools. Table 2.1 presents several satellite platforms and their specifications including spatial, spectral, radiometric, and temporal resolutions.

Table 2.1 Satellite Platform Summary

PLATFORM TYPE	PLATFORM	SPATIAL (M)	SPECTRAL (BANDS)	RADIOMETRIC (BITS)	TEMPORAL (DAYS)	MAJOR APPLICATIONS
LANDSAT	Landsat 8	30 - MSS 15 - pan	9	16	16	-water consumption -agriculture -land use
SPOT	SPOT 7	6 - MSS 1.5 - pan	5	12	1	-disaster response -natural resource exploration
AVHRR	NOAA – 14	1.09	6	10	14/day	-cloud cover -surface temperature
MODIS	EOS Terra Aqua	1-2: 250 3-7: 500 8-36: 1000	36	12	16	-global phenomena observation
ASTER	EOS Terra Aqua	1-3: 15 4-9: 30 10-14: 90	14	Bands 1-9: 8 Bands: 10-14: 12	16	-global phenomena observation
MISR	EOS Terra Aqua	500-1000	4	14	16	-global phenomena observation
GEOS	GEOS – 8	3.2 - MSS 0.82 - pan	Visible/ NIR/pan	11	3	-mapping natural resources, natural disasters, agriculture, forestry, and mining
IKONOS	IKONOS	3.2 - MSS 0.82 - pan	Visible/ NIR/pan	11	3	-mapping natural resources, natural disasters, agriculture, forestry, and mining
QUICKBIRD	QuickBird	2.62 - MSS 0.65 - Pan	5	11	1 - 3.5	-land use -agriculture -forest analysis
GEO-EYE	GEO-EYE – 2	1.36 - MSS .034 - pan	Visible/ NIR/pan	11	3	-local processes observation
WORLDVIEW	WorldView – 3	1.24 - MSS 0.31 - pan 3.7 - SWIR	Pan 8 MSS, SWIR 12 CAVIS	11 - Pan &MSS 14 - SWIR	4.5	-local geological observation -human phenomena observation

Satellites have been collecting imagery since the early 1970's. This has allowed for long-term global and regional studies such as those concerned with vegetation change, climatic variability, and temporal changes to in land use to name a few (Lamchin et al., 2018; C. Wang et al., 2018). The quality of data collected by satellites are highly dependent on weather conditions. Cloud coverage often hinders a satellites data collection rendering some imagery useless. They also do not provide very high-resolution imagery in the sub-centimeter range, due to the coarse spatial resolution. The finest spatial resolution available from a satellite platform is several meters/pixel (1.24m/pixel as seen in Table 2.1). This spatial resolution does not make it ideal for crop detection or studies that require spatial resolution of centimeters/pixel. Coarse resolution imagery is ideal for large-scale surveys studying land use change, vegetation dynamics, or seasonal hydrology. Satellite imagery is also used for natural disaster response and global observation of cloud cover, human phenomena, and use of natural resources.

Aerial

Aerial platforms operate within the Earth's atmosphere. They do not require the atmospheric corrections as that of satellite imagery because of closer proximity to the earth's surface. Flight altitude highly is variable, although high altitude flights can require atmospheric correction. Aerial platforms are more flexible than satellite imagery because of their sole reliance on the pilot's schedule rather than a fixed orbit and revisit time. Aerial platforms provide a flexible and reliable platform for studies ranging from a few hectares to thousands of hectares.

Manned

Manned systems range from balloons to small aircraft to blimps. Used for studies assessing the vegetation characteristics, soil moisture, and thermography, manned aerial systems are very versatile (Huang et al., 2010b; Matese et al., 2015; J. Primicerio et al., 2012a; Yang et al., 2010). Long flight times covering large areas, while also maintaining a very high spatial resolution are a few advantages manned aerial systems have over satellites. Many of these systems, however, have high costs associated with flight demands, such as licensing, equipment, and fuel. Flight times can also be highly dependent on scheduling and weather conditions. Many researchers or farmers cannot afford a plane or balloon of their own; as a result, the manned aircraft is hired or shared among many researchers or farmers.

Unmanned

sUAS's lightweight design, maneuverability, and versatility have made them ideal for military use for many years. Within the last 10 years, sUAS have become readily available and affordable for the public with a wide range of capabilities (Salami et al., 2014). Precision agriculture has had several years of success with sUAS in everything ranging from determining the Normalized Difference Vegetation Index (NDVI) to monitoring the relationship between the spatial arrangements of shrubs and disturbance gradients (Mitchell et al., 2012; J. Primicerio et al., 2012a). The public has embraced the endless capabilities of sUAS and their continually developing applications.

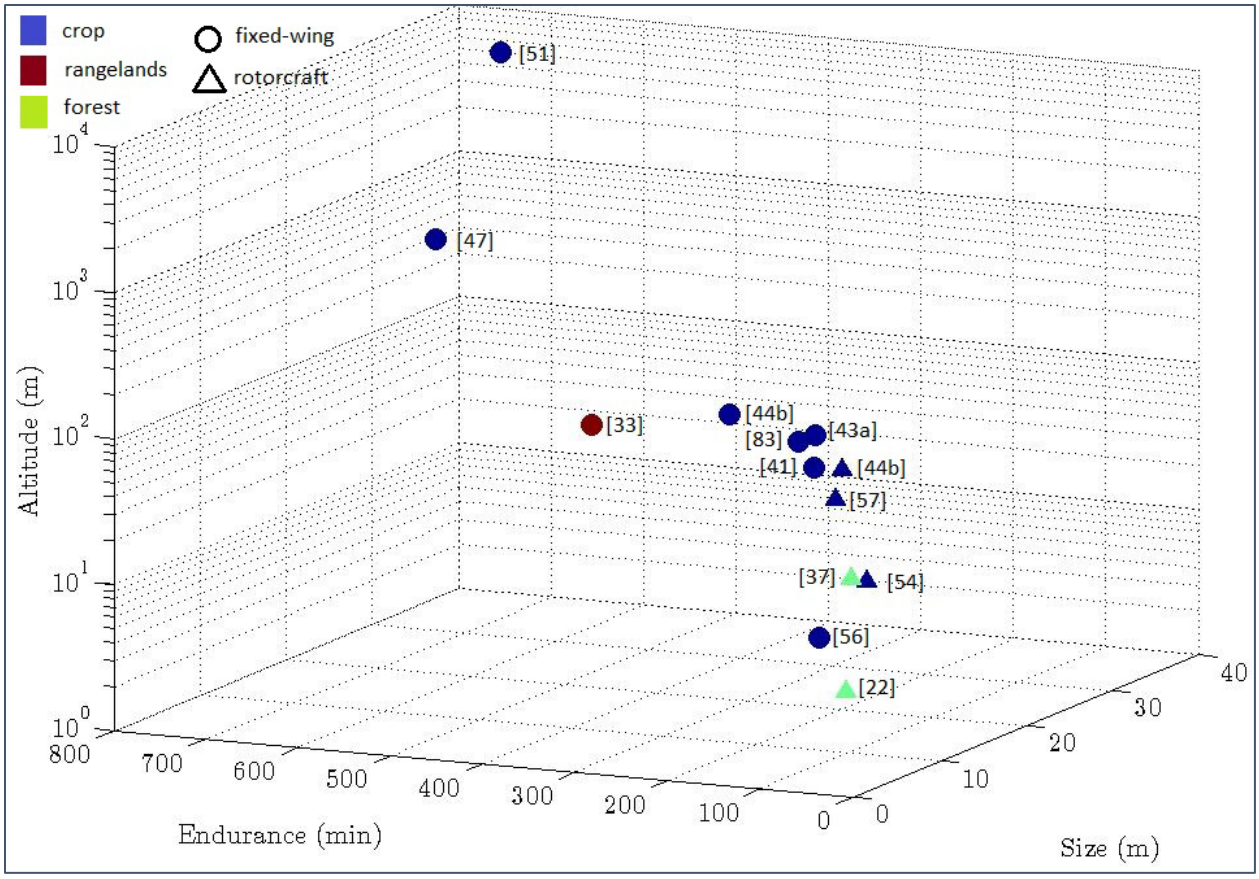

Figure 2.2 sUAS Experiments Classification (Reproduced from (Salami et al., 2014))

Figure 2.2 illustrates the wide range of tasks that sUAS can perform. The two classes of sUAS, fixed-wing, and rotorcraft (here on referred to as multirotor) differ in their flight duration, speed, and altitude. Multirotor sUAS has are typically used for short, low altitudes missions that require high-resolution imagery, but can also be flown at high altitudes to capture imagery data for larger areas. The flexibility in flight speed and altitude, take off requirements, and overall usability have catalyzed its use for hundreds of applications. Multirotor sUAS allow for vertical takeoff and landings and very low ground speeds (2 m/s).

Fixed wing sUAS, in contrast, operate similarly to manned aircraft and are capable of longer and higher altitude flights than multirotor sUAS. Longer flight times and higher altitude capabilities make fixed wing sUAS ideal for surveying and capturing data for large areas.

Federal Aviation Administration (FAA) regulations in the United States allow for flights altitudes up to 122 m while maintaining a clear line of sight. Altitudes or distances exceeding these defined thresholds will require additional clearance from the FAA. These regulations have allowed civilian use and research projects to take place without additional permits and licenses. Weight

and balance of the sUAS determine the battery life and subsequently the flight duration. Each sUAS has different payload capabilities and weight requirements, based on the battery and vehicle power. Improper balance or overloading of the vehicle can lead to reduced flight duration or lead to crashes.

When determining a sUAS to select for a given project, one must understand the scope of the project and the requirements demanded of the sUAS. Such demands may consider the amount of area needing covered, flight time to cover the desired area, desired data to be captured, and altitude requirements. The attachments (i.e. cameras, thermal sensing equipment, and telemetry) can be selected based on the project data requirements and sUAS specifications. Technology in sUAS design, payload capacity, and onboard sensor arrays are quickly closing the gap with satellite systems by allowing for the examination of higher spatial and temporal resolutions.

Ground

Early remote sensing began with satellite and ground systems as the primary source for data collection. Ground-based sensor systems can range from handheld devices to permanently fixed systems (Rodriguez-Moreno et al., 2017; Vina et al., 2004) such as those that are mounted on irrigation systems (Barnes et al., 2000). Advantages of ground systems include the close proximity to the target, low cost, ease of use, and flexibility of the platform. Close proximity to the target can eliminate atmospheric interference seen with satellite systems. Ground systems are beneficial because of the low noise and little correction Ground systems provide accurate imagery in controlled environments such as greenhouses because of their flexibility, size, and simple set up. Ground systems are also often used for preliminary surveys at a study area to determine if a larger study will produce viable results. Ground systems can be used to recover high-quality baseline data to calibrate or confirm the accuracy of aerial and satellite systems (Chavez, 1996; Collings & Caccetta, 2011; Moran et al., 1992; S. Sankaran et al., 2015; Swain et al., 2007; H. Zhang et al., 2013). For example, a field spectrometer can be used to measure several targets to collect baseline reflectance values, which can then be used to calibrate data collected from aerial systems (Smith & Milton, 1999).

Vegetative Indices

Vegetative indices are an important part of multispectral analysis applied to the terrestrial environment. Vegetation indices generate ratios that allow one to isolate and characterize specific

wavelengths related to plant health. Modification of indices using different wavelengths occurs readily based on study requirements. An example of this is seen with NDVI. The original NDVI equation takes into consideration only red and NIR wavelengths (Equation 2.1) (Rouse et al., 1974). NDVI was originally developed for use on satellite systems. Healthy plants reflect most of the NIR photons. Creating a ratio of NIR reflectance and a band in the visible spectrum gives a more complete interpretation of plant health. Blue and green bands are subject to large effects due to Rayleigh scattering. Rayleigh scattering affects the red band; however, the effects are minimal compared to the blue band. By normalizing the NIR and red bands NDVI was developed.

$$NDVI = \frac{R_{NIR} - R_{Red}}{R_{NIR} + R_{Red}} \qquad \text{Equation 2.1}$$

Where:

R_{NIR} = Reflectance in NIR (700 to 1200 nm)

R_{Red} = Reflectance in Red (600 to 700 nm)

Since its development, slight modifications to NDVI have transformed the NDVI to become more applicable. Modifications include green NDVI (GNDVI) and blue NDVI (BNDVI) as well as the normalized difference red-edge (NDRE), all of which can be used to detect slightly different vegetation characteristics (Barnes et al., 2000; A. A. Gitelson et al., 1996; A. A. Gitelson & Merzlyak, 1998). The vegetative index should be based on the remote sensing platform and sensor used for data collection as well as the desired outcome of the data. For example, BNDVI is suitable assessment with data captured from sUAS and manned aircraft because of the sensor's proximity to the earth. BNDVI may not be suitable for assessment of satellite-collected data because of the effect of Rayleigh scattering on the blue band. Vegetative indices continue to develop and evolve as the knowledge of plant characteristics and responses are expanded. A complete list of indices, formulas, and spectra covered is found in Appendix A.

Applications

Multispectral imagery has thousands of applications in many industries including agriculture, academics, construction, forestry, mining, and military, to name a few. Listed below are a few examples of applied multispectral imagery for vegetative surfaces in the agriculture, forestry, and land use industries.

Precision agriculture

Precision agriculture (PA) has amplified in the last decade as an obligation to feed a growing population continues to increase. sUAS have become the main platform to complete aerial PA work. sUAS allow for a precise real-time look at a given area and the effects of environmental conditions on crops and livestock.

Disease sensing

Plant diseases can result in large amounts of product losses, in times totaling billions of dollars nationwide. This can cause hardship for producers and consumers. Immediate detection of diseases is critical to maximizing yields and minimizing loss. Several researchers have used multispectral imagery to assess disease severity and symptoms. Disease detection can occur through the use of visible and IR spectroscopy (S. Sankaran et al., 2010) and multispectral imagery (Garcia-Ruiz et al., 2013; Yang et al., 2010). The amount of information derived from the visible and infrared areas of the electromagnetic spectrum makes visible and IR bands ideal for disease detection. IR regions provide information about the physiological stress levels within the plant with specific bands serving as indicators for certain diseases. All vegetation is affected by disease differently. Each plant reflects specific wavelengths that are used to detect and assess the type and severity of the disease present (S. Sankaran et al., 2010). Huanglongbing infested citrus trees can be assessed using GNDVI and soil-adjusted vegetation index (SAVI) with a narrow band multispectral camera (Garcia-Ruiz et al., 2013). Cotton root rot classification is best identified using only the NIR band (Yang et al., 2010). Sudden death syndrome (SDS) in soybean expresses strong correlations to pigment index (PI) proving that multispectral imagery is a useful tool for disease assessment (Hatton et al, presently unpublished work).

Water stress

Drought affects many parts of the world. Without adequate water, plants do not reach their yield potential and in extreme cases, die prematurely. Thermal imagery has proven useful for the assessment of crop water stress. Elevated canopy temperature in water-stressed plants often indicates less water content within the plant cells themselves (Idso et al., 1981). Vegetative indices to assess water stress in crops also display promising results without the requirement for thermal cameras. NDVI, canopy chlorophyll content index (CCCI), and crop water stress index (CWSI)

assess water stress and nitrogen stress on cotton. Water stress, nitrogen stress, and canopy density are distinguishable from one another and detectable through the indices (Barnes et al., 2000).

Nitrogen concentration

Nitrogen is one of the three macronutrients necessary for plant health and production. Nitrogen deficiencies lead to yield and growth reductions, but too much nitrogen can also have detrimental effects on plant health as well as pollution of the surrounding environment. Nitrogen assessments have been completed on many staple crops such as rice (Swain et al., 2007), cotton (Barnes et al., 2000) and wheat (Tilling et al., 2007). Nitrogen stress can often be detected by assessing the amount of chlorophyll content found within the plant's leaves (Barnes et al., 2000). Multispectral imagery and vegetation indices help to determine optimum nitrogen content in rice (Swain et al., 2007) and the effect of nitrogen treatments on wheat yield (Tilling et al., 2007).

Chlorophyll concentration

Chlorophyll concentrations are critical to the health and vitality of plants and without the proper chlorophyll concentration; plants are unable to photosynthesize correctly. Multispectral imagery has been proven useful for the detection of chlorophyll concentrations. Chlorophyll can be measured directly using CCCI as demonstrated by Swain et al. (2007) and Tilling et al. (2007) but also through the use of the triangular greenness index (TGI) (Hunt Jr. et al., 2013).

Best management practices

Multispectral remote sensing occurs year around allowing for data collection during any season or plant development stage. The flexibility and use throughout the growing season allow farmers to monitor crops to determine best management practices. Changes in crop biomass or health can lead to better irrigation scheduling or applications of fertilizer, herbicide, or pesticide. Link et al. (2013) utilized multispectral data to assess the application of fertilizer in order to implement changes as determined by the multispectral data. The non-invasive nature of remote sensing makes it a desirable choice for assessment of management practice as the aerial platform results in no soil compaction or disrupted plants (Link et al., 2013).

Land use

Assessment of land use is critical to the development of conservation (Singh et al., 2018); assessment of vegetation growth (Flynn & Chapra, 2014) and tracking of changes within the

environment (Getzin et al., 2014) and mapping land cover through land classification (Feng et al., 2015). Each of these is described below.

Land classification and vegetation mapping

Mapping of vegetation types generates an understanding of land cover. Reflectance values obtained from multispectral imagery can be used to classify certain pixel values into land use categories. Classification of land cover through a random forest model is just one of many ways to map vegetation and classify land cover. However, the inclusion of texture patterns within the imagery leads to much more accurate results (Feng et al., 2015). Multispectral remote sensing can be useful in the classification of land cover based on the reflectance of the surface through the electromagnetic spectrum.

Forested mapping and conservation

Forest mapping is extremely important in the conservation of natural habitats, especially in the wake of increasing deforestation. Mapping forest and fragmentation patterns can help assess the rate and pattern of deforestation. Forest health can be monitored by using remote sensing to help understand factors affecting the health such as disease or pests. Multispectral imagery also allows for the mapping and monitoring of gap patterns for assessment of forest floor cover (Getzin et al., 2014). Application of this forest mapping across the world will track the cover in the forests and assess the changes in the canopy.

Conservation of wildlife is becoming more important as the loss of habitat continues to endanger the existence of species every day. Forest mapping using LiDAR, Landsat imagery, and GPS locational data, over Indonesia has led to an understanding of habitat, environmental factors, and disturbances affecting habit for two primate species. It was discovered that feeding, sleeping and ranging habits for both species were influenced by on disturbances to their environment. In fact, one primate species strictly avoided burned areas by changing sleeping and ranging habitat completely. (Singh et al., 2018). Studies like this can help in understanding and influence conservation management practices all over the world.

Vegetation growth assessment

Vegetation growth is critical to understanding the overall health of an environment and how factors influence changes in that environment. Aquatic vegetation helps maintain river clarity, water purity, and a balanced ecosystem, while also providing vital habitat for aquatic species.

Monitoring stream algae helps to assess the health of the river and its ecosystem. Flynn & Chapra (2014) developed a system designed to assess the aquatic vegetation over a shallow non-turbid river using a sUAS. Using sUAS imagery, they mapped the spread of algae along the river from April to December leading to an understanding of the algae's growth cycle within the river system (Flynn & Chapra, 2014).

Arctic moss beds support many small mammals. The understanding of the moss's growth after the first winter freeze is critical to understanding of their role in the ecosystem. Multispectral imagery allowed for thematic mapping of arctic moss beds for gathering spatial and environmental data on arctic moss beds with a modified Triangular Vegetation Index (MTVI2). The surface temperature of the moss and MTVI2 demonstrate strong accuracy for co-registration methodology (Turner et al., 2014).

Conclusion

Multispectral remote sensing has the capability to provide on-demand assessment for small areas ranging from a few hectares to large areas the size of the Amazon River basin to the entire world. Multispectral imagery is well suited for a variety of operations and flexible enough to fit any other operation from field assessments to automated analysis. The requirement for rapid assessment of cropland and other vegetated areas will always be high because of the requirement to maximize yield and land cover.

Measurement and detection of reflectance of radiation or light from a plant allow for assessment of plant qualities. Healthy and unhealthy plants reflect radiation differently based on the pigments present within the plant structure, stress due to water, or nutrient deficiencies, and changes in environmental conditions. Farmers and researchers can determine the plant health based on light reflectance of the plant through the electromagnetic spectrum with the help of multispectral sensors.

Multispectral sensors come in all shapes and sizes but have four resolutions that greatly affect the type of sensor used for data collection. Temporal, spatial, spectral, and radiometric resolution are important to consider when designing a project and selecting a sensor. While all four cannot be maximized they can be optimized based on the needs of the project.

Data collection alone will not yield accurate results. Calibration and correction of multispectral imagery are critical for accurate analysis of results. There are a number of methods suitable for image calibration and correction but the requirements, of the system and physical location of the

study need to be considered before calibration or correction can take place. Without a correct understanding of the system and location, calibrations and corrections can be incorrectly applied causing data to be inaccurate.

Satellite, aerial, and ground remote sensing systems all allow for assessment and are beneficial given different parameters. The biggest consideration when choosing a platform is the requirements of the project. Each platform has the capability of producing the same results for vegetation sensing however, the scales will be different for each.

Multispectral remote sensing of vegetative areas contributes understanding of how the earth is used, how vegetation interacts with ecosystems, how crops utilize nutrients, water, fight disease, and how to manage crops to produce the maximum yield. Vegetative indices are beneficial to a number of industries and help the growth of precision agriculture. Creating a ratio of different bands allows for isolation of a specific factor affecting plant health, such as disease, water stress, or nutrient deficiencies. Multispectral remote sensing can be applied in almost any aspect of vegetation studies. It has been used for the assessment of forest fragmentation to land cover to water stress analysis in crop. Remote sensing continues to grow and develop as more people utilize the possibilities of the practice. As this field grows, the possibilities are endless.

Chapter 3 - Comparison of aerial and ground remote sensing to quantify sudden death syndrome in soybeans

Nicholle M. Hatton[1], Ethan Menke[2], Ajay Sharda[1], Deon van der Merwe[3], and William Schapaugh Jr[2]

[1]Department of Biological and Agricultural Engineering, College of Engineering; [2]Department of Agronomy, College of Agriculture, Kansas State University; [3]Department of Farm Animal Health, Faculty of Veterinary Medicine, University of Utrecht

Abstract

Discovered in 1971, Sudden Death Syndrome (SDS), caused by the fungus Fusarium virguliforme, has spread from the US to South American and European countries with the potential to infect plants worldwide. Yield loss of 10% to 15% and 70% in extreme cases are common for infected plants. Currently, SDS impacts are scored by visual assessment of infection severity and percent of crop diseased. The manual process requires 3-4 hours to collect row based coarse data for a 3-5 acre field. The quality of data collected over several hours is impacted due to changing diurnal environmental conditions. Small unmanned aerial systems (sUAS) offer an alternative method of data collection while eliminating changing environmental conditions due to the short flight times. A platform designed to collect high throughput aerial imagery data to quantify SDS is proposed. Similar systems have been used for disease detection in crops, however; this system has not been evaluated to ascertain if it can provide a similar or improved assessment of SDS. A comparative evaluation of ground-based and aerial remote sensing methods for scoring of SDS is proposed to evaluate efficacy. The purpose of this research was to (1) determine if PI can be used for the assessment and quantification of SDS and assess the validity of each component of SDS score, (2) compare validity and accuracy of ground-based and aerial remote sensing methods for scoring of SDS to determine benefits of aerial remote sensing of SDS, and (3) assess the use of PI for determination of maturity. A seven-acre field was selected as test plots to collect both manual reflectance using a spectrometer and aerial imagery using color infrared camera over a two year period. Aerial imagery was collected using a sUAS late in the growing season and at maturity each year. Image processing was conducted to produce pigment index (PI) maps from the orthomosaics.

PI values were compared to manual collected ground-based data. Results showed a negative correlation between SDS scores and pigment index values. The aerial imagery and ground-based data showed strong correlation indicating that aerial data could be applied to spatial maps to score SDS. Aerial and ground-based data were assessed for high instances of SDS with aerial data showing less variability (R^2=0.8359). The second-year analyzed each component of SDS score, severity, and incidence, with two flights. PI proved to be the best indicator of severity compared with SDS score and incidence with R^2=0.6313 and ρ=-0.8016 for the first day of flight. PI also accurately correlated to SDS score with R^2=0.6159 and ρ=-0.7916. The second flight showed a weaker correlation between PI and SDS score and severity. The decreasing trend can be accounted for due to the timing of the growth stage. Overall, PI proves to be a good indicator of SDS score and severity.

Introduction

Sudden Death Syndrome (SDS) in soybean is a fungal infection of the roots that was first discovered in the United States in 1971 (Roy et al., 1997; Xing & Westphal, 2009). The disease has since spread from the soybean producing states, posing a significant threat to the Midwest and the majority of U.S. soybean production, to South America and Europe. Extreme cases of SDS can cause premature death of the plant (Chong et al., 2005; Roy et al., 1997) and it is reported to have a 100% mortality rate extreme cases (Hartman et al., 1999). Typical SDS impacted soybean will result in a 20% to 50% loss (Roy et al., 1997). U.S. financial impacts due to SDS in 2005 were estimated at $118.9 million or 504,101 tons (Wrather & Koenning, 2006). This impact has since grown to an estimated $1.6 billion in losses from the 2016 growing season (Manage soybean risks, SDS and SCN with ILeVO.2016).

SDS is caused by *Fusarium virguliforme* (or *F. solani*) which target the plant's rooting system, causing the roots to turn brown or grey in color. Foliar symptoms develop after the disease has reached later stages. Root infection occurs early in plant development, while foliar symptoms appear after flowering (Chong et al., 2005; Cui et al., 2014; Roy et al., 1997; Shrivastava et al., 2015; Tang et al., 2010; Xing & Westphal, 2009). The root systems of infected plants will begin to show discoloration and node formation in advanced cases (Chong et al., 2005). The vascular root tissue begins to break down and turn gray in color with infection. Grey tissue limits the nutrients through the plant. Nodes begin to develop through the root system. After the root system has developed symptoms, foliar symptoms begin as the plant is in the flowering stage of its growth

cycle. Foliar symptoms will begin with light yellow interveinal chlorotic spots (Chong et al., 2005; Cui et al., 2014) progressing to chlorosis and eventually becoming necrotic as the infection progresses, Figure 3.1 (Hartman et al., 1999). The only remaining green on the plant will be found on both mid-veins and major lateral veins in the late stages of infection, Figure 3.1 (Hartman et al., 1999; Tang et al., 2010). Infection during the flowering stage of the life cycle results in dropping of the blooms and pods beginning with the uppermost pods (Roy et al., 1997). There are some documented cases where both the leaves and the roots did not show outward symptoms, thus the presence of SDS is confirmed by internal gray coloring in the cutting of the root (Roy et al., 1997).

Figure 3.1 - SDS foliar symptoms a) chlorotic spotting and interveinal chlorosis in the beginning stages b) defoliation

SDS is known to occur in areas of heavy moisture and reported to be most destructive when soybeans are planted in cool, wet soils (Westphal et al., 2006). Heavy midsummer rains that saturate the soil are known to contribute to fungus growth and soil temperatures between 55^0F to 65^0F create an ideal environment for *F. virguliforme* to propagate (Shrivastava et al., 2015; Westphal et al., 2006). An entire field may develop symptoms of SDS, but commonly, varying field conditions produce areas of concentrated impacts (e.g. hotspots) of SDS (Roy et al., 1997).

In terms of soybean production, agronomist, producers, and service providers typically manually scout the field to determine crop damage from SDS. The goal of field scouting to develop crop management and mitigation, i.e. irrigation water strategies to minimize the crop damage and

minimize further development of symptoms. Plant breeders developing new soybean SDS resistant cultivars collect whole field SDS scores to compare and contrast different genotypes for selection (Anderson et al., 2015; Ngaki et al., 2016). Field researchers conducting cultivar research have to walk the field to collect information to quantify the extent of SDS. More recently, researchers have manually collected crop reflectance utilizing spectrometers, and then utilize reflectance information to calculate crop vegetative indices along with ground-based truth data to quantify incidence and extent of SDS (Bajwa et al., 2017). However, all these techniques required numerous hours of operation as it requires the researcher to walk along all crop rows to collect data. The time required for a small field is high with data collection usually beginning around mid-morning and ending several hours later. The extended period of operation is of concern as the solar radiation intensity or irradiance, weather, and temperature varies over the day having a potential impact on the reflectance observations from plant canopy with similar health. Therefore, an improved method would rapidly assess the large areas and accurately quantify SDS on a spatial scale adequate for both researchers and producers.

Small unmanned aerial systems (sUAS) has had success in a variety of research efforts, ranging from the determination of soil erosion (d'Oleire-Oltmanns et al., 2011), leaf cover (McGwire et al., 2013), and Normalized Difference Vegetation Index estimations (NDVI) (Salami et al., 2014) to aerial monitoring of spatial arrangements between shrubs and disturbance gradients (Bybordi & Reggiani, 2015; Mitchell et al., 2012; J. Primicerio et al., 2012a; Themistocleous et al., 2014). sUAS typically are comprised of aerial vehicle and ground-based control systems to develop, program and manage flight missions. During field research, investigators have commonly used multi-rotor and fixed sUAS platform and have found them to be beneficial for surveying smaller areas that require a high resolution (C. Zhang & Kovacs, 2012). Fixed wing sUAS operate like an airplane where take-off and landing require a landing strip, operate at relatively high speed before flight is achieved and during flight, and cover large areas (e.g. 100's to 1000's of acres) quickly and in a single flight. Fixed wing sUAS are also presently capable of carrying larger payloads and can easily reach altitudes above the limit set by the Federal Aviation Administration (FAA). Multirotor sUAS platforms are relatively easy to use; can perform vertical take-off and landings; have hover capabilities; provide good camera control, and can travel at slower speeds and lower altitudes. The flight time and payload depends on the selection of a multirotor but these platforms can easily cover relatively small acres quickly. Therefore, researchers are finding greater utility of

sensors mounted on multirotor sUAS platforms to quickly collect spatial higher-resolution imagery and draw conclusions on crop and soil variability (Bendig et al., 2014; Calderón et al., 2014a; Gómez-Candón et al., 2014; J. Primicerio et al., 2012b; Salami et al., 2014; C. Zhang & Kovacs, 2012).

sUAS aerial imagery has been utilized for years in precision agriculture, but few studies have been conducted to verify accuracy. Several studies have combined multispectral imagery with ground-based observations to generate more accurate maps of a given area for analysis (Bendig et al., 2014; Campomanes et al., 2015; Collings & Caccetta, 2011; Huang et al., 2010a; Kaleita, 2006). Gitelson et al. (1998) utilized remote sensing to validate NDVI and green normalized difference vegetation index (GNDVI) measurements within various tree species against ground-based imagery (A. A. Gitelson & Merzlyak, 1998). More recently, remote sensing methods have been utilized as an indicator of downy mildew infection of opium poppy. This study found that aerial generated imagery was equally accurate to ground-based generated data (Calderón et al., 2014b). Wheat phenotyping validation comparing multispectral aerial imagery to that or ground-based reflectance data exhibited that multispectral imagery can be utilized to generate accurate "high-throughput phenomics in wheat breeding" (S. Sankaran et al., 2015). Zhang et al. (2013) demonstrated that aerial remote sensing had a 90% accuracy in detection of cotton plants when compared with ground-based hyperspectral accuracy of 93.3% (H. Zhang et al., 2013). Most recently, Lukas et al. (2016) were able to demonstrate that sUAS provide reliable information for site-specific management (Lukas et al., 2016).

Color infrared (CIR) is the common sensor use on sUAS platforms to detect canopy reflectance response. CIR reflectance data gathered by a sUAS mounted camera provide very useful information on photosynthesis and canopy energy balance. The reflectance information can be used to derive a variety of vegetative indices, including NDVI and Pigment Index (PI). The vegetative indices indicate the health of a given area by measuring the amount of specific light reflected by the plant (Pinter et al., 2003). Low NDVI values have been exposed as an indicator of plant stress due to water, disease, nutrient deficiencies etc. (F. Liu et al., 2012; Suárez et al., 2008; Vina et al., 2004). Overall, the capability to view the whole field at once and conduct spatial analysis substantially expands research capabilities on topics such as plant health.

sUAS platforms have been revealed to provide accurate data when directly compared to ground-based data, little data have been collected on SDS using aerial remote sensing methods.

To date, no studies have compared the validity of utilizing sUAS for accurate detection SDS. The utilization of sUAS to accurately assess SDS impacted fields would significantly reduce the time and cost of an evaluation compared with ground-based detection methods. Further, it could be utilized as a high throughput phenotyping method allowing for accurate and rapid assessment of diseased fields. The purpose of this research was to (1) determine if PI can be used for the assessment and quantification of SDS, (2) compare validity and accuracy of ground-based and aerial remote sensing methods for scoring of SDS to determine benefits of aerial remote sensing of SDS, and (3) assess the use of PI for determination of maturity.

Methods

A methodical approach was developed for completing a comparative evaluation of data collected using aerial methods paired with terrestrial. The process included completing the following:

- Establishing plot information the plot location and planting methods such as planting date, varieties planted, and infection
- Following the set criteria for SDS scoring and conducting SDS scoring
- Establishing the ground unit and implementing ground-based data collection
- Establishing the aerial platform, identifying the sUAS and sensors used for each flight, and mission planning rationale
- Monitoring flight conditions including the weather conditions relating to the days that aerial data were collected
- Completing data processing comparing aerial images and ground-based data.

This study was conducted in 2016 and 2017. The first year ground-based truth was utilized to establish the feasibility of utilization of aerial systems for SDS scoring. The second-year establishes a methodology for aerial SDS scoring and accuracy comparison over the entire plot. Presented below is a detailed summary of the approach applied.

Study site

Soybean genotype plots were established in 2016 and 2017 crop seasons at the Kansas State University, Kansas River Valley Experiment Field outside of Rossville, Kansas (39.11852°, -95.92459°). The dominant soil type was a Eudora silt loam. The study area was selected because of a history of SDS impacted crops. No artificial inoculation of the crops with fungus was required. To ensure disease severity, an overhead pivot applied water throughout the growing season.

All plots had maturity and SDS ratings collected. Maturity was recorded as the date after 31 August when 95% of the pods on the plants had reached mature color. SDS ratings were taken at the R6 growth stage of the plants (Fehr et al., 1971).

Genotypes planted included a Nested Association Mapping population (NAM 10) consisting of 140 F_5 derived lines from a cross between IA 3023 by LD00-3309 along with checks for yield, SDS, and agronomic traits, for a total of 160 entries. SDS resistant checks from maturity groups, three and four were LD06-7862, Ripley, and LS09-1920. SDS susceptible checks from maturity groups three and four were Morgan and Spencer. Four replications occurred for entries in the NAM population. The NAM population used a randomized complete block design consisting of two row plots 3.8 m long with 0.76 m row spacing, Plots were planted on 12 May 2016 and 9 May 2017 into no-till corn stubble and pre-emergence herbicides were applied to prevent early season weed growth. Postemergence applications of herbicide and manual removal were used to control weeds throughout the season. Irrigation was applied throughout the growing season to maintain adequate soil moisture and to help increase the severity of SDS. NAM 10 plots were harvested on 29 September 2016 and 4 October 2016.

Ground-based Plant Health

Ground-based measurements were collected from near canopy closure to R7 growth stage and the start of maturity (Fehr & Cavinness, 1977). Data was collected on cloud-free days between 10 a.m. and 2 p.m. to limit solar effects. Two Ocean Optics USB2000 hyperspectral spectrometers (Ocean Optics, Largo, Florida, USA) were mounted on a monopod to collect reflectance measurements from 350-1027 nm. Spectrometer held vertically approximately one-half meter over the middle of the two-row plots. Calibration of the spectrometer occurred with a standard reflectance panel. A tablet operating CALMIT Data Acquisition Program 2 (CDAP-2, UNL Nutech Ventures, Lincoln, Nebraska) was used to control and integrate the spectral measurement from the spectrometers. Ten scans of the plot were taken and the software system averaged to give a mean reflectance for the entire plot. Post-processing of the collected data were performed through CDAP-2 to generate reflectance values for each plot. The ground-based measurements on check plots were collected only for 2016 season to compare and contrast against the aerial imagery results.

Sudden Death Syndrome Scoring

SDS foliar symptoms were rated at R6 for all varieties. R6 refers to a growth stage with pod cavity filled, seeds just reaching full size. R6 has been designated for SDS scoring because symptom expression tends to be the best developed at this stage. Plots were scored for disease severity (Ds) on the scale of 1-9 based on foliar symptoms and disease incidence (Di) from 0-100% in 5% increments based on the amount of the plot that expresses foliar symptoms (Schmidt, 2007). Severity score criteria are shown in Table 3.1. Scoring was performed on 31 August 2016 and 6 September 2017 by the same individual to reduce as much variability as possible. Disease index (Dx) was established by Equation 1 (Nijti et al., 2001) and will range from zero to 100. SDS is considered to be severe if the disease index score is above 25.

Table 3.1 - SDS Severity Scoring Guidelines

Score	Description of Symptoms
1	1-10% of leaf surface chlorotic, OR 1-5% necrotic
2	10-20% of leaf surface chlorotic, OR 6-10% necrotic
3	20-40% of leaf surface chlorotic, OR 11-20% necrotic
4	40-60% of leaf surface chlorotic, OR 21-40% necrotic
5	Greater than 60% of leaf surface chlorotic, OR greater than 40% necrotic
6	Premature leaf drop up to 1/3 defoliation
7	Premature leaf drop up to 2/3 defoliation
8	Premature leaf drop GREATER than 2/3 defoliation
9	Premature death

$$D_x = \frac{D_i * D_s}{9} \qquad \text{Equation 3.1}$$

Where:

Dx = SDS score

Di = Disease Incidence

Ds = Disease Severity

Aerial Imagery

An IRIS$^+$ multirotor (3D Robotics, Berkley, California, USA) and Ritewing Zephyr 3 (Rightwing Rc LLC, Apache Junction, Arizona, USA) fixed wing with a 47-inch wingspan sUAS were used as aerial platforms to mount spectral sensors and collect aerial imagery. The fixed wing

has a designed endurance of 30 minutes flight with a payload of up to 400 g; whereas multirotor are designed for approximately five minutes with the similar payload. A CIR (modified Sony Alpha 5100 (Sony Corporation, Tokyo, Japan) converted for Blue/Green/NIR bands(Arrow Consulting LLC, Manhattan, Kansas, USA)) sensor was utilized with the fixed-wing platform in 2016 and on multirotor in 2017 to collect aerial imagery. Both the IRIS^{+} and Ritewing Zephyr were utilized while collecting data for this study.

Camera/Planes

Two cameras were utilized to capture data depending on the type required. A modified Sony Alpha 5100 (Sony Corporation, Tokyo, Japan) converted to Blue/Green/NIR was utilized with the Ritewing Zephyr 3 (2016 data collection) and a 3DR IRIS+ (2017 data collection). DJI Phantom 4 Pro (DJI, Shenzhen, China), a rotary sUAS, utilizes an onboard 12.4-megapixel camera. Single images were utilized for this study. Visible images taken with the DJI Phantom 4 Pro were used for reference and visualization of the study area.

Mission Planning

Mission planning was accomplished through Mission Planner (ArduPilot) and Pix4D Capture (Pix4D, Lausanne, Switzerland) apps that allow easier control and observation of sUAS flight details. sUAS aerial imagery was collection both for 2016 and 2017 season. As mentioned earlier, 2016 data was used to compare and contrast between aerial imagery and ground-based data to quantify SDS on check plots and 2017 data was used to ascertain SDS on the whole field scale. The sUAS flights were conducted on 18 August 2016, 8 September 2017, and 13 September 2017, henceforth referred as flying dates or FD1, FD2, and FD3 respectively. Flights in 2017 occurred two and seven days after SDS scoring and 14 days before scoring in 2016. The entire field was scored with PI values taken. For FD1, true color images were collected with the DJI Phantom 4 Pro and color infrared (CIR) images were collected using fixed-wing sUAS. The fixed wing sUAS was programmed to fly at an altitude of 120 m above ground level (AGL) with a front-to-back and side-to-side overlap of 75% following a single grid pattern. The sUAS for true color image capture was flown at 40m AGL with an 85% front to back and side-to-side overlap. For FD2, CIR images were collected using quadcopter programmed to fly at 80 m with front-to-back and side-to-side overlap of 75%. The true color camera on a quadcopter was programmed to fly at 60 m with front-to-back and side-to-side overlap of 80%. For FD3, true color and CIR images were collected using

parameters programmed on FD2. The sUAS multirotor with CIR and fixed wing with CIR sensor were programmed to fly at 5 m/s and 18 m/s respectively. Ground control points were set for each FD with GPS locations recorded. Ground control points were used for the correction and optimization of the orthomosaic. Altitudes were selected to optimize spatial resolution, battery life and sUAS flight capabilities. The side-to-side and front-to-back overlap were selected based on parameters of generation of an accurate orthomosaic. The crop and weather parameters are shown in Table 3.2. The weather parameters were atmospherically stable and suitable for flying on each of the three FDs.

Table 3.2 - Weather Conditions

Date	18-Aug (FD1)	8-Sept (FD2)	13-Sept (FD3)
Temperature (^{0}C)	31.5	26.7	21.1
Relative Humidity (%)	58	47	72
Wind Speed (mph)	5-12	10	5
Conditions	Clear	Clear	Clear
Crop growth status	Closed canopy	Near maturity	At maturity

Data Processing

Pigment Index

Photosynthesis uses chlorophyll a and b to absorb photon energy for conversion to sugar and fatty acids. A secondary product of the conversion process are reactive oxygen species that can be harmful to plants in high concentrations. Reactive oxygen species are produced in minute amounts in healthy plants because of aerobic metabolism. Stress causes the amount of reactive oxygen species to increase (Hodecker et al., 2018; Kang et al., 2017). Additionally, microorganisms like fungi and bacteria invade the plant tissue by producing a high concentration of reactive oxygen species, which overwhelm the plant's cells defenses to oxidative damage. Reduction of reactive oxygen species occurs through the production of carotenoids, an antioxidant (S. H. Kim et al., 2012). The more stressed the plant becomes the more carotenoids produced. Carotenoids absorb and reflect photons in a manner that can be used to assess changes in carotenoid concentrations and therefore has the potential to be used to assess plant stress. Understanding how different pigments (i.e. chlorophyll a and b and carotenoids) absorb and reflect photons within plant material

can lead to the development of methods to detect changes in chlorophyll: carotenoid ratios, and potentially assessment of plant stress.

Chlorophyll a and b absorb photons in blue and red regions while carotenoids absorb photons across blue and green regions of the visible light spectrum (Chappelle et al., 1992), represented in Figure 3.2 (Heliospectra, 2014). Plants also reflect photons very strongly in the NIR region. Measuring the absorption and reflectance of photons for the assessment of plant health is often done by generating a normalized difference vegetation index (NDVI). NDVI (Equation 3.2) has been used in the assessment of plant biomass and growth vigor (Granados-Ramírez et al., 2004; C. J. Tucker et al., 1985). NDVI however, is not a reliable indicator of plant stress because plant stress and biomass are confounded (D. van der Merwe, personal communication, 2016).

$$NDVI = \frac{R_{NIR} - R_{Red}}{R_{NIR} + R_{Red}} \qquad \text{Equation 3.2}$$

Where:

R_{NIR} = Reflectance in NIR (700 to 1200 nm)

R_{Red} = Reflectance in Red (600 to 700 nm)

Variations of the NDVI have been developed to assess different regions of the visible spectrum and their relationships to plant characteristics. Blue normalized difference vegetation index (BNDVI) and green normalized difference vegetation index (GNDVI) assess the photons reflected in the blue and green regions, respectively. The BNDVI, Equation 3.4, is primarily determined by chlorophyll concentration, with some influence from the carotenoid content. The GNDVI, Equation 3.3, is influenced more heavily by the carotenoid concentration and has been used successfully as an indicator of plant health (A. A. Gitelson et al., 1996). Individually, either type of NDVI does not accurately or completely assess plant stress because of the confounding influence of biomass on the NDVI value. A new index called Pigment Index (PI), which reduces the confounding influence of biomass, was derived by subtracting the GNDVI from the BNDVI (KSURF Invention Disclosure No. 2016-010, 2016). PI assesses reflectance from blue, green, and NIR regions captured with a modified broadband camera to assess plant stress (Equation 3.5). PI changes with the changing ratios of carotenoids to chlorophylls. Increased ratios of carotenoids to chlorophylls indicate stress conditions in the plant, or other physiological conditions that lead to changes in chlorophyll: carotenoid ratios, such as the normal progression through growth stages

(D. van der Merwe, personal communication, 2016). Low PI values can be a sign of high concentrations of carotenoids, resulting from plant stress.

It was hypothesized that the introduction of stress and reduction of photosynthetic potential in plants suffering from SDS will result in lowered PI-values. To test this hypothesis, an experimental field of soybean with varied levels of SDS was assessed to determine the degree of correlation between SDS and PI values. As symptoms of SDS progress, the plant is unable to photosynthesize at the same rate as healthy plants. The reduction of photosynthesis causes an increase in the blue light reflected. PI reduction due to stress and reduced photosynthetic activity are apparent in early and late stages of disease progression.

$$GNDVI = \frac{R_{NIR} - R_{Green}}{R_{NIR} + R_{Green}} \quad \text{Equation 3.3}$$

$$BNDVI = \frac{R_{NIR} - R_{Blue}}{R_{NIR} + R_{Blue}} \quad \text{Equation 3.4}$$

Where

R_{NIR} = Reflectance in NIR (700-1200nm)

R_{Blue} = Reflectance in blue (400-500 nm)

R_{Green} = Reflectance in green (500-600 nm)

$$PI = BNDVI - GNDVI \quad \text{Equation 3.5}$$

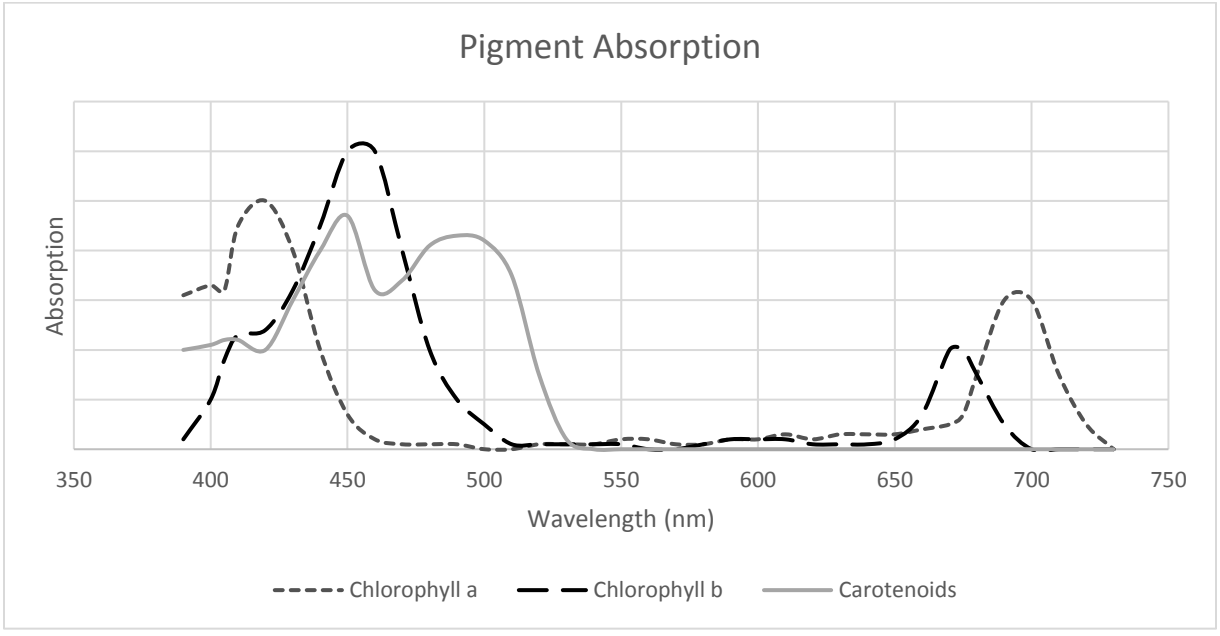

Figure 3.2 - Representation of plant pigments. Chlorophyll a and b and carotenoids included.

Larger fractions of available light are absorbed in low light areas such as shadow, resulting in higher BNDVI and GNDVI values that are not correlated with the physiological condition of plants. This artifact is particularly prominent in imagery captured from low altitude aircraft such as sUAS using sensors with wide-angle lenses. PI reduces the impact of this artifact (D. van der Merwe, personal communication, 2016). Figure 3.3 displays a comparison of PI to GNDVI and BNDVI over one portion of the study area. It can be seen that much of the dark green (0.9-1) area in the GNDVI image occurs in areas of shadow as determined from the CIR image (Figure 3.3a). The GNDVI (Figure 3.3c) inaccurately calculates high values in shadowed areas. BNDVI (Figure 3.3d) inaccurately assesses portions of the wheel tracks seen across row 9 of the field. The wheel track should not display "healthier" areas than the surrounding vegetation. The subtraction of the GNDVI from the BNDVI reduces shadow artifacts because the shadow effect is similar in both NDVI types (D. van der Merwe, personal communication, 2016). Figure 3.3b demonstrates the PI with reduced shadow artifacts in the wheel tracks.

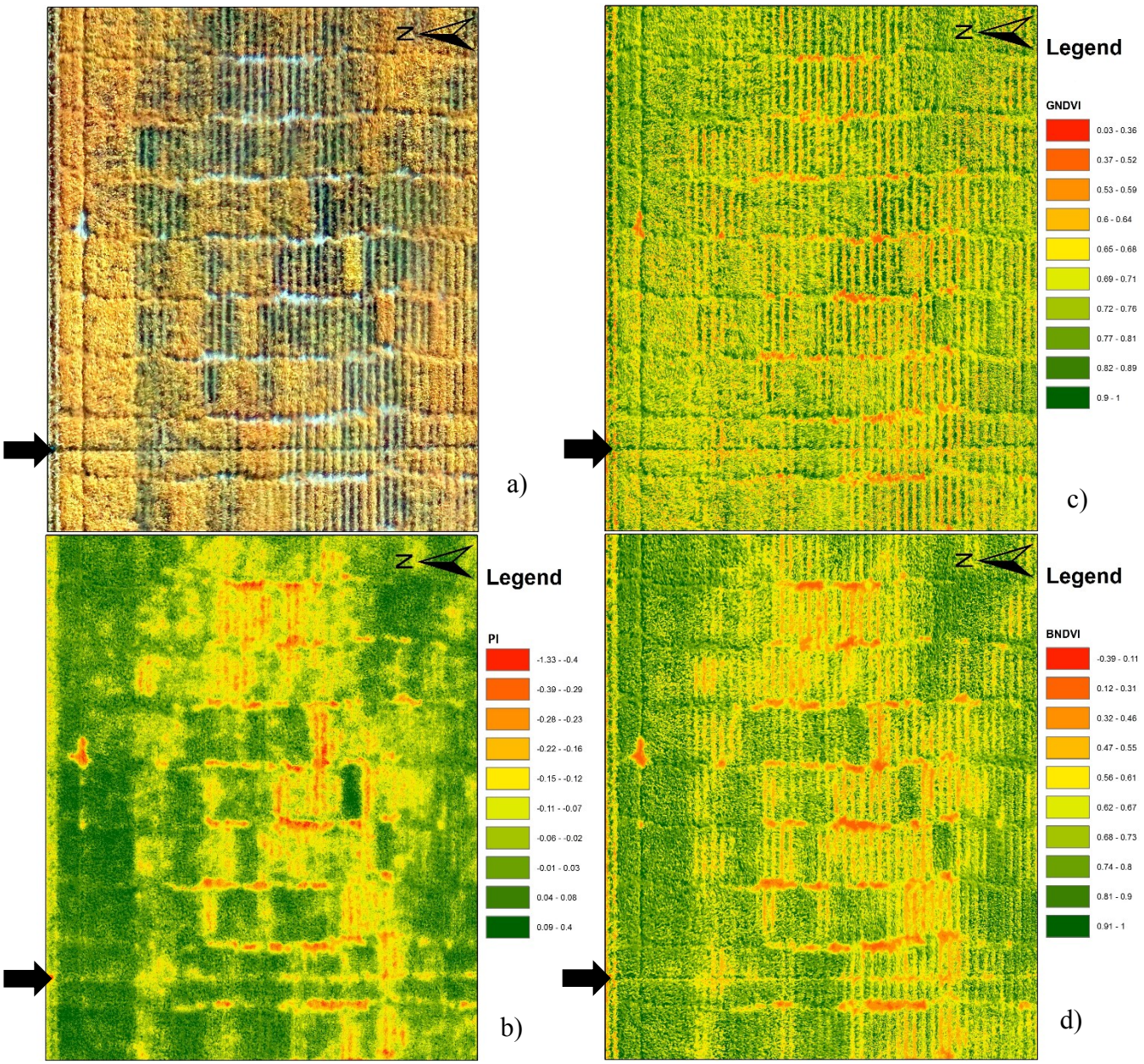

Figure 3.3 - PI comparison with GNDVI and BNDVI from 13 September 2017 data set. The image covers NAM 10 plots from row 8 to 16 a) displays original section of the field in CIR image b) displays the PI generated for the given section c) displays the generated GNDVI for the given section and d) displays the BNDVI generated for the given section. Legends for each map are given in reference to that specific map. Arrow indicates wheel track in each image.

Ground-based Data

Initial processing of the raw spectral data were completed using CDAP-2 software to provide an average reflectance value at each of the collected wavebands for each plot. The ultraviolet wavelength readings were removed from the data. The remaining data were averaged over ten-

nanometer bands to reduce the dimensionality of the data set (Phatak, 2004). Missing scans and bad scans were removed from the dataset, data were then combined with the collected agronomic data, such as SDS rating and yield. Proc Mixed in SAS 9.4 was used to determine if the individual day had significant interaction between the genotype and wavelength. The ground-based reading on 17 August 2016, closest to the sUAS data collection did not have significant interaction between entry and reflectance reading due to uncontrollable environmental effects. For this reason, the next closest collected day was used which was 8 August 2016 which did show a significant difference between entries and reflectance values. PROC CORR used to help select waveband from ground-based data to form indices. Blue reflectance was calculated as an average of 465 nm and 475 nm wavebands, green reflectance was calculated as an average of 565 nm and 575 nm wavebands, and NIR reflectance was calculated as an average of 775 nm and 785 nm. These averages were then used to calculate BNDVI, GNDVI, and PI as shown above.

Aerial Image Processing

Agisoft Photoscan Professional (V 1.2.6, Agisoft LLC, St. Petersburg, Russia) generated an orthomosaic using weighted average values of all pixel reflectance values from individual photos. Ground reference panels were used for geometric correction and accuracy of the orthomosaic. The orthomosaic was then processed in ArcGIS 10.3 (ArcMap 10.4.1, Esri, Redlands, California, USA) to calculate GNDVI, BNDVI, and PI. Spatial analysis calculated and converted the orthomosaic into GNDVI, BDNVI, and PI maps of the field. The maps were generated with a color gradient of green to red indicating high to low vegetative index values, Figure 3.4.

Transects established through the approximate center of each row allowed for the average GNDVI, BNDVI, and PI to be for calculation of the plot average, Figure 3.4. The transect data were extracted and averaged across the two rows in a plot to establish the two-row average for each plot allowing for comparison between aerial and ground-based spectral reflectance data and SDS scores. Both the aerial and ground-based data have one average value for the selected plot at the completion of this analysis.

Pix4Dmapper Pro (Pix4Dmapper Pro 2.2.25, Lausanne, Switzerland) was used to generate a surface elevation model and an orthomosaic map used for reference and accuracy checks during data analysis. Additionally, the instances of high SDS plots were looked at to determine the accuracy of PI when detecting severe SDS. Any plot scoring above a 25 is considered high. The

results could indicate the accuracy to quantify incidences of high SDS using the PI derived from ground-based system and sUAS aerial imagery.

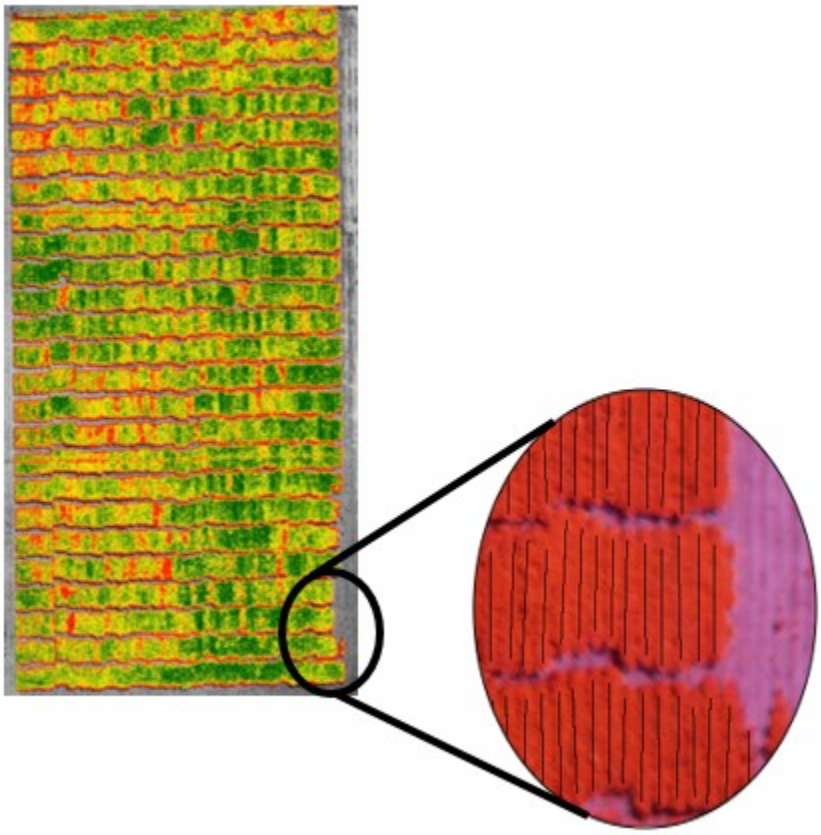

Figure 3.4 - Example pigment index (PI) map generated using aerial imagery collected on FD1 with of transects across each row (PI layer turned off for accessibility in transect). Green indicates high PI while red indicates low PI

Statistics

Nearest neighbor analysis was run to account for variations within the field resulting from environmental effects. Nearest neighbor analysis was run based on the three plots to the north and south and the three plots to the east and west. Plot values were averaged among the four replications to generate an entry mean. The entry means was used for all statistics. A subroutine SAS 9.4 (SAS, Cary, North Carolina, USA) PROC CORR function was used to evaluate if there was a significant interaction between PI collected from the ground-based unit and sUAS with SDS score as well as maturity. SDS score components, severity, and incidence were compared to PI for correlation strength. Results could be used for implementation on large-scale applications such as farming operations.

PROC REG was used to calculate a linear regression using the reflectance indices to predict SDS score. All models were created using daily entry means of created indices. R statistical software was used for 2017 data to generate ANOVA tables and Spearman's Rho correlation values. PI, GNDVI, and BNDVI, derived from aerial imagery generated using a modified broadband camera, were compared to SDS scores to assess the relative performance these VIs as indicators of SDS. FD2 and FD3 were used for comparison, as they were the closest to maximum symptom expression. SDS score, severity, and incidence are compared to PI for correlation

Results/Discussion

PI Comparison

PI exhibited the best correlation between GNDVI, BNDVI, and PI when compared to SDS score for FD2 and FD3. GNDVI did not prove to be statistically significant for either FD2 or FD3 ($P = 0.4861$ and $P = 0.77$, respectively). GDNVI was not differentiable among high and low SDS scores. SDS infected plants showed the same GNDVI value as healthy plants. BNDVI showed statistical significance for both days ($P < 0.0001$ and $P = 0.0001143$, respectively); however, the correlation values were low (Table 3.3).

Table 3.3 - Spearman's Rho of GNDVI, BNDVI, and PI for FD2 and FD3. Statistically significant values (P < 0.001) are noted given an asterisk

	GNDVI	BNDVI	PI
FD2	-0.0838	-0.3627*	-0.7916*
FD3	-0.0743	-0.3500*	-0.7163*

Aerial and ground-based data comparison

Strong correlation between PI and SDS scores within the 2016 check plots was observed with the PI maps. PI had a slightly stronger correlation ($R^2 = 0.7974$) with SDS scores as compared to ground-based data ($R^2 = 0.7809$), however both showed statistical significance with $P > 0.0001$. In comparison to PI derived using aerial imagery, the ground-based data exhibited a strong correlation to SDS scores ($R^2 = 0.7809$), which was similar to correlation derived from the aerial imagery. Additionally, analysis of only high SDS (SDS scores of ≥ 25) instances using PI derived from ground-based and sUAS aerial imagery indicated significantly higher correlation with $R^2 = 0.8359$ when utilizing aerial imagery as compared to one from the ground-based data

($R^2 = 0.7114$). The greater accuracy of aerial imagery could be because of minimal environmental factors influencing the data quality. Aerial data takes considerably less time to collect (average flight time of approximately 11 minutes) than ground-based systems. During this time, there is minimal change in the temperature, solar angle, wind, and cloud cover compared to ground-based systems. Short flight time also captures a better understanding of the entire field at once rather than over several hours.

A regression equation fitted to the check plots was used to predict SDS score in the remaining plots from the PI map, Figure 3.5. The prediction is graphed against the actual SDS score to assess the accuracy of the prediction. Both ground-based and PI-based models showed low prediction values. However, these data are used to determine the next generation in planting.

In soybean breeding programs phenotypic evaluation is one of the largest restraints in breeding new lines. The ability to use sUAS to collect data increases the amount of line that can be evaluated in a given year. Both the ground-based and aerial PI for the check lines produced highly correlated regression equations, $R^2 = 0.7809$ and $R^2 = 0.7974$ respectively. This equation can then be used to predict the performance of the experimental lines. SDS estimates could be made using the regression equation produced by the data collected for on the checks. These predicted values can then be used as the basis of selection. Selections can be made using the predicted SDS score of the checks as the selection criteria. Elimination of lines with a lower predicted SDS score than that of the susceptible parent (IA3023). This method would allow an increase in the number of lines being evaluated by reducing the number of lines that would need to be physically rated for disease by the breeder, to just the parental lines and the SDS checks. This method would be most useful in early generation screening of large amounts of materials. The material would then have to be evaluated by the breeders for resistance before release to ensure the true resistance of the material to SDS.

Ground-based data display an overall more accurate prediction because specific wavelengths are selected for the BNDVI and GNDVI based on wavelengths that reflect the strongest in each band. The specific wavelengths selected allow little noise to occur in the data. Further, wavelengths presenting the most production and strongest correlation were selected, when available. Aerial data utilize all wavelengths within each band available to calculate the BNDVI and GNDVI. This can lead to error because excess wavelengths create noise. This becomes abundantly apparent in Figure 3.5 as ground-based data appear to predict twice as well.

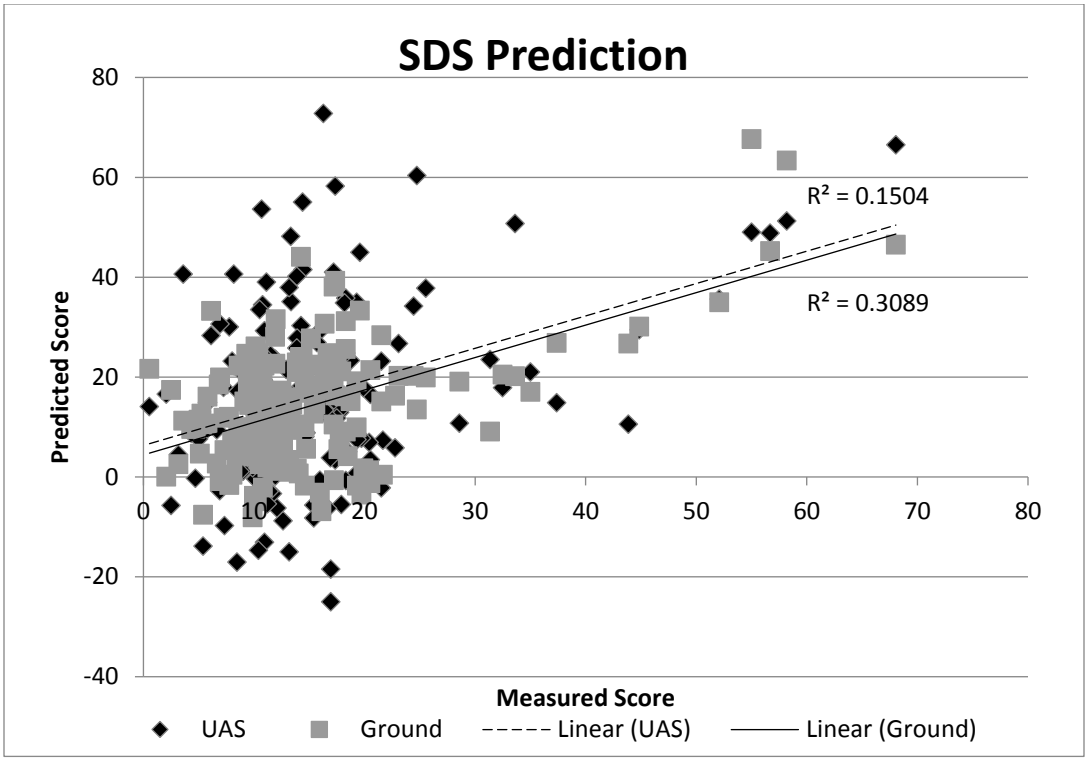

Figure 3.5 - Prediction accuracy based on regression created from resistant and susceptible check plot data

2017 Field Data

Aerial accuracy of check plots exceeded that of ground-based systems. For aerial assessment of SDS to be practically applied, the whole field must display a correlation of PI to SDS score. The whole field analysis to quantify SDS using SDS scores from select sites in 2017 indicated strong correlation as well with $\rho = -0.7916$ (Figure 3.6) for FD2 and $\rho = -0.7163$ for FD3 (Figure 3.7). Both FD2 and FD3 proved statistically significant with P-values less than 0.0001.

SDS score was further analyzed by breaking SDS score into its components, severity, and incidence. Individual components correlation to PI was determined for additional accuracy. Severity presented the highest correlation, even higher than SDS score, Figure 3.8 and Figure 3.9. FD2 displayed lower variance and higher correlations with $R^2 = 0.6313$ and $\rho = -0.8016$. FD3 displayed $R^2 = 0.5153$ and $\rho = -0.7389$. Both variance and correlation are improved from the SDS score for both days. Incidence presented the lowest correlation and highest variance for both days among the values seen in Figure 3.10 and Figure 3.11. FD2 presented Spearman's rho of $\rho = -0.7185$. FD3 dropped to a spearman's rho of $\rho = -0.6774$.

Breeding applications will eliminate the plots with the worst response to SDS to increase resistance for the next season. In 2016, only 16 of the 160 plots scored high for SDS infection, as a result, the 2017 data was used to assess the ability for SDS to quantify high plots for elimination. The top 50% of the plots with the highest SDS scores were selected. SDS scores ranged from 93.83 to 29.60. PI from FD2 recognized 80.0% of top plots in the analysis. FD3's PI values accounted for 78.75% of the plots.

The decrease in correlation from FD2 to FD3 can be accounted for based on the senescence of the plants. R6 occurs very close to maturity of the soybeans. Within 10 days of R6, plants are reaching maturity and as a result, photosynthesis in the plant is slowing. The PI cannot differentiate between low PI caused by high SDS infection and senescence of the plant. PI is a good indicator of SDS however, it is important to use it at the proper growth stage. The comparison of results from the two FD in 2017 showed that PI can provide stronger correlation to SDS if the aerial imagery is collected when SDS leaf systems are fully visible and before plant senescence. The results from the whole field analysis showed that the aerial imagery approach could be useful on a field scale to quantify SDS.

Further, severity shows the strongest correlation of SDS ($\rho = -0.8016$ and $\rho = -0.7389$). The strong correlation and small variance lead severity to a strong case. Large-scale operations will not take into consideration the incidence of infection because small plots are not planted on large grow operations. Farming operations will not determine the amount of SDS present, only that SDS is present. Once SDS presence is determined in a field mitigation steps will be taken to decrease the impact of SDS on yield. While SDS score and incidence are great disease indicators for small research plots, they are not practical over a large field. However, severity is applicable no matter the size of the field.

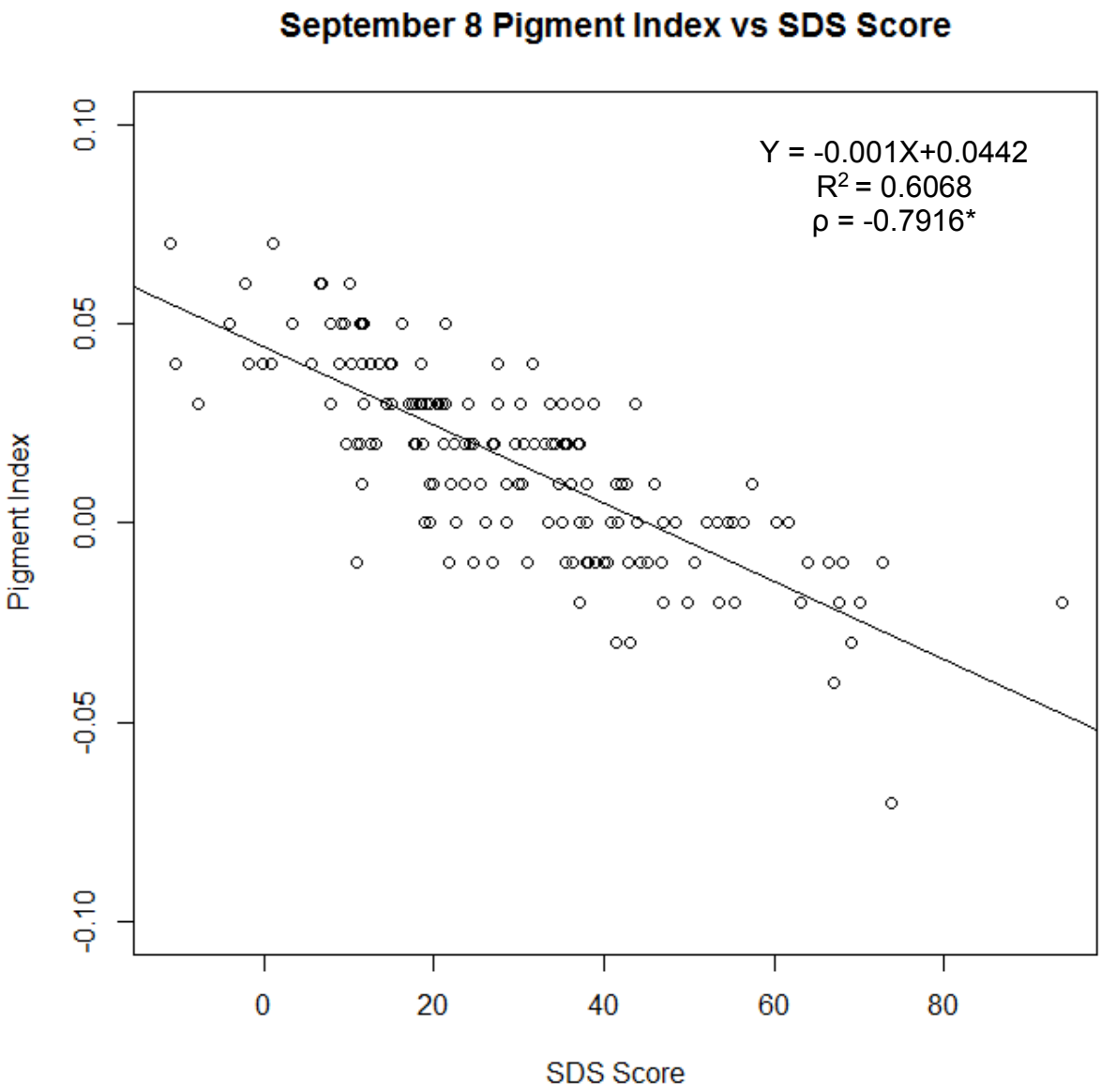

Figure 3.6 – 8 September 2017 PI comparison with SDS score. The equation for line of fit, R^2, and Spearman's rho (ρ) are given. Correlation coefficients that statistically significant ($P < 0.0001$) are indicated by an asterisk.

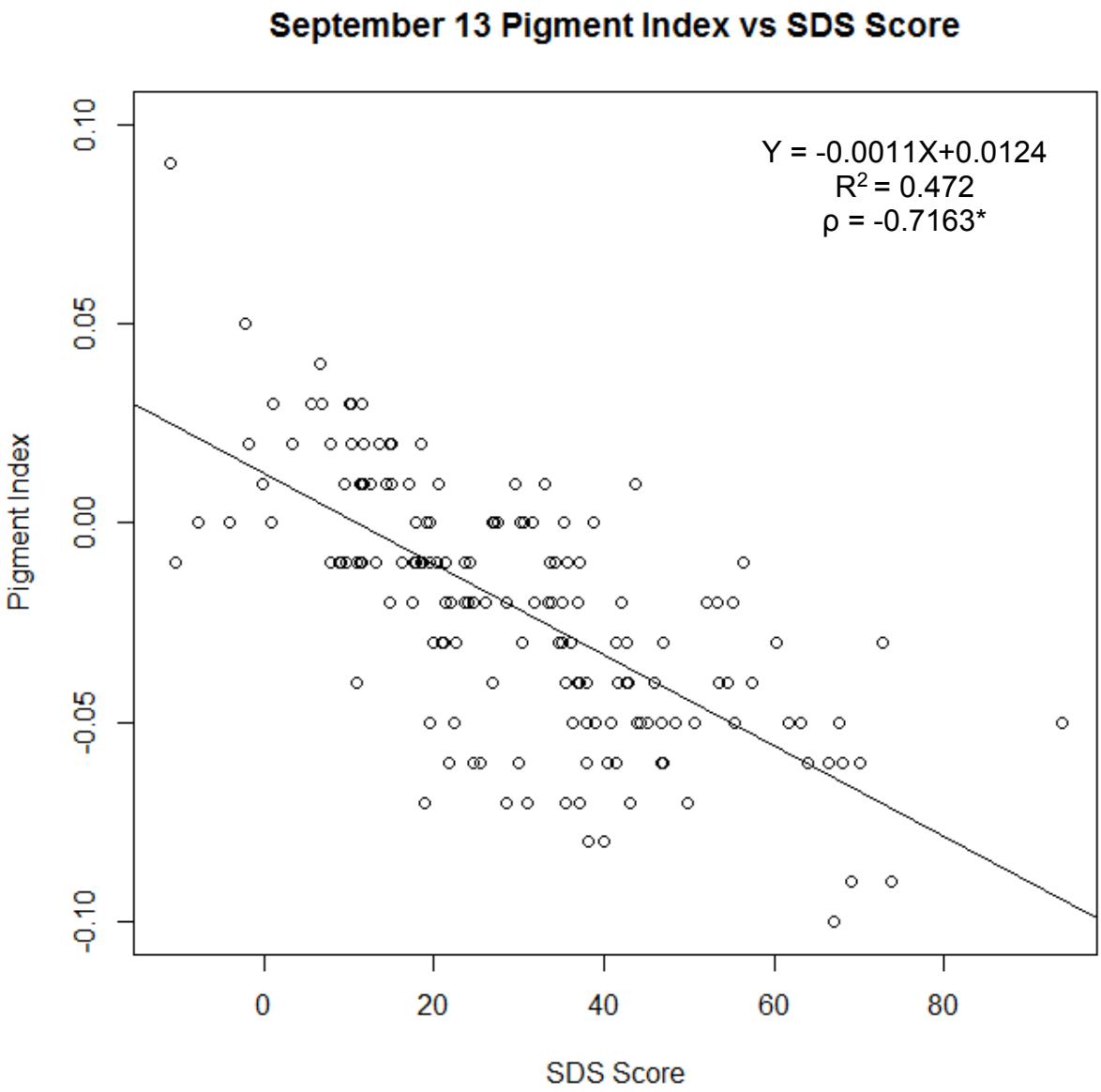

Figure 3.7 – 13 September 2017 PI comparison. The equation for line of fit, R^2, and Spearman's rho (ρ) are given. Correlation coefficients that statistically significant ($P < 0.0001$) are indicated by an asterisk.

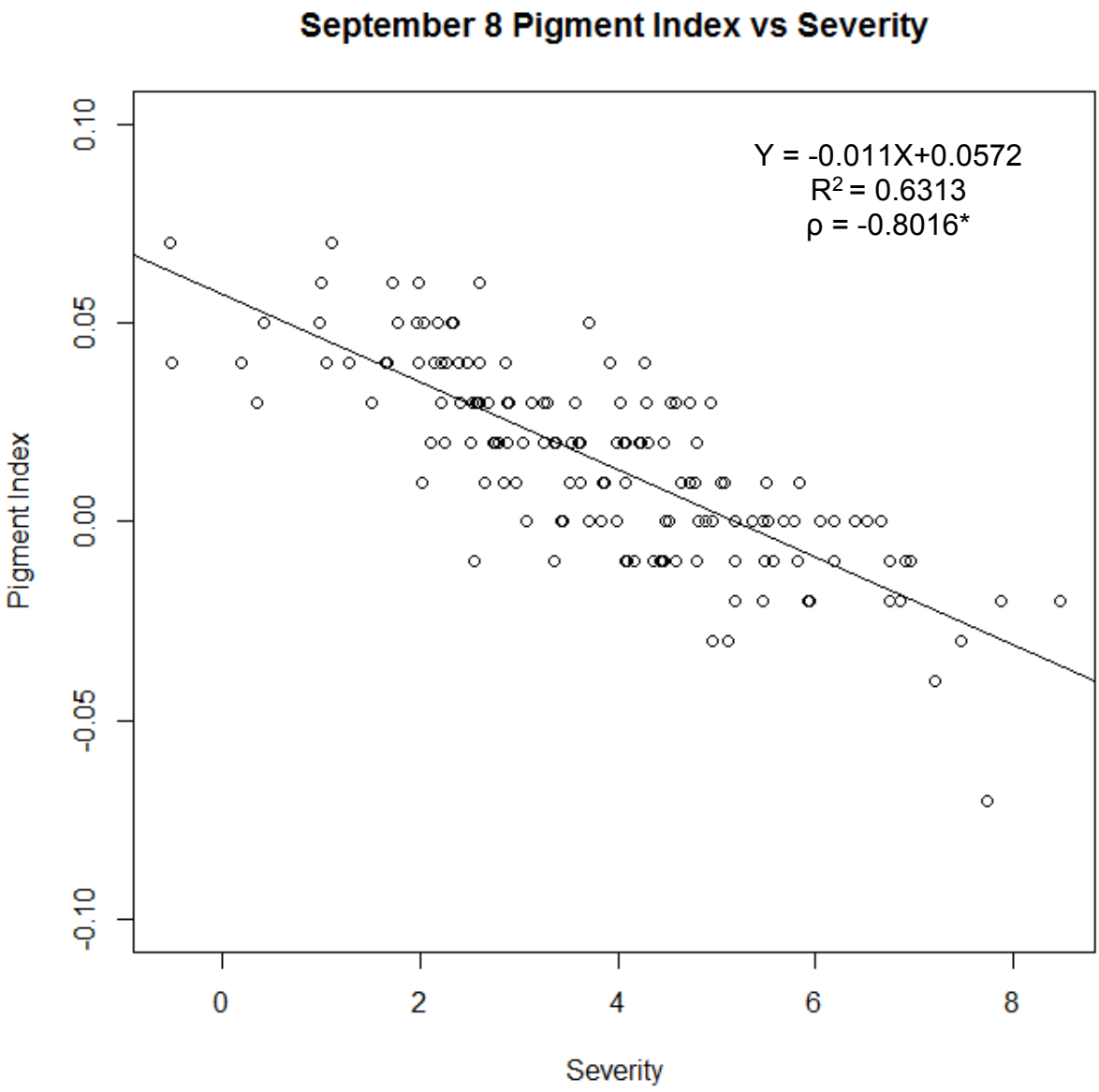

Figure 3.8 – 8 September 2017 severity as compared to PI. The equation for line of fit, R^2, and Spearman's rho (ρ) are given. Correlation coefficients that statistically significant ($P < 0.0001$) are indicated by an asterisk.

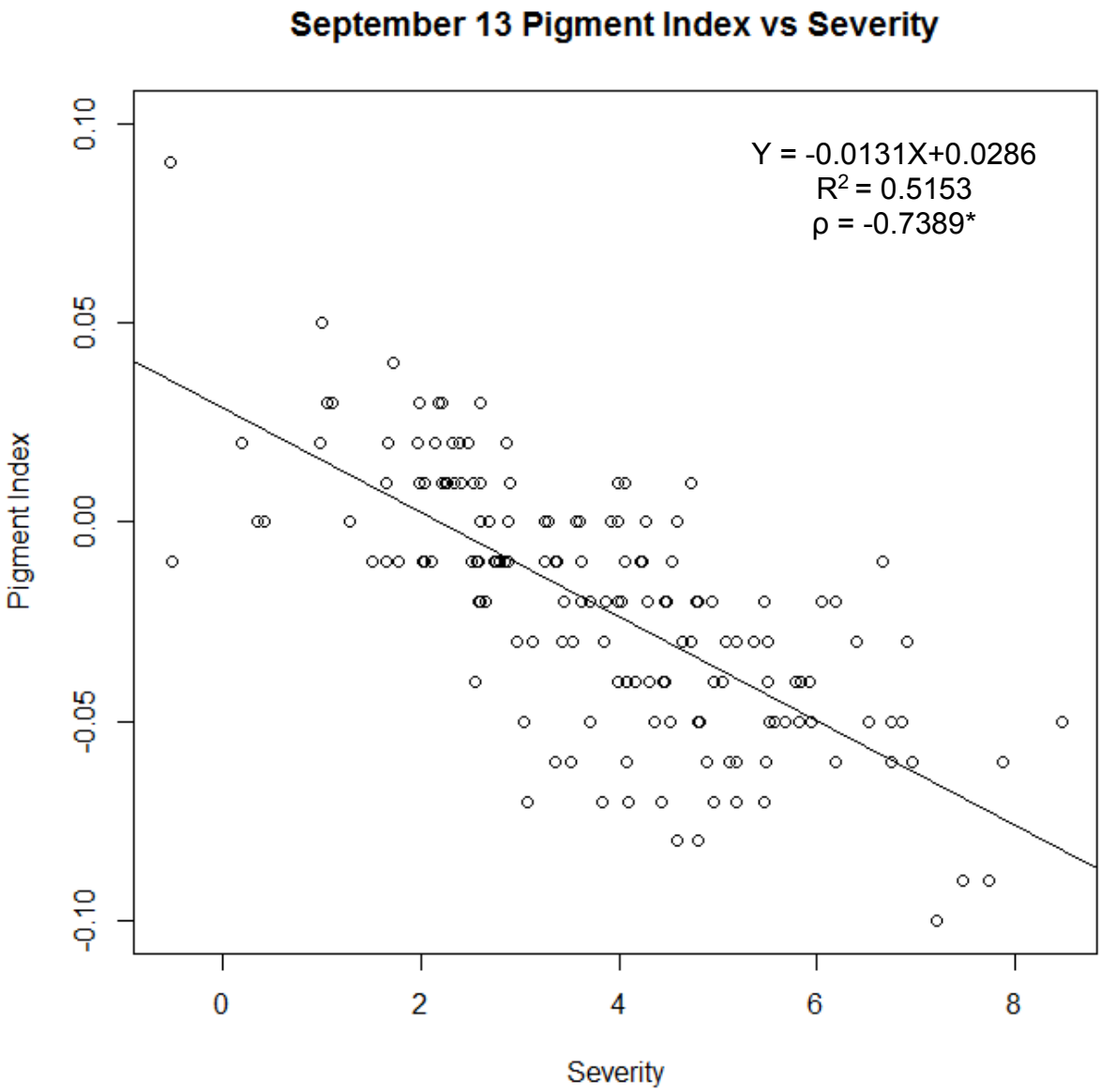

Figure 3.9 – 13 September 2017 severity as compared to PI. The equation for line of fit, R^2, and Spearman's rho (ρ) are given. Correlation coefficients that statistically significant ($P < 0.0001$) are indicated by an asterisk.

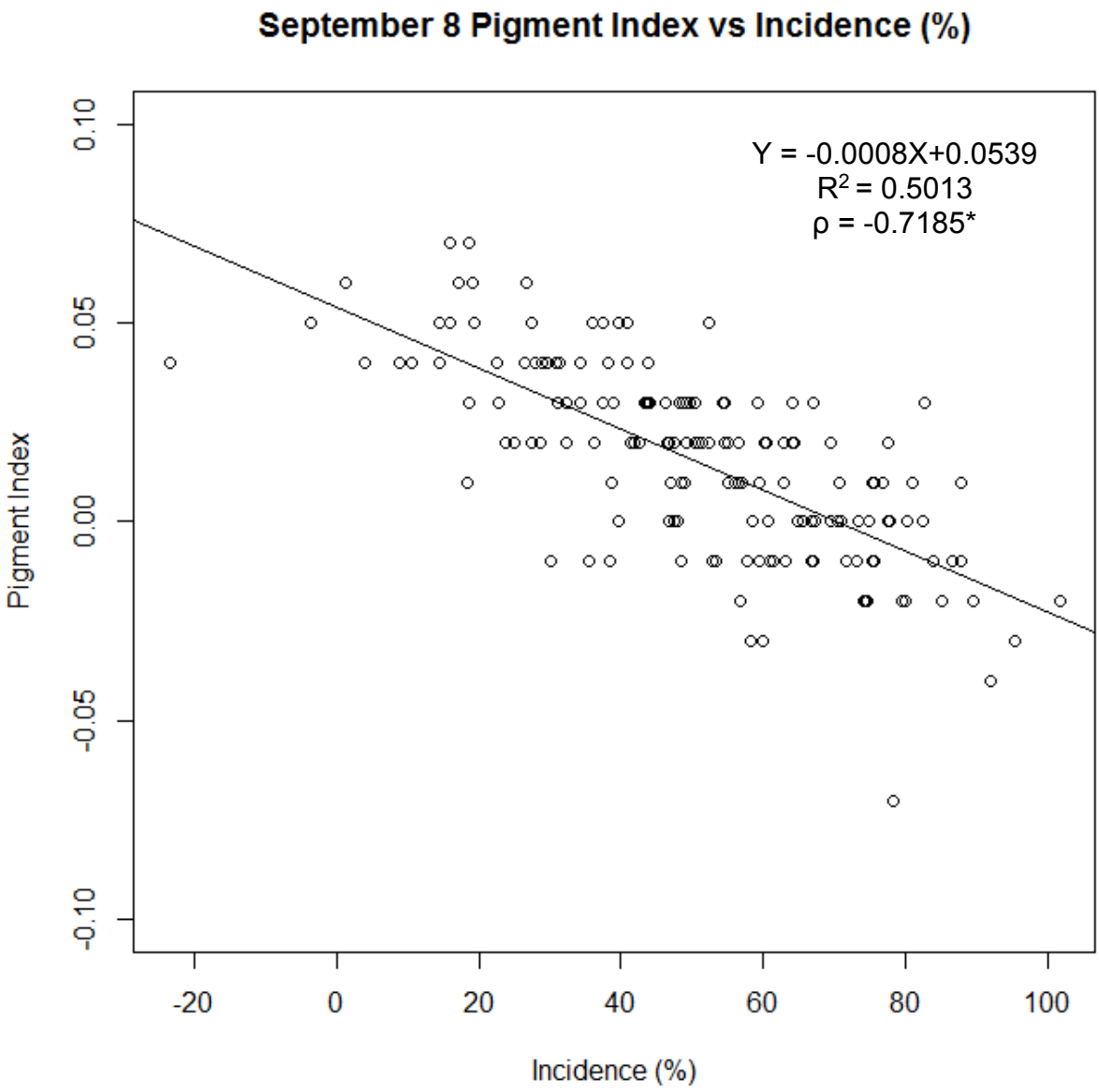

Figure 3.10 – 8 September 2017 incidence as compared to PI. The equation for line of fit, R^2, and Spearman's rho (ρ) are given. Correlation coefficients that statistically significant ($P < 0.0001$) are indicated by an asterisk.

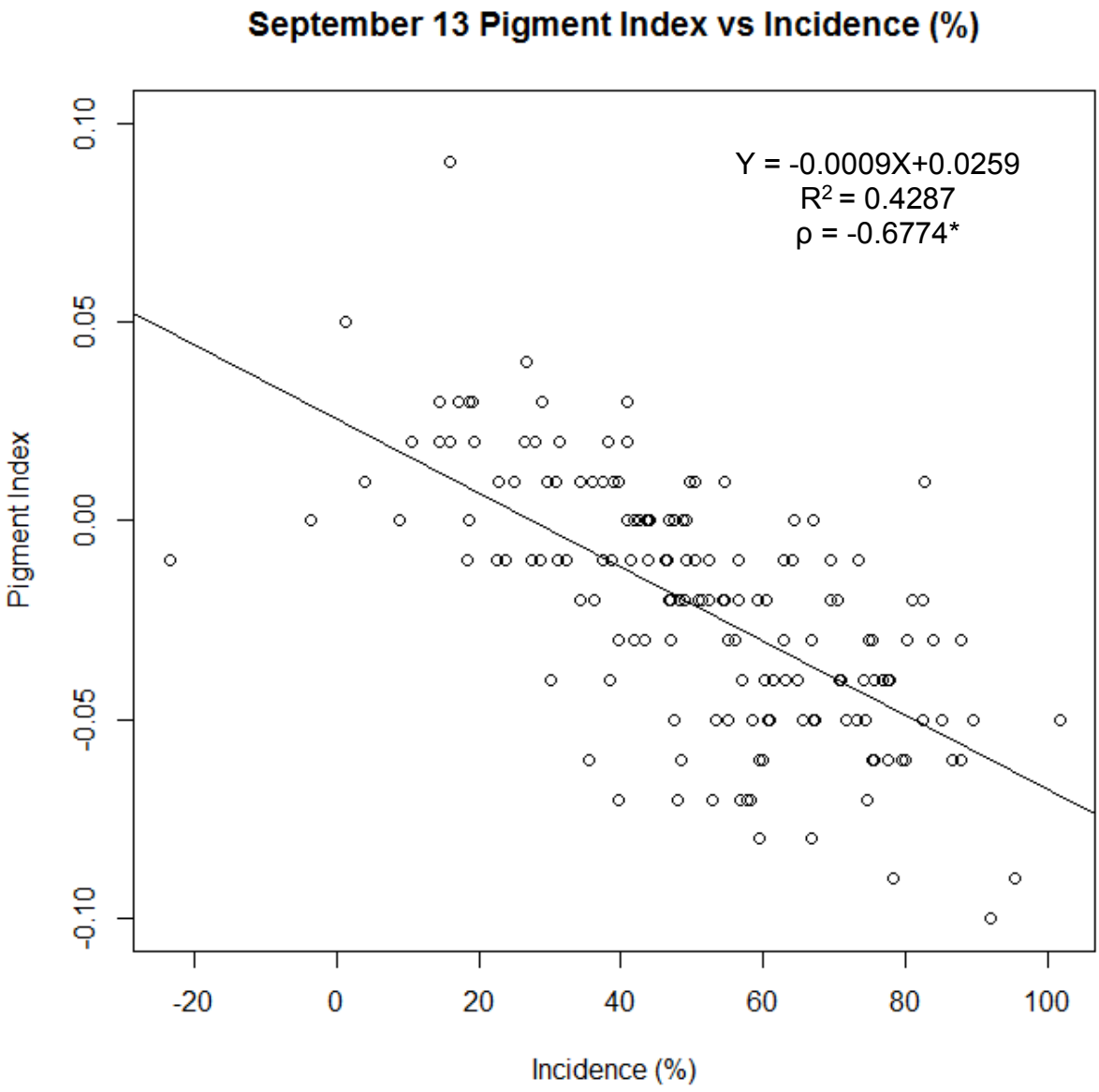

Figure 3.11 – 13 September 2017 incidence as compared to PI. The equation for line of fit, R^2, and Spearman's rho (ρ) are given. Correlation coefficients that statistically significant ($P < 0.0001$) are indicated by an asterisk.

High SDS Instances

SDS score was plotted against the PI for ground-based and aerial platforms to assess the accuracy of high instances of SDS. Aerial very accurately assesses high SDS from the PI with an R^2=0.8359. Ground-based PI also predicts high instances of SDS, however, it is considerably lower than aerial platforms at R^2=0.7114, Figure 3.12.

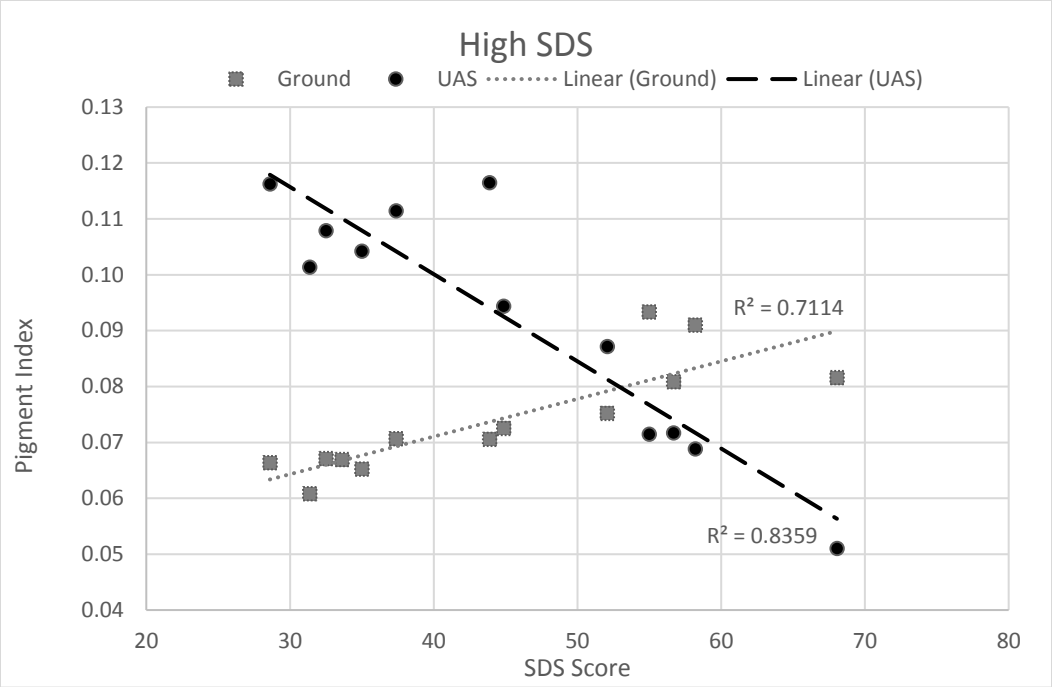

Figure 3.12 - High SDS score comparison to ground-based and aerial derived PI

The ground-based system seemingly predicted SDS score better than the aerial system based on FD1 however, the high SDS scores display that the aerial platform performed much better than the ground-based unit. The analysis of high scoring SDS further supports the use of aerial platforms. Aerial data are able to detect the high scoring cases of SDS more accurately than the ground-based unit ($R^2 = 0.8359$). Accuracy gives the breeder assurance that the undesirable genotypes will not be used for further breeding. The accuracy of the high instances of SDS also supports the elimination of the ground-based unit for the 2017 season and focusing on further improving the accuracy of aerial imagery.

sUAS data showed a negative correlation between PI and SDS score while ground-based data show a positive correlation. High SDS scores should show low PI values based on the definition of PI. The positive relationship between ground-based PI and SDS score is believed to be caused by the ground-based system. The ground-based system shows little variation in the NIR reflectance values. Aerial data show large changes in the NIR reflectance depending on the plant health while ground-based data does not show the same change in NIR reflectance. This means that PI greatly is influenced by the blue and green reflectance causing a positive relationship with SDS score. The ground-based system shows the same effects in reflectance over multiple years of data. This further supports the use of an aerial assessment of PI over ground-based methods.

Maturity

Plots maturity dates were taken as a metric of harvest. Plots matured as early as 15 days to a late as 34 days, after 31 August. FD2 exhibited a strong correlation of $R^2 = 0.6035$ and $\rho = 0.7887$, Figure 3.13. FD3 saw a drastic increase in the correlation at $R^2 = 0.7395$ and $\rho = 0.8824$, Figure 3.14. This is only two days before the first plots reach maturity.

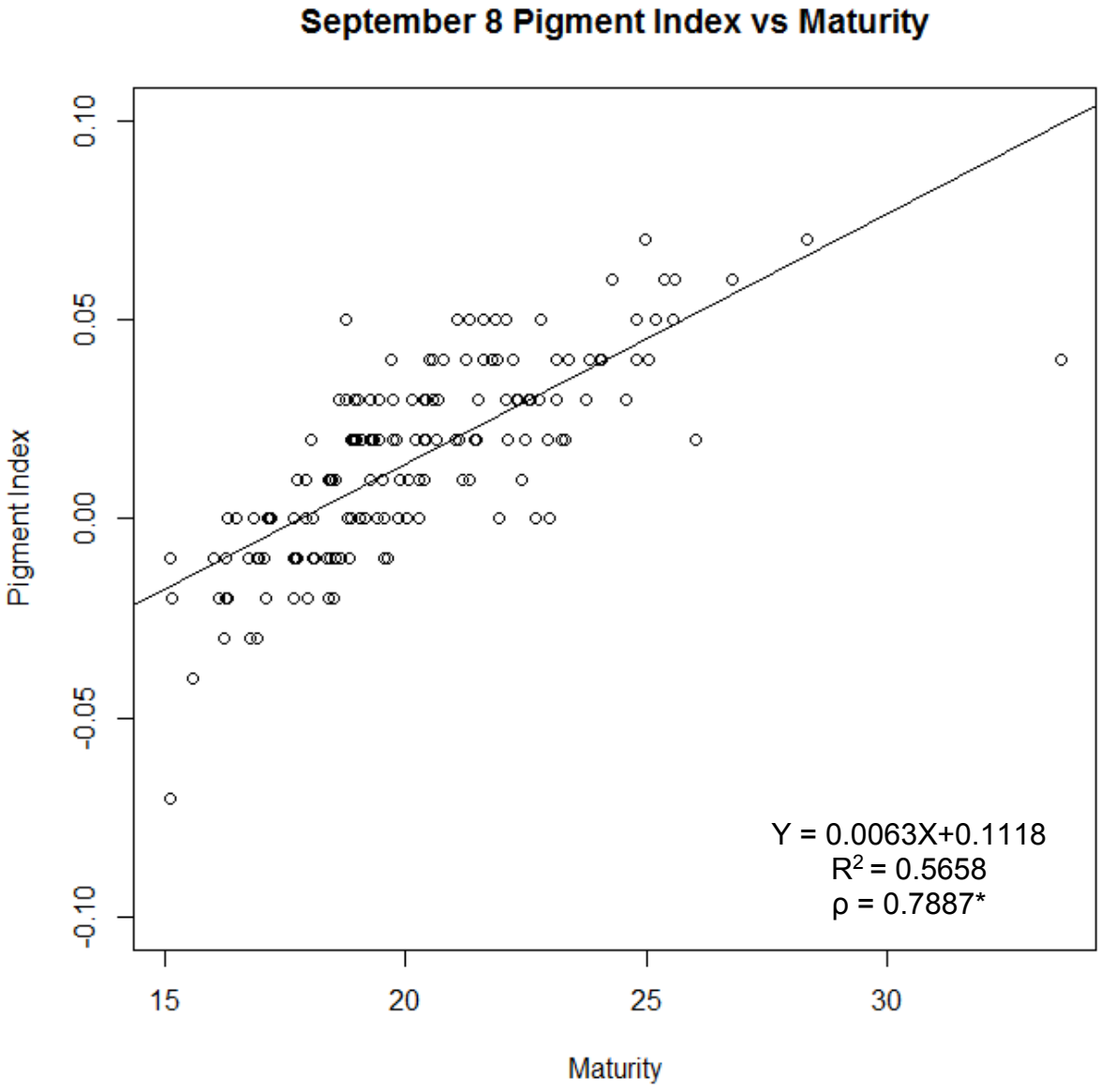

Figure 3.13 – 8 September 2017 maturity comparison to PI. The equation for line of fit, R^2, and Spearman's rho (ρ) are given. Correlation coefficients that statistically significant ($P < 0.0001$) are indicated by an asterisk.

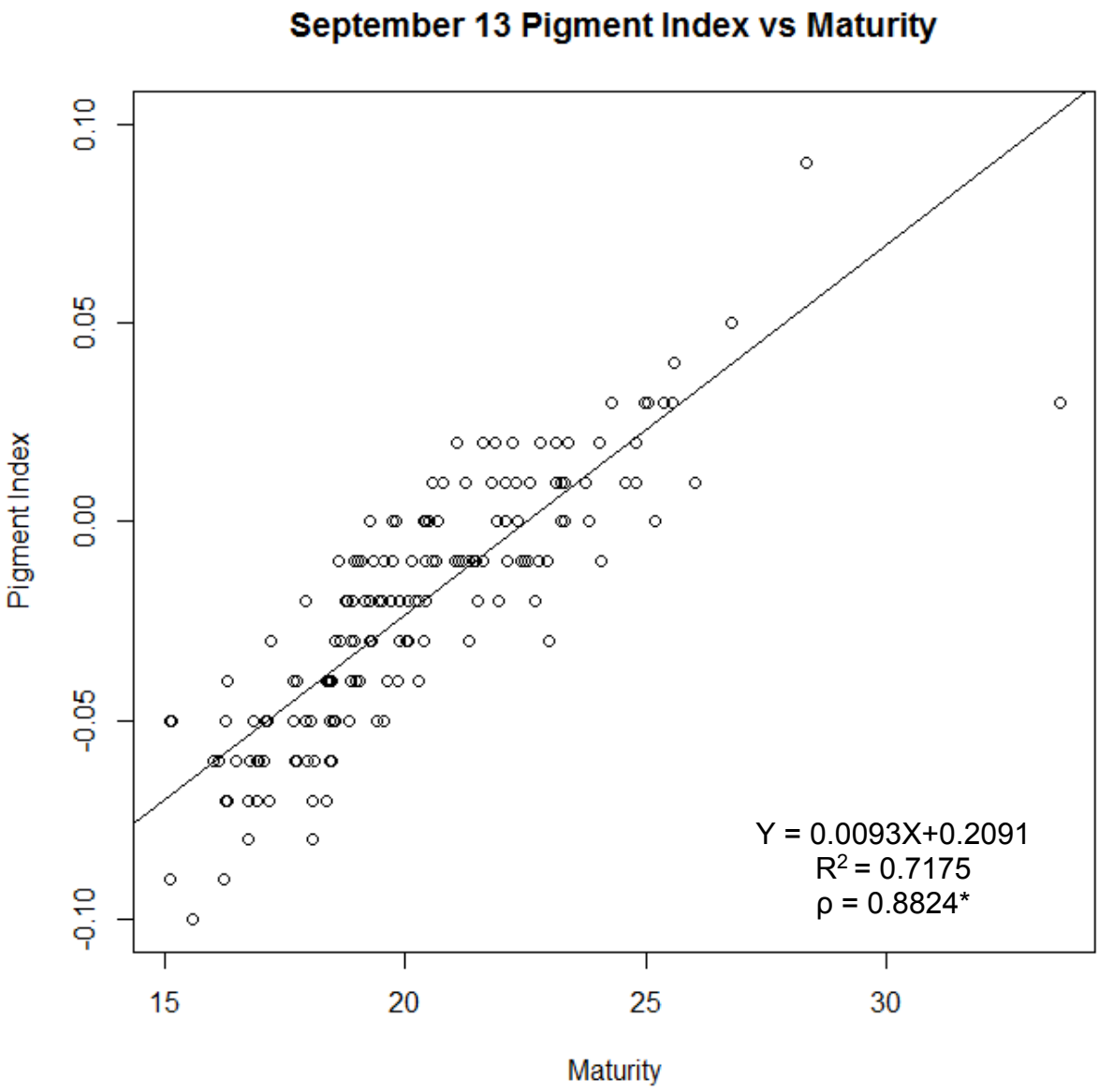

Figure 3.14 – 13 September 2017 maturity comparison to PI. The equation for line of fit, R^2, and Spearman's rho (ρ) are given. Correlation coefficients that statistically significant ($P < 0.0001$) are indicated by an asterisk.

As plant mature the metabolic processes slow, commonly referred to as senescence. PI not only acts as a measure of plant stress but also as a measure of photosynthetic activity relating to maturity. Mature plants will have little to no photosynthetic activity occurring. Photosynthesis occurring in plant cells slows until maturity is reached reflected by lower PI values. The closer to maturity of the plant the less photosynthesis occurs in plant cells. Low photosynthetic activity ties to low chlorophyll a and b within the plant. PI values decrease as the concentrations of chlorophyll

a and b decreases. FD3 showed stronger correlations of PI to maturity than FD2. The proximity to maturity reduced the measured PI resulting from reductions in photosynthesis and chlorophyll a and b production. The closer to senescence the plant gets the more accurately the PI correlates to the final maturity date.

Area coverage

The strong correlation between PI and SDS scores indicated that the aerial imagery could be used to derive PI for quantification of SDS on soybean. The comparable results from aerial imagery and ground-based data also indicated that sUAS aerial imagery based PI can provide comparable results to quantify SDS. The sUAS aerial imaging system can potentially cover much larger area compared to the ground-based system within a time duration available in a day. The aerial systems presented in this study are capable of covering approximately 6 hectares per hour while the ground-based system presented is only capable of 0.33 hectare per hour. The reduction in time spent on SDS assessment translates to increased productivity. sUAS provide the opportunity to breeders to conduct high spatial and temporal studies covering greater study plots to study breeding lines during the growing season.

Conclusion

This study proved that aerial SDS assessment using a sUAS is statistically useful, comparable to ground-based methods, and SDS is quantifiable from aerial platforms over a whole field. PI acts as an indicator of SDS indirectly correlating to SDS presence. Aerial PI proved a strong negative correlation to the SDS scores for checks and high scoring SDS plots in 2016. Analysis of aerial PI proved comparable to ground-based PI as a detector of SDS. Decreased variability in the ground-based scores was explained with the selection of individual wavelengths in the calculation of ground-based BNDVI, GNDVI, and PI. Overall, aerial data was determined to be a faster, better, and more accurate indicator of SDS because of the reduction in time and environmental factors affecting ground-based collected data.

Aerial PI also presented a strong correlation over a whole field in the 2017 growing season. Individual components of SDS score, severity, and incidence were analyzed to assess their strength as measurements of SDS. SDS severity maintained the least variability and highest correlation to PI across the 2017 data including SDS score. PI detection of severity is a promising indicator of SDS and applicable across all field sizes including large farming operations. Further, PI presented

a strong correlation to the maturity of plots. PI not only acts as an indicator of plant health but also plant senescence and maturity. Future studies will include an early assessment of SDS to determine if SDS is detectable through CIR imagery before visible symptoms appear.

Chapter 4 - Remote thermal infrared imaging for rapid screening of sudden death syndrome in soybean

Nicholle Hatton[1], Ajay Sharda[1], William Schapaugh[2], Deon van der Merwe[3]

[1]Department of Biological and Agricultural Engineering, College of Engineering; [2]Department of Agronomy, College of Agriculture, Kansas State University; [3]Department of Farm Animal Health, Faculty of Veterinary Medicine, University of Utrecht

Abstract

Sudden death syndrome (SDS), a fungal infection in soybeans caused by Fusarium virguliforme, greatly affects the plant health and in some cases, can cause yield losses of more than 70%. Infected plants are scored by visual assessment based on severity and extent of infection. This manual process is time intensive and not practical for large acreages. Diseased and stress in plants show elevated canopy temperatures that can potentially lead to identification of unhealthy plants without manual scoring. The infection decreases nutrient distribution causing stress that results in internal plant temperature to increase. Thermal infrared (TIR) sensors have the ability to measure the emitted radiation of an object in the infrared region of the electromagnetic spectrum to estimate canopy temperatures. However, TIR sensors have not yet been utilized to capture changes in canopy temperatures to detect SDS in soybean. Therefore, the goal of this study was to 1) use a TIR sensor to assess plant health and vitality, and 2) evaluate canopy temperatures over the growing season to quantify disease development. A thermal infrared camera was mounted on a small unmanned aerial system to capture aerial imagery over the growing season. The first flight was achieved once SDS foliar symptoms began initial development. The remaining three flights occurred before, during, and after full pod fill when symptoms had reached their apex. Results show increasing correlations over the four days. Elevated canopy temperature changes were observed on canopies at early SDS symptom development. Symptoms at the end of the growing season displayed strong correlations to the canopy temperature with ρ= -0.7114. Disease severity showed the strongest correlation throughout the four flights with the last at ρ= -0.7115. The four flights exhibit a decreasing trend with Spearman's rho (R^2=0.7859 for disease severity). Therefore,

thermal imaging can be utilized to detect diseased plots. Future studies will be conducted to understand how to mitigate for SDS using thermal detection.

Introduction

Sudden death syndrome (SDS), caused by *Fusarium virguliforme*, is an invasive fungus that targets the root system of soybeans. Since its discovery in 1971, SDS has spread to infect plants across the United States, South America, and Europe (Chong et al., 2005; Roy et al., 1997). Extreme cases of SDS can cause 100% yield loss and premature death of the plant; however, typical losses are between 20-50% of the predicted yield (Hartman et al., 1999; Roy et al., 1997). Currently, the only fungicide commercially available is ILeVO (Crop Science US, Bayer, Research Triangle Park, North Carolina, USA) used to help control SDS. Disease mitigation practices through irrigation scheduling and crop rotation are seen as the best management approach for disease prevention and minimization of yield losses. Financial impacts from SDS were estimated at $1.6 billion for 2016 (Manage soybean risks, SDS and SCN with ILeVO.2016).

SDS thrives in areas of heavy moisture and is most destructive in cool, wet soils (Westphal et al., 2006). Consistent soil temperatures between 55^0F and 65^0F create an ideal environment for SDS (Shrivastava et al., 2015; Westphal et al., 2006). Heavy summer rains contribute to the growth and migration of SDS throughout the field. SDS is found in concentrated areas within a field due to varying field and soil conditions (Roy et al., 1997). These areas are known as hotspots.

Symptoms of SDS begin developing in the roots causing a brown or grey discoloration. The development of this brown or grey discoloration limits the nutrient distribution through the plant by destroying the vascular tissue of the root system (Chong et al., 2005; Cui et al., 2014; Hartman et al., 1999; Roy et al., 1997; Shrivastava et al., 2015; Tang et al., 2010; Xing & Westphal, 2009; H. Zhang et al., 2013). Generation of nodes on the roots follows as the disease progresses (Chong et al., 2005). Foliar symptoms develop after flowering of the soybean. Light yellow chlorotic spots begin developing on the leaves of the soybean (Chong et al., 2005; Cui et al., 2014). The chlorotic spots grow to chlorosis, and finally, become necrotic (Hartman et al., 1999). The only remaining green on the plant leaves is found in the mid-veins and major lateral veins (Hartman et al., 1999; Tang et al., 2010). If allowed to progress, SDS will cause premature death of the plant with dropping of seedpods following the flowering stage. This causes loss in yield (Roy et al., 1997).

The plant experiences stress-induced nutrient deficiencies, caused by the initial root infection, in the early stages of SDS. Worsening of SDS will eventually prohibit normal plant functions,

namely evapotranspiration, to a point where the plant can no longer maintain homeostasis. These plants usually exhibit higher temperatures than healthy plants, which can provide a proxy for measuring SDS severity.

Thermal infrared (TIR) imagery measures an objects emitted radiation. The emitted radiation of an object can be used to derive the canopy temperature. Changes in the plant canopy temperature can be caused by stress, disease, and nutrient deficiencies. Mapping crop canopy temperature uses TIR imagery (Alves & Pereira, 2000; Ayeneh, van Ginkel et al., 2002; J. A. J. Berni, Zarco-Tejada et al., 2009; Espinoza et al., 2017; Luo et al., 2018; X. Wang et al., 2010). TIR imagery is also used in the estimation of biomass (Gunawardena & Fernando, 2016; Maimaitijiang et al., 2017; Wooster et al., 2013), prediction of yields (Guan et al., 2017; Hecker, Smith et al., 2013; Leroux et al., 2016), and assessment of fruit and crop quality (Berdugo et al., 2014; Sepulcre-Cantó et al., 2013; Sepulcre-Cantó et al., 2007; Zhao et al., 2005). Thermal evaluation of SDS for the determination of disease symptoms or severity has not yet been attempted. However, work from Berdugo et al. (2014), Calderón et al. (2014a), Chaerle et al. (2004), A. Mahlein et al. (2012), and Oerke et al., 2006 assess diseased and healthy plant temperatures under greenhouse conditions. These studies demonstrate that as early as two days after inoculation, temperatures of diseased plants can increase by 2^0C or more as the disease progresses (Chaerle et al., 2004; Oerke et al., 2006). Further work by Calderón et al. (2013) and De Carolis et al. (1974) took thermal imaging into fieldwork to assess early detection of diseases in olive trees and rice. Both studies demonstrated that early disease detection is possible when using elevated canopy temperatures as the main indicator between diseased plants and healthy plants (Calderón et al., 2013; De Carolis et al., 1974).

The aim of this case study is to 1) demonstrate that SDS infected soybeans exhibit elevated canopy temperatures, and 2) explore the temporal effects of disease progression using thermal imagery acquired by a small unmanned aerial system (sUAS).

Methods

An approach to compare SDS infected plants to healthy plants was established through the development of this case study. Naturally infected soybeans over a typical growing season served as the sample population for this study. The relationship between canopy temperature and SDS score is assessed over several days after canopy closure is reached.

Study Area

The study area is located at the Kansas State University, Kansas River Valley Experiment Field outside Rossville, KS (39.11852°, -95.92459°) and was selected for its prevalent SDS history. The dominant soil in the field is Eudora silt loam. Irrigation was applied throughout the growing season to maintain adequate soil moisture and to help increase the severity of SDS.

All plots had maturity and SDS ratings collected. Maturity was recorded as the number of days following 31 August when 95% of the pods on the plants had reached mature color. SDS ratings were taken at the R6 growth stage of the plants (Fehr et al., 1971).

The experiment consisted of a Nested Association Mapping (NAM) population comprised of 140 F_5 derived lines from a cross between IA3023 and LD00-3309 along with checks for yield, and agronomic traits and susceptible and resistant checks for resistance to Soybean Sudden Death Syndrome (SDS), for 160 entries. Four replications occurred for entries in the NAM population. The NAM population used a randomized complete block design using two-row plots 3.8 m long with 0.76 m between rows. The field was planted on 9 May 2017 into corn stubble and application of pre-emergence herbicide prevented early season weed growth. Postemergence herbicide applications and hand weeding controlled weeds throughout the season.

SDS Scoring

SDS was scored on two criteria, severity and incidence. Severity (Ds) addresses the severity of the SDS infection based foliar symptoms, on a scale of 0-9, as seen in Table 4.1. Incidence (Di) accounts for the percentage of the plot infected with SDS. Incidence ranges from 0% to 100% in 5% increments. Scoring occurred at growth stage R6. R6 is the growth stage where the seedpod cavity is filled, and seeds are just reaching full size. R6 is designated for SDS scoring due to the expression of the disease symptoms (Schmidt, 2007).

Table 4.1 - SDS severity scoring guidelines

Score	*Description of Symptoms*
0	No visual evidence of infection
1	1-10% of leaf surface chlorotic, OR 1-5% necrotic
2	10-20% of leaf surface chlorotic, OR 6-10% necrotic
3	20-40% of leaf surface chlorotic, OR 11-20% necrotic
4	40-60% of leaf surface chlorotic, OR 21-40% necrotic
5	Greater than 60% of leaf surface chlorotic, OR greater than 40% necrotic
6	Premature leaf drop up to 1/3 defoliation
7	Premature leaf drop up to 2/3 defoliation

8	Premature leaf drop GREATER than 2/3 defoliation
9	Premature death

Once severity and incidence for the plot have been assessed they are used to establish the SDS score (Dx) using Equation 4.1 (Nijti et al., 2001). Dx ranges from 0-100. Scoring occurred on 6 September 2017 for the plots in this study. The same individual, to reduce error, completed scoring. Dx scores above 25 indicate severe SDS infection.

$$D_x = \frac{D_i * D_s}{9} \qquad \text{Equation 4.1}$$

Where

Dx = SDS Score

Di = Incidence of infection

Ds = Severity of infection

Aerial Imagery

Aerial imagery was acquired using a sUAS coupled with a thermal camera designed for sUAS use. The IRIS+ (3DR, Berkeley, California, USA) in combination with a FLIR VUE Pro R 19 mm thermal camera (FLIR Systems, Wilsonville, Oregon, USA) captured imagery for this study. The thermal camera measures a spectral band from 7.5-13.5 μm.

Flight Planning

Flights occurred four times throughout the season on 28 August, 3 September, 8 September, and 13 September. Flights began at 12:00 p.m. on each day. A flight altitude 77 m above ground level (AGL) allowed a flight time of 7 minutes covering an area of about 1.8 hectares with a spatial resolution of 6.89 cm/pixel. Side lap was set to 75% while front-to-back overlap was set to 85% to achieve a one-second camera trigger interval. The sUAS was programmed to fly at a ground speed of 3 m/s. Based on the preliminary studies conducted with different ground speeds, the 3 m/s ground speed provided images with minimal blur.

Reference panels were instrumented to measure actual temperature and use it to calibrate canopy temperatures derived from images. Temperatures of reference panels were measured using surface-mounted thermistors (ON-930-44033, Omega Engineering Inc., Stamford, Connecticut, USA) with a measurement accuracy of ±0.1°C. Reference panels were painted black, grey, white

and another as a water bath. The different colored panels and water bath provided different temperature gradients for canopy temperature calibration. Laboratory experiments showed that reference panels have uniform temperature across the surface. Air temperature and humidity were gathered using a humidity/temperature transmitter (HX303AV, Omega Engineering Inc., Stamford, Connecticut, USA) with an accuracy of ±3% and ±0.2°C, respectively. Weather conditions for all flights were clear and atmospherically stable with minimal wind.

Data processing

Sixteen plots each with high (SDS score of 25 and over), medium (SDS score of 8-17), and low (SDS score of 0-5) SDS were randomly selected for comparison for a total of 48 plots. Independent images from each day were analyzed in FLIR Tools (FLIR Systems, Wilsonville, Oregon, USA) to derive the canopy temperature of each plot. Temperature was derived from the emitted radiation of the plot captured by the sensor. FLIR Tools used the target's emissivity, distance from the sensor to object (flight altitude AGL), relative humidity, and atmospheric temperature to derive the temperature. Emissivity was set at 0.94 nm (Guoquan & Zhengzhi, 1993; Rubio et al., 1997). Distance, relative humidity, and atmospheric temperature were set in camera settings in the field each day based on the daily conditions. Derived plot temperature was taken as the average temperature for that plot on a given day. The plots had complete canopy closure with no soil visible in the background; therefore the area of each plot was drawn to derive average plot canopy temperature. The derived canopy temperature for each plot was averaged over five images. The images selected were five consecutive images with target plot visible in the middle during a single pass of the flight (Figure 4.1 and Table 4.2). Averaging over five images eliminated bias that could occur due to changes in the angle between the canopy and sensor. The canopy temperature (Tc) was extracted for each plot for each day as the average canopy temperature over five subsequent images.

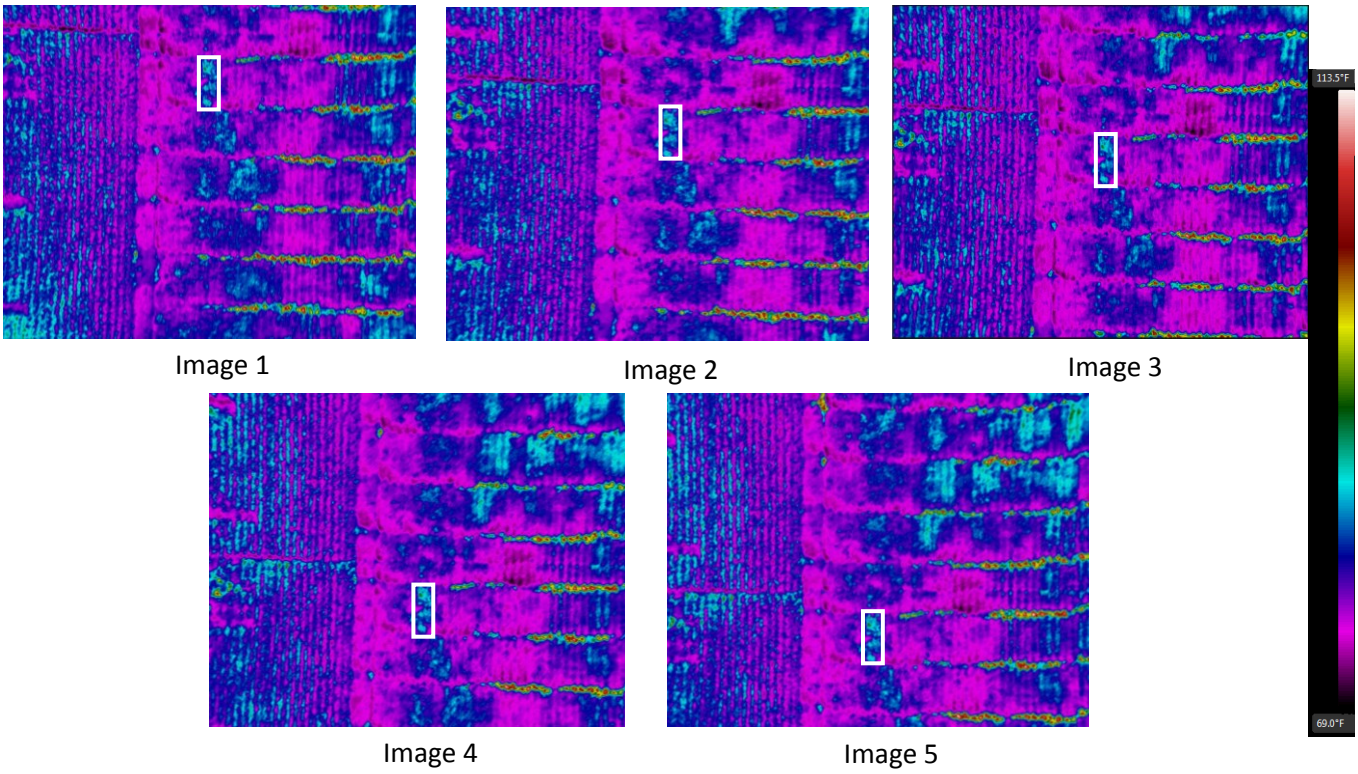

Figure 4.1 – Example sequence of image selection for calculation of average canopy temperature. Plot 121 circled to show relative position in each image.

Derived temperatures were calibrated with infield calibration panels to account for error in the derivation of temperature from emitted radiance. Measured panel temperatures and temperatures of panels derived from FLIR Tools were used to create a regression line for calibration of canopy temperatures.

Average air temperature during flight was used to normalize the canopy temperature due to the large range in daily temperatures occurring over the study period, similar to work by Berni et al. (2009), Calderón et al. (2013), and Calderón et al. (2014a). The temperature difference was found using Equation 4.2 given below:

$$T_{\Delta} = T_a - T_c \qquad \text{Equation 4.2}$$

Where

T_{Δ} = temperature difference

T_a = average air temperature during the flight

T_c = average canopy temperature

R statistical software was used to complete ANOVA testing and generate Spearman's rho correlations for each day.

Results

Average canopy temperature for all four flying dates varied between 62.6º F and 93.3º F, with standard deviation varying from 0.10^0F to 0.73^0F. Table 4.2 shows an example of the canopy temperature averaging over five images. Six plots (two low, two medium, and two high scoring) were chosen in the example. These results indicated the TIR sensor had a very consistent response to canopy emittance for series of images taken over the plots. It is also evident from the results that the canopy temperature was consistent when capturing canopy emitted radiation from different angles during a single pass of the flight. Overall, these observations exhibited that averaging of TIR image data may not necessarily give improved results during spatial analysis of aerial imagery.

Table 4.2 – Example average canopy temperature and standard deviation for two plots of each low, medium and high SDS from 3 September flight. Air temperature during flight was 82.4^0F (28^0C). Ta-Tc values shown in parenthesis.

SDS SCORE	PLOT	IMG 1 (^{0}F)	IMG 2 (^{0}F)	IMG 3 (^{0}F)	IMG 4 (^{0}F)	IMG 5 (^{0}F)	T_C (^{0}F)	STD DIV
0.0	302	77.8 (4.6)	77.8 (4.6)	77.5 (4.3)	77.5 (4.3)	77.8 (4.6)	77.7 (4.5)	0.16
0.6	4	76.5 (5.9)	76.6 (5.8)	76.9 (5.5)	75.8 (6.6)	76.2 (6.2)	76.4 (6.0)	0.42
10.0	24	79.4 (3.0)	79.5 (2.9)	79.5 (2.9)	78.0 (4.4)	78.5 (3.9)	79.0 (3.4)	0.69
11.1	101	78.8 (3.6)	79.1 (3.3)	79.5 (2.9)	79.3 (3.1)	79.4 (3.0)	79.2 (3.2)	0.28
85.0	165	82.7 (-0.3)	82.3 (0.1)	83.3 (-0.9)	82.6 (-0.2)	83.2 (-0.8)	82.8 (-0.4)	0.42
100.0	121	83.2 (-0.8)	81.8 (0.6)	82.3 (0.1)	83.1 (-0.7)	83.1 (-0.7)	82.7 (-0.3)	0.62

Temperature difference was compared to SDS scoring for each day flown to assess the relationship between temperature and SDS prevalence for each day. Each study period presented significance in the relationship between temperature and SDS score ($P < 0.0001$), incidence ($P < 0.02$), and severity ($P < 0.002$). Figure 4.2 displays the temperature difference of each day compared to SDS score. Analysis of each flight revealed a progression in correlation between temperature difference and SDS scores. Spearman's rho correlation increases throughout the growing season with a weak correlation observed for 28 August ($\rho = -0.2856$) and the strongest correlation observed for 13 September ($\rho = -0.7114$). Temperature difference exhibited a negative

correlation to the SDS score for each day, which implies that a lower temperature difference represents a higher SDS score. 8 September exhibited noticeably low-temperature difference values indicating canopy temperatures were above the air temperature. 8 September also exhibits a slightly lower Spearman's rho correlation and R^2 value in comparison to the flights before and after.

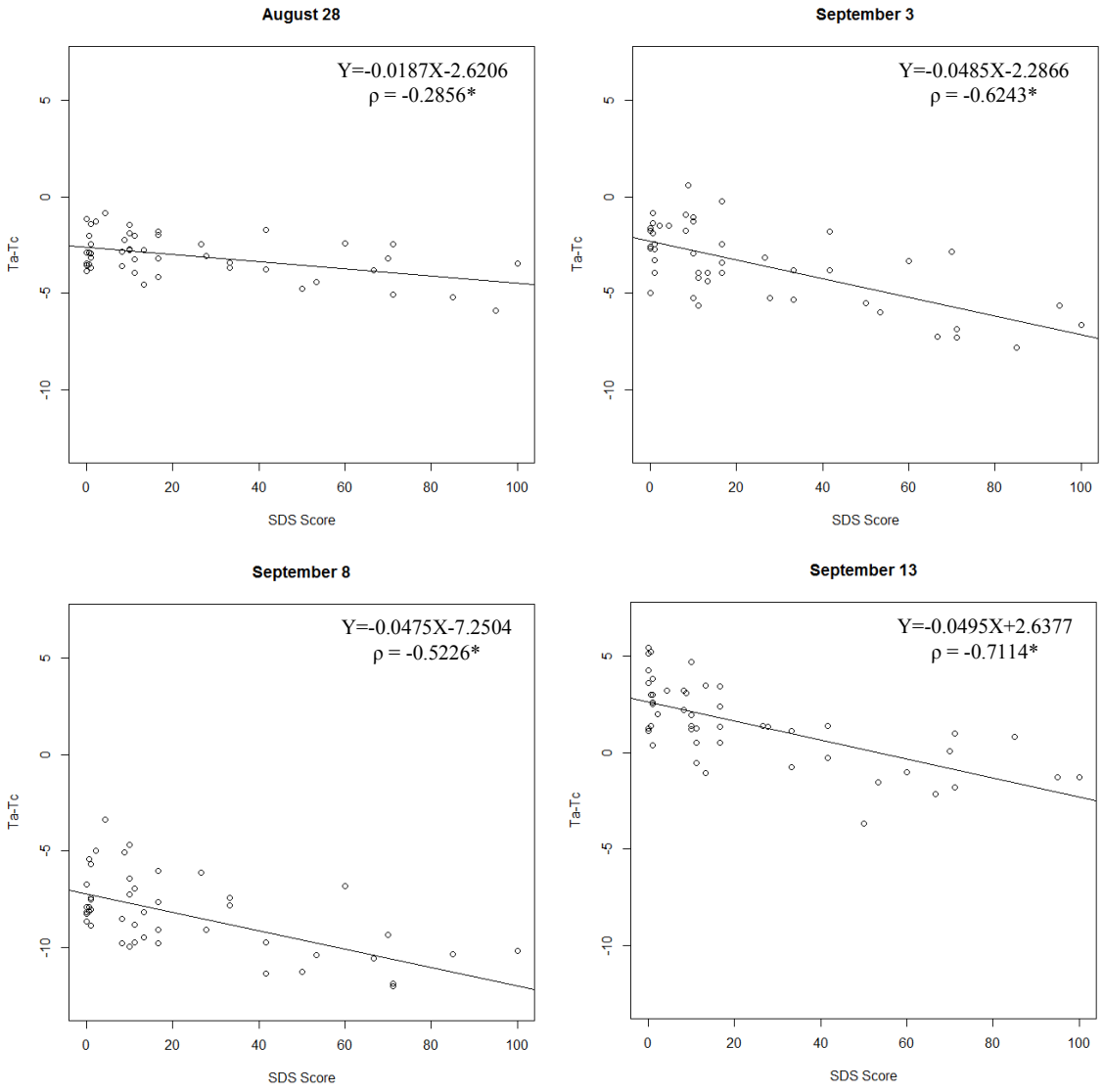

Figure 4.2 - SDS score to Ta-Tc (temperature difference) for each day of UAS flight. Equation for line of fit and Spearman's rho (ρ) are given for each plot. Correlation coefficients that were statistically significant (P<0.01) are indicated by an asterisk.

A strong correlation was observed between temperature difference and SDS severity and incidence for each of the four sUAS flights. Figure 4.3 and Figure 4.4 show the severity and

incidence, respectively, for each day of sUAS flight as compared to Ta-Tc (temperature difference). Both severity and incidence displayed similar statistical significance and correlation to the SDS score for a given day. As evident in Figure 4.2, both severity and incidence for 8 September displayed a much lower Ta-Tc (temperature difference) value compared to other days of flight. The lower correlation could be due to unseasonably cool nightly temperatures. This value also exhibits a negative correlation to temperature difference. The general trend for each day demonstrates that higher temperature reflected a greater extent of SDS infection in a plant within a plot. The overall increase in correlation demonstrates the progression of the disease over the growing season. Symptoms reach maximum expression by the end of the season. However, affected plots begin presenting significant symptoms two weeks earlier than typically measured with current assessment methods (i.e. SDS scoring). 28 August exhibited few visual symptoms of SDS but exhibited higher temperatures due to stress caused by SDS. Early detection of SDS infection could lead to increased yields as mitigation steps could be implemented before visual symptoms develop.

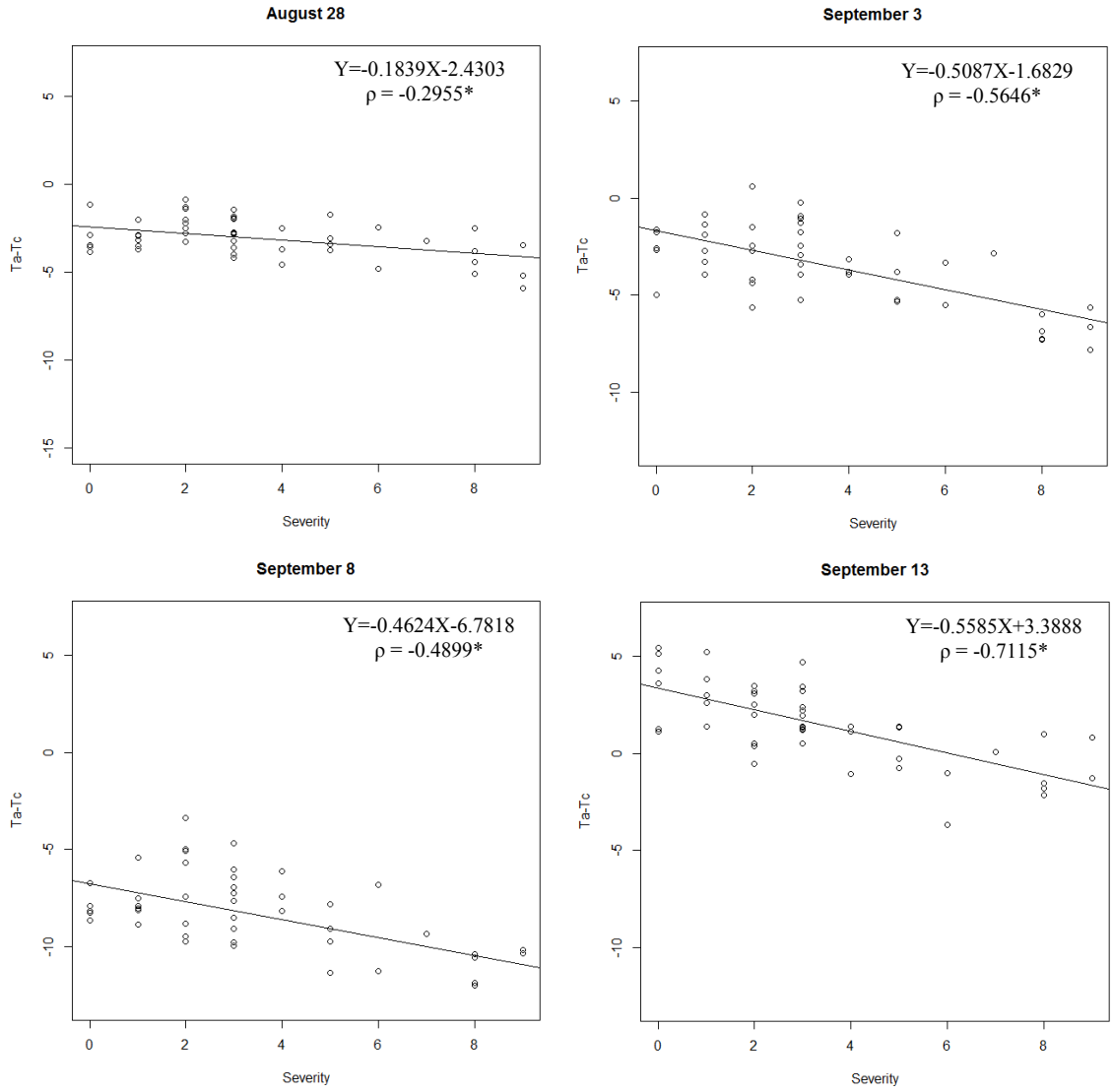

Figure 4.3 - Severity of infection to Ta-Tc (temperature difference for each day of UAS flight. Equation for line of fit and Spearman's rho (ρ) are given for each plot. Correlation coefficients that were statistically significant (P<0.01) are indicated by an asterisk.

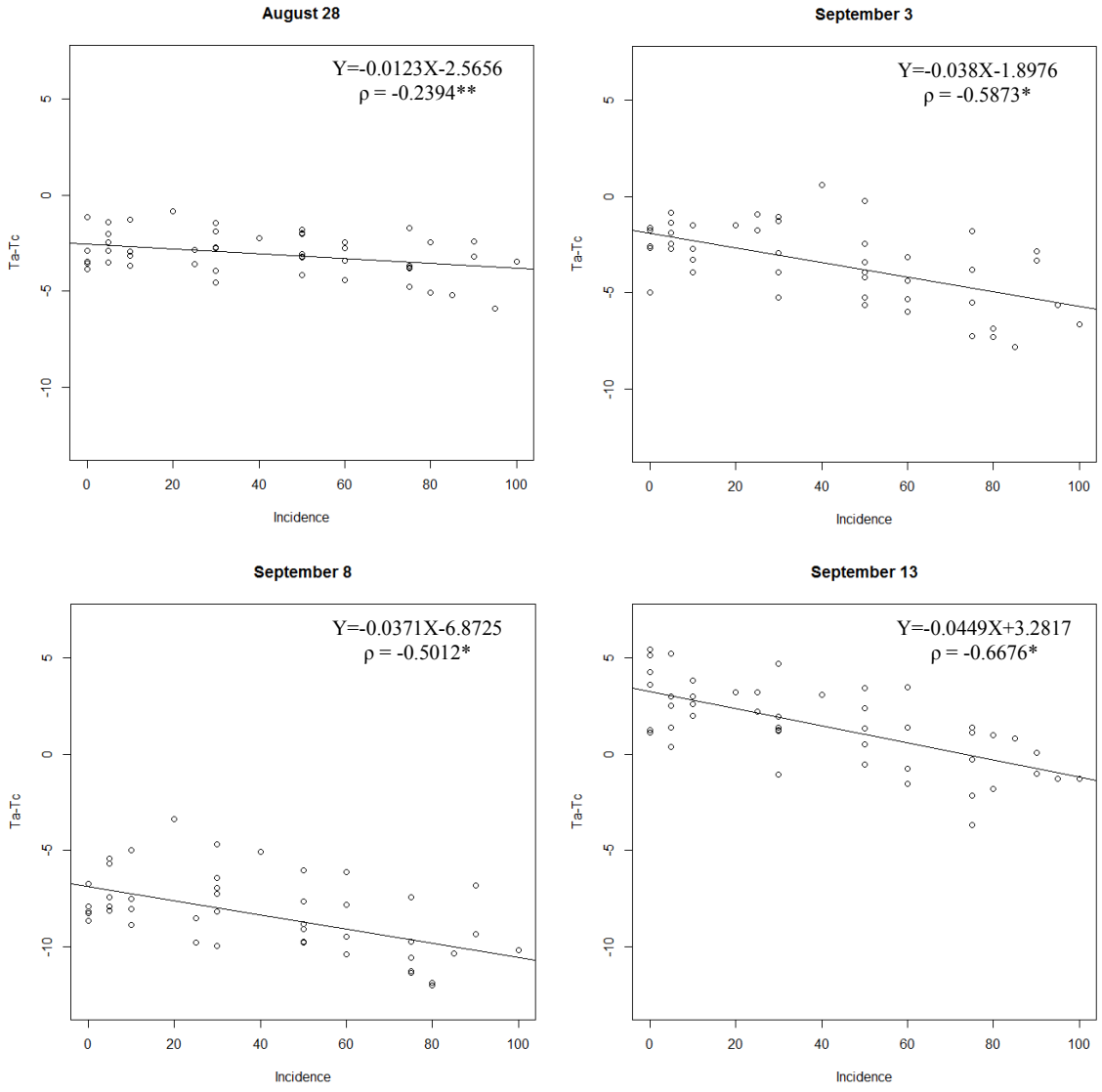

Figure 4.4 - Incidence of infection to Ta-Tc (temperature difference) for each day of UAS flight. Equation for line of fit and Spearman's rho (ρ) are given for each plot. Correlation coefficients that statistically significant (P < 0.01) are indicated by an asterisk and (P < 0.05) are indicated by a double asterisk.

Spearman's rho plotted for SDS score, severity, and incidence displayed with R^2 values of 0.7125, 0.7895, and 0.7268, respectively (Figure 4.5). Severity maintains the strongest relationship with R^2 at 0.7859. These graphs demonstrated how increasing temperatures led to increasing correlations as symptoms progressed. Symptom progression allowed for differentiation between temperatures of healthy and unhealthy plants. Early in symptom development temperatures of healthy plants and diseased plants showed little differentiation, however, as the disease progresses and symptom expression becomes greater the differentiation in temperature becomes stronger.

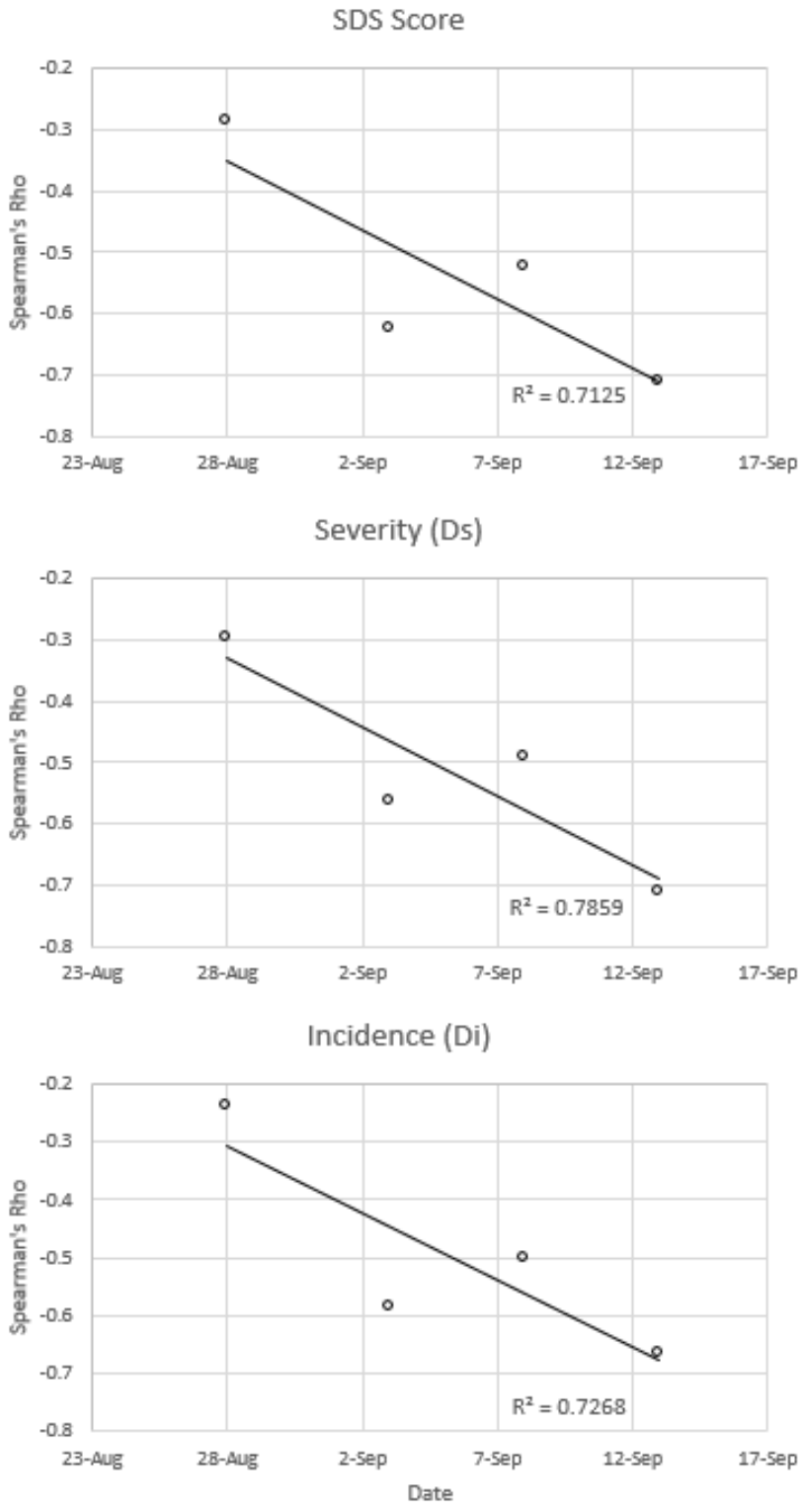

Figure 4.5 - Spearman's Rho related to SDS score, severity of infection, and incidence of infection. R^2 given for SDS score, severity, and incidence.

Discussion

Visual SDS symptoms on 28 August were minimal. A few plots exhibited chlorotic spots, but none exhibited necrotic spots. This day exhibited the least statistical significance for SDS incidence (P = 0.01581). At this point in plant and disease development, the early stages of symptoms are not advanced enough to show strong statistical significance. SDS infection at this point in the season will be minimal only affecting a few plants. Plants showing marginal symptoms might not exhibit distinctly different temperature compared to healthy plants (Figure 4.6). Plots with low SDS infection are distinguished by higher temperature difference. Highly infected plots maintain low Ta-Tc values (Figure 4.6) across the four sUAS flight days. By 13 September, plots with high SDS scores exhibited extreme symptoms with several plots dropping pods and exhibiting prematurely dead leaves. Strong, significant Spearman's rho correlations with temperature difference and SDS score, incidence, and severity (P < 0.0001) appear at this time.

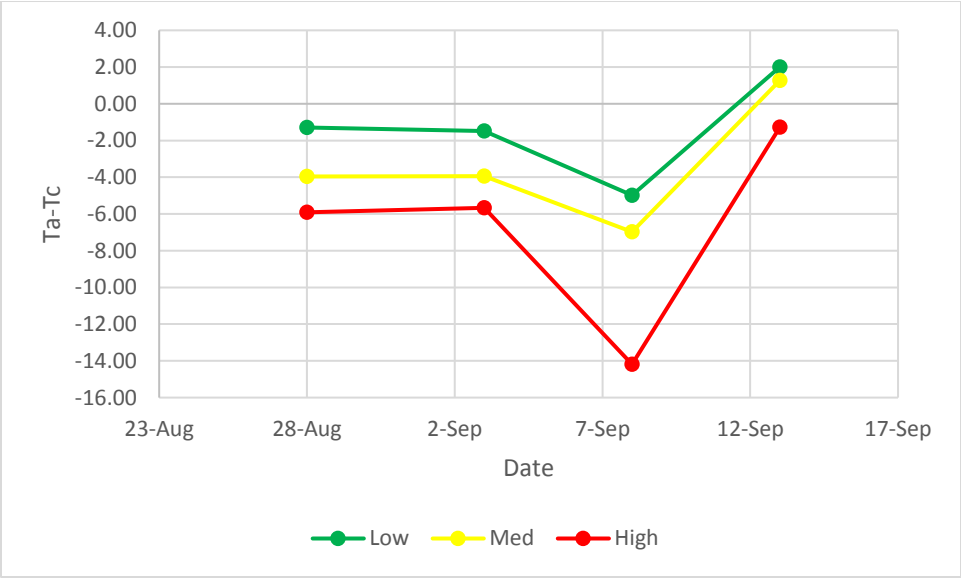

Figure 4.6 - Low, medium, and high plot across four sUAS flight days

An understanding of how field elements and weather affects a crop is critical to precision agriculture. Reasons explaining the observed correlation differences and changes in temperatures would be difficult without a thorough understanding of daily weather measurements. Largescale application of thermal remote sensing should include daily weather measurements and field factors to assess the sensed image accurately. 28 August, 3 September, and 13 September maintain temperature difference values ranging from 6 to -8. 8 September temperature difference values

range from -3 to -14. The low-temperature difference values could be a result of increased canopy temperatures across the entire field.

Several uncharacteristically cool evenings between 4 September and 8 September explain the decrease in correlation on 8 September. Evenings during this time dropped below 50^0F (10^0C). Temperatures this cool, are uncharacteristic for this region and time of year. Cool temperatures help SDS progress and can make symptoms worse. However, at this growth stage, the cool temperature could affect the plant health more than the development and progression of SDS. These cool evening temperatures can cause the plant to slow its metabolic processes. Photosynthesis, homeostasis, and transportation can all slow when cool weather is present. During this time, daily temperatures reached above 80^0F (27^0C). The combination of slowed transpiration and hot daily temperatures causes the plant have elevated canopy temperatures regardless of SDS infection. This can cause the canopy temperatures to rise across the whole field similar to what is seen on 8 September. All plots on 8 September exhibited higher temperatures including the plots unaffected by SDS. Increased canopy temperatures make it more difficult to distinguish between SDS and other factors affecting the plants such as non-disease stress. The overall range of temperatures decreased for 8 September indicated by decreased temperature difference to SDS score correlation. 13 September did not decrease in correlation as night temperatures after 8 September rose, and the soybeans recovered to resume normal metabolic processes.

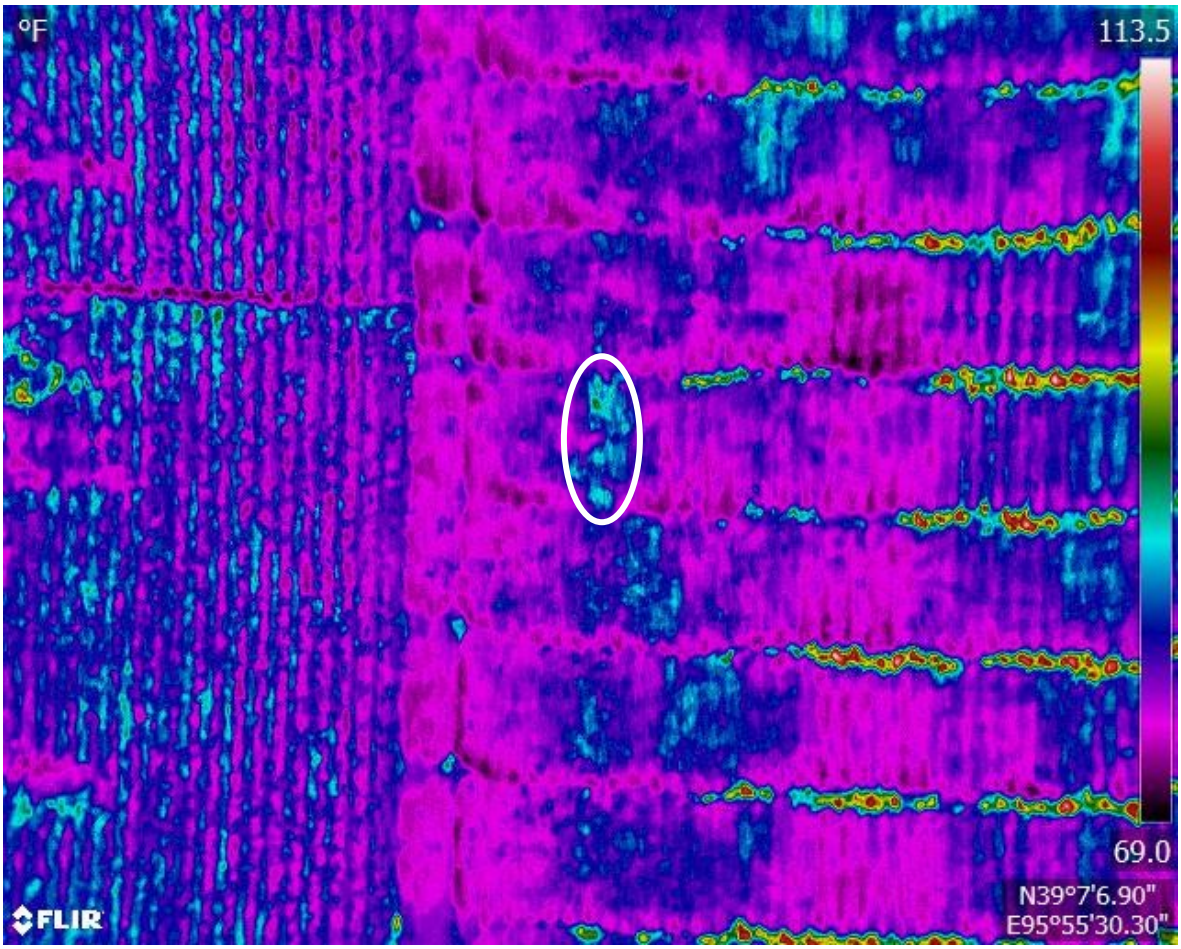

Figure 4.7 - TIR image taken 3 September over the research plot. Temperature in image ranges from 69^0 F (20.5^0 C) to 113.5^0 F (45.3^0 C). Plot 121 (circled) maintains a temperature of 81.1^0 F (27.3^0 C) with an SDS score of 100. Healthy plants exhibit average temperatures below 74^0 F (23.3^0 C)

Figure 4.7 is a TIR image collected during the 3 September flight. Corn boarders the soybean research plots to the left. The center and left of center exhibit the soybean plots flown. Yellow/Red horizontal lines show high temperatures from exposed soil between rows of plots. Soil will range from approximately 80^{0}F (26.7^{0}C) to 113.5^{0}F (45.3^{0}C). The light blue plot (plot 121) in the center of the image (circled, exhibits a temperature of 81.1^{0}F (27.3^{0}C). This soybean plot recorded an SDS score of 100, severity of nine, and incidence of 100%. The plots right of plot 121 record SDS scores of 3.5 or lower, while also maintaining temperatures of approximately 74^{0}F (23.3^{0}C). This image reflects how SDS can dramatically affect the canopy temperature. By keying on the elevated canopy temperatures, these methods can be applied on a large-scale to effectively identify SDS infected soybeans.

Realistically, farmers with large fields cannot assess their entire crop for SDS on a daily or even weekly basis. Farmers would be unable to visually detect SDS in remote areas of the field until symptoms become severe.

Soybeans within a normal grow operation will not be scored for the incidence in a similar manner as they are for research plots. For remote sensing applications presented here to be effective on a large scale, it is critical that the severity and SDS score display similar correlations to temperature difference. Assessment of severity independently, seen in Figure 4.3 and Figure 4.5, express that severity very closely follows the correlation to temperature that SDS score displays. Plots of the Spearman's rho over the four days indicate a stronger relationship (R^2=0.7859) than Spearman's rho for SDS score. This strong relationship indicates that severity is a very good predictor of Spearman's rho for the given day. Figure 4.7 is an example of how farmers can view fields and apply TIR imagery using a sUAS. Farming applications can use TIR imagery for scouting a field for plots exhibiting high canopy temperatures as an indicator of SDS presence within their field.

Conclusion

Previous studies showed that thermal assessment of disease was possible through aerial platforms. The case study presented here demonstrates that an infield assessment and accurate identification of soybean SDS using a TIR camera and sUAS system is possible. Correlations with temperature difference and SDS score increased along with severity throughout the growing season. Correlations with disease incidence and severity also presented increases through the growing season with very strong correlations at the end of the season. Overall assessment of severity displayed the highest relationship in correlation over the days flown. Severity of SDS infection is the most practical predictor of SDS for large application use because of its high correlation and easy application.

This case study exhibits the potential use of TIR remote sensing for detection of SDS in soybean. While correlations at the beginning of the flight period were weak, they have potential to act as predictors to SDS within a field and give preliminary indications of the disease before visual symptoms appear. Future studies will expand this research to assess disease over an entire field and determine when the earliest that definable SDS symptoms are present.

Chapter 5 - Conclusion

Summary of findings

PI derived from a modified broadband camera imagery and change in temperature derived from TIR imagery both show noteworthy improvements to the assessment of SDS in soybean. The use of sUAS for data collection improves upon the current method of ground-based system assessments with the minimization of external variables influencing collected data. The short flight times minimize the change in solar angle, air temperature, wind conditions, and other environmental factors that can influence data.

PI readily detects SDS infection at the growth stage R6. After R6, correlations begin to decrease. Infected and healthy plants begin to senesce as they reach maturity. At maturity, the plants have reached senescence and are no longer photosynthesizing. The drying of the plant in senescence causes confounding variables with SDS. PI does not strictly assess SDS in soybean but, acts as an indicator of plant health. The PI values for plants are low at maturity because the plant is no longer absorbing blue light with the same intensity as healthy plants. Close to plant maturity PI values are influenced by SDS infection as well as senescence. Assessment at R6 gives the most accurate assessment of SDS because plants have not begun to senesce. The only variable interacting with the data is the SDS score. However, PI is also an indicator of maturity. After plants reach R6 PI become a strong indicator of maturity. Use of PI after R6 must consider disease influences as well as senescence.

TIR imagery shows increasing correlations over a growing season. The low correlation of the first flight and low symptom expression could lead to the identification of high instances of SDS in plants that are expressing symptoms early. Early identification of SDS allows for mitigation of the disease before large loses on yield occur. Change in temperature through TIR imagery detected correlations with SDS 10 days before symptom expression climaxed. More studies are needed to further explore how early SDS can be accurately correlated to change in temperature. However, farming operations can act on the knowledge that some crops exhibit higher canopy temperatures than expected. Exploration of the field can occur to detect and/or monitor the crops. If crops are beginning to show symptoms of SDS mitigation steps can be implemented immediately to minimize yield loss. TIR imagery strongly correlates to SDS, as symptom expression gets stronger.

The increase in correlation between SDS score and temperature change across the growing season exhibits soybean's inability to maintain homeostasis once infection occurs.

Through both CIR and TIR imagery the best correlation to PI or change in temperature was not with SDS score but rather severity (a component of SDS score). The strong correlation to severity is encouraging for implementation of these methods to large-scale operations.

Implications

The strong correlations of TIR and PI to disease severity have strong implications in the practical and large-scale application of SDS assessment through aerial imagery. Farmers will not be able to assess the disease incidence in a field covering many acres. While the disease incidence is important for the accurate calculation of SDS score (Dx), it is not practical outside of research and breeding operations. The small plot sizes make it ideal for research and breeding operations. Farming applications will assess the presence of SDS within the field for the mitigation of disease symptoms. Once SDS is discovered mitigation steps are taken for the maximization of yield. Looking only at the disease severity allows for farming operations to readily assess SDS in a given area and take immediate action.

Any time remote sensing is utilized the environmental factors must be considered and understood. This is evident given the changes that were seen in canopy temperatures on 8 September. The cause of the increased canopy temperature could not be determined from the image data alone. Large-scale application of aerial detection of SDS or any remote sensing work will require a knowledge of the area, physical characteristics like soil, and environmental factors such as daily temperature fluctuations. Data misinterpretation can occur when this knowledge is unknown or not considered.

Future work

Future work is required before large-scale application of this methodology is possible. Understanding more about PI and early detection of SDS could help in the mitigation of the disease. Early detection with TIR could be more effective if the range of temperature increase due to SDS infection was better understood. Possible research questions based on this research follow:

- Under controlled conditions (i.e. greenhouse or similar), how early can SDS be accurately detected? Both thermally and with PI.
    - What temperature change can be explained by SDS infection?

    - Is the temperature change limited to a specific range?
    - Can PI be used for accurate early detection of SDS?
- Can PI or CIR imagery be utilized for early assessment of SDS in field conditions?
    - How early can PI and changes in canopy temperature significantly and strongly correlate with SDS?
- Using the TIFF image setting, can you see symptoms of SDS develop over the growing season over a whole field?
    - What change in temperature is significant for detection of SDS infection and not explained by environmental, weather, or field factors?
- Scoring of SDS occurs at R6. However, could the correlations to SDS increase if SDS scoring occurred the same day or day after aerial assessment, even before reaching R6?
    - Is there a stronger correlation throughout the growing season this way?
    - Will the early assessments show stronger correlations or remain the same?
- How do diseases compare with one another? Can we distinguish between different diseases through CIR or TIR imagery?

While these questions will take many more studies to answer, I believe they are important and will lead to better understanding of aerial imagery for disease assessment across many crops.

References

Abdel-Aziz, Y. I., & Karara, H. M. (2015). Direct linear transformation from comparator coordinates into object space coordinates in close-range photogrammetry. *Photogrammetric Engineering and Remote Sensing, 81*(2), 103-107. doi:10.14358/PERS.81.2.103

Al-amri, S., Kalyankar, N. V., & Khamitkar, S. D. (2010). A comparative study of removal noise from remote sensing image.

Ali, A. M., Darvishzadeh, R., Skidmore, A. K., & van Duren, I. (2017). Specific leaf area estimation from leaf and canopy reflectance through optimization and validation of vegetation indices. *Agricultural and Forest Meteorology, 236*, 162-174. doi:10.1016/j.agrformet.2017.01.015

Alonso, C., Tarquis, A. M., Zúñiga, I., & Benito, R. M. (2017). Spatial and radiometric characterization of multi-spectrum satellite images through multi-fractal analysis. *Nonlinear Processes in Geophysics, 24*(2), 141-155. doi:10.5194/npg-24-141-2017

Alves, I., & Pereira, L. S. (2000). Non-water-stressed baselines for irrigation scheduling with infrared thermometers: A new approach. *Irrigation Science, 19*(2), 101-106.

Anderson, J., Akond, M., Kassem, M. A., Meksem, K., & Kantartzi, S. K. (2015). Quantitative trait loci underlying resistance to sudden death syndrome (SDS) in MD96-5722 by 'Spencer' recombinant inbred line population of soybean. *3 Biotech, 5*(2), 203-210. doi:10.1007/s13205-014-0211-3

Ayeneh, A., van Ginkel, M., Reynolds, M. P., & Ammar, K. (2002). Comparison of leaf, spike, peduncle and canopy temperature depression in wheat under heat stress. *Field Crops Research, 79*(2), 173-184. doi:10.1016/S0378-4290(02)00138-7

Bajwa, S. G., Rupe, J. C., & Mason, J. (2017). Soybean disease monitoring with leaf reflectance. *Remote Sensing, 9*(2) doi:10.3390/rs9020127

Baret, F., & Guyot, G. (1991). Potentials and limits of vegetation indices for LAI and APAR assessment. *Remote Sensing of Environment, 35*(2-3), 161-173. doi:10.1016/0034-4257(91)90009-U

Baret, F., Guyot, G., & Major, D. J. (1989). *TSAVI: A vegetation index which minimizes soil brightness effects on LAI and APAR estimation*

Barnes, E. M., Clarke, T. R., Richards, S. E., Colaizzi, P. D., Haberland, J., Kostrzewski, M., . . . Moran, M. S. (2000). *Coincident detection of crop water stress, nitrogen status and canopy density using ground-based multispectral data*. Madison: American Society of Agronomy.

Bendig, J., Bolten, A., Bennertz, S., Broscheit, J., Eichfuss, S., & Bareth, G. (2014). Estimating biomass of barley using crop surface models (CSMs) derived from UAV-based RGB imaging. *Remote Sensing, 6*(11), 10395-10412. doi:10.3390/rs61110395

Berdugo, C. A., Zito, R., Paulus, S., & Mahlein, A. -. (2014). Fusion of sensor data for the detection and differentiation of plant diseases in cucumber. *Plant Pathology, 63*(6), 1344-1356. doi:10.1111/ppa.12219

Berni, J. A. J., Zarco-Tejada, P., Sepulcre-Cantó, G., Fereres, E., & Villalobos, F. (2009). Mapping canopy conductance and CWSI in olive orchards using high resolution thermal remote sensing imagery. *Remote Sensing of Environment, 113*(11), 2380-2388. doi:10.1016/j.rse.2009.06.018

Berni, J. A. J., Zarco-Tejada, P., Suarez, L., & Fereres, E. (2009). Thermal and narrowband multispectral remote sensing for vegetation monitoring from an unmanned aerial vehicle.(author abstract)(technical report). *IEEE Transactions on Geoscience and Remote Sensing, 47*(3), 722. doi:10.1109/TGRS.2008.2010457

Blackburn, G. A. (1998). Spectral indices for estimating photosynthetic pigment concentrations: A test using senescent tree leaves. *International Journal of Remote Sensing, 19*(4), 657-675. doi:10.1080/014311698215919

Borgogno-Mondino, E., Lessio, A., Tarricone, L., Novello, V., & de Palma, L. (2018). A comparison between multispectral aerial and satellite imagery in precision viticulture. *Precision Agriculture, 19*(2), 195-217. doi:10.1007/s11119-017-9510-0

Broge, N. H., & Leblanc, E. (2001). Comparing prediction power and stability of broadband and hyperspectral vegetation indices for estimation of green leaf area index and canopy chlorophyll density. *Remote Sensing of Environment, 76*(2), 156-172. doi:10.1016/S0034-4257(00)00197-8

Brown, L., Chen, J. M., Leblanc, S. G., & Cihlar, J. (2000). A shortwave infrared modification to the simple ratio for LAI retrieval in boreal forests: An image and model analysis. *Remote Sensing of Environment, 71*(1), 16-25. doi:10.1016/S0034-4257(99)00035-8

Bybordi, S., & Reggiani, L. (2015). (2015). Drones in agriculture: Applications and outlook. Paper presented at the *Dipartimento Di Elettroniva Informazione e Bioingegneria,*

Calderón, R., Navas-Cortés, J. A., Lucena, C., & Zarco-Tejada, P. (2013). High- resolution airborne hyperspectral and thermal imagery for early detection of verticillium wilt of olive using fluorescence, temperature and narrow- band spectral indices. *Remote Sensing of Environment, 139*, 231-245. doi:10.1016/j.rse.2013.07.031

Calderón, R., Montes-Borrego, M., Landa, B., Navas-Cortés, J., & Zarco-Tejada, P. (2014a). Detection of downy mildew of opium poppy using high- resolution multi-spectral and thermal imagery acquired with an unmanned aerial vehicle. *Precision Agriculture, 15*(6), 639-661. doi:10.1007/s11119-014-9360-y

Calderón, R., Montes-Borrego, M., Landa, B. B., Navas-Cortés, J. A., & Zarco-Tejada, P. J. (2014b). Detection of downy mildew of opium poppy using high-resolution multi-spectral and thermal imagery acquired with an unmanned aerial vehicle. *Precision Agriculture, 15*(6), 639-661. doi:10.1007/s11119-014-9360-y

Campomanes, F. P., V., Silapan, J. R., & Blanco, A. C. (2015). Building footprint extraction using LiDAR data and spectral indices from aerial imagery. Paper presented at the *ACRS 2015 - 36th Asian Conference on Remote Sensing: Fostering Resilient Growth in Asia, Proceedings,*

Carbonnell, M., Karara, H. M., & American Society, o. P. (1979). *Handbook of non-topographic photogrammetry* Falls Church, Va.: American Society of Photogrammetry.

Ceccato, P., Flasse, S., & Grégoire, J. (2002). Designing a spectral index to estimate vegetation water content from remote sensing data: Part 2. validation and applications. *Remote Sensing of Environment, 82*(2), 198-207. doi:10.1016/S0034-4257(02)00036-6

Chaerle, L., Hagenbeek, D., De Bruyne, E., Valcke, R., & Van, D. S. (2004). Thermal and chlorophyll- fluorescence imaging distinguish plant-pathogen interactions at an early stage. *Plant and Cell Physiology, 45*(7), 887-896. doi:10.1093/pcp/pch097

Chappelle, E. W., Kim, M. S., & Mcmurtrey, J. E. (1992). Ratio analysis of reflectance spectra (RARS): An algorithm for the remote estimation of the concentrations of chlorophyll A, chlorophyll B, and carotenoids in soybean leaves. *Remote Sensing of Environment, 39*(3), 239-247. doi:10.1016/0034-4257(92)90089-3

Chavez, P. S. (1996). Image-based atmospheric corrections revisited and improved. *Photogrammetric Engineering and Remote Sensing; Photogramm.Eng.Remote Sens., 62*(9), 1025-1036.

Chen, J. M. (1996). Evaluation of vegetation indices and a modified simple ratio for boreal applications. *Canadian Journal of Remote Sensing, 22*(3), 229-242. doi:10.1080/07038992.1996.10855178

Chong, S. -., Hildebrand, K. K., Luo, Y., Myers, O., Indorante, S. J., Kazakevicius, A., & Russin, J. (2005). Mapping soybean sudden death syndrome as related to yield and soil/site properties. *Soil and Tillage Research, 84*(1), 101-107. doi:10.1016/j.still.2004.09.001

Clevers, J. G. P. W. (1991). Application of the WDVI in estimating LAI at the generative stage of barley. *ISPRS Journal of Photogrammetry and Remote Sensing, 46*(1), 37-47. doi:10.1016/0924-2716(91)90005-G

Clevers, J. G. P. W., & Verhoef, W. (1993). LAI estimation by means of the WDVI: A sensitivity analysis with combined PROSPECT-SAIL model. *Remote Sensing Reviews, 7*(1), 43-64.

Collings, S., & Caccetta, P. (2011). On the generation of broad-scale hyperspectral ground reflectance mosaics from aerial and ground-based observations. *International Journal of Image and Data Fusion, 2*(3), 237-253. doi:10.1080/19479832.2010.551523

Cui, D., Zhang, Q., Li, M., Slaminko, T., & Hartman, G. L. (2014). A method for determining the severity of sudden death syndrome in soybeans. *Transactions of the ASABE, 57*(2), 671-678. doi:10.13031/trans.57.9837

d'Oleire-Oltmanns, S., Marzolff, I., Peter, K. D., Ries, J. B., & Hssaïne, A. A. (2011). (2011). Monitoring soil erosion in the souss basin, Morocco, with a multiscale object-based remote sensing approach using UAV and satellite data. Paper presented at the *1st World Sustainability Forum,* Basel, Switzerland.

Dash, J., & Curran, P. J. (2004). The MERIS terrestrial chlorophyll index. *International Journal of Remote Sensing, 25*(23), 5403-5413. doi:10.1080/0143116042000274015

Datt, B. (1999). Remote sensing of water content in eucalyptus leaves. *Australian Journal of Botany, 47*(6), 909-923. doi:10.1071/BT98042

Daughtry, C. S. T., Hunt Jr., E. R., Doraiswamy, P. C., & McMurtrey III, J. E. (2005). Remote sensing the spatial distribution of crop residues. *Agronomy Journal, 97*(3), 864-871. doi:10.2134/agronj2003.0291

Daughtry, C. S. T., Walthall, C. L., Kim, M. S., de Colstoun, E. B., & Mcmurtrey, J. E. (2000). Estimating corn leaf chlorophyll concentration from leaf and canopy reflectance. *Remote Sensing of Environment, 74*(2), 229-239. doi:10.1016/S0034-4257(00)00113-9

De Carolis, C., Baldi, G., Galli de Paratesi, S., & Lechi, G. M. (1974). Thermal behaviour of some rice fields affected by a yellows-type disease.*2*, 1161-1170.

De Villiers, J. P., Leuschner, F. W., & Geldenhuys, R. (2010). Modeling of radial asymmetry in lens distortion facilitated by modern optimization techniques. Paper presented at the *Proceedings of SPIE - the International Society for Optical Engineering, , 7539* doi:10.1117/12.838804

Deering, D. W., Rouse Jr., J. W., Haas, R. H., & Schell, J. A. (1975). Measuring "forage production" of grazing units from Landsat MSS data.*2*, 1169-1178.

Del Pozo, S., Rodríguez-Gonzálvez, P., Hernández-López, D., & Felipe-García, B. (2014). Vicarious radiometric calibration of a multispectral camera on board an unmanned aerial system. *Remote Sensing, 6*(3), 1918-1937. doi:10.3390/rs6031918

Dinguirard, M., & Slater, P. N. (1999). Calibration of space- multispectral imaging sensors: A review. *Remote Sensing of Environment, 68*(3), 194-205. doi:10.1016/S0034-4257(98)00111-4

Eitel, J. U. H., Long, D. S., Gessler, P. E., & Smith, A. M. S. (2007). Using in-situ measurements to evaluate the new RapidEye ™ satellite series for prediction of wheat nitrogen status. *International Journal of Remote Sensing, 28*(18), 4183-4190. doi:10.1080/01431160701422213

Espinoza, C. Z., Khot, L. R., Sankaran, S., & Jacoby, P. W. (2017). High resolution multispectral and thermal remote sensing-based water stress assessment in subsurface irrigated grapevines. *Remote Sensing, 9*(9) doi:10.3390/rs9090961

Faig, W. (1975). Calibration of close-range photogrammetric systems: Mathematical formulation. *Photogrammetric Engineering and Remote Sensing, 41*(12), 1479-1486.

Fehr, W. R., Caviness, C. F., Burmood, D. T., & Pennington, J. S. (1971). Stage of development descriptions for soybeans, glycine max (L.) merrill. *Crop Sci, 11*, 929-931.

Feng, Q., Liu, J., & Gong, J. (2015). UAV remote sensing for urban vegetation mapping using random forest and texture analysis. *Remote Sensing, 7*(1), 1074-1094. doi:10.3390/rs70101074

Flynn, K. F., & Chapra, S. C. (2014). Remote sensing of submerged aquatic vegetation in a shallow non- turbid river using an unmanned aerial vehicle. *RemoteSensing, 6*(12), 12815-12836. doi:10.3390/rs61212815

Fuentes, D., & G. (2001). Mapping Canadian boreal forest vegetation using pigment and water absorption features derived from the AVIRIS sensor. *Journal of Geophysical Research: Atmospheres, 106*, 33565-33577. doi:10.1029/2001JD900110

Gamon, J. A., Peñuelas, J., & Field, C. B. (1992). A narrow-waveband spectral index that tracks diurnal changes in photosynthetic efficiency. *Remote Sensing of Environment, 41*(1), 35-44. doi:10.1016/0034-4257(92)90059-S

GAMON, J. A., & SURFUS, J. S. (1999). Assessing leaf pigment content and activity with a reflectometer. *New Phytologist; New Phytologist, 143*(1), 105-117. doi:10.1046/j.1469-8137.1999.00424.x

Garcia-Ruiz, F., Sankaran, S., Maja, J. M., Lee, W. S., Rasmussen, J., & Ehsani, R. (2013). Comparison of two aerial imaging platforms for identification of Huanglongbing-infected citrus trees. *Computers and Electronics in Agriculture, 91*, 106-115. doi:https://doi.org/10.1016/j.compag.2012.12.002

Gausman, H. W. (1977). Reflectance of leaf components. *Remote Sensing of Environment, 6*(1), 1-9. doi:10.1016/0034-4257(77)90015-3

Gausman, H. W. (1974). Leaf reflectance of near-infrared. *Photogramm Eng, 40*(2), 183-191.

Getzin, S., Nuske, R. S., & Wiegand, K. (2014). Using unmanned aerial vehicles (UAV) to quantify spatial gap patterns in forests. *Remote Sensing, 6*(8), 6988-7004. doi:10.3390/rs6086988

Gilabert, M. A., González-Piqueras, J., García-Haro, F. J., & Meliá, J. (2002). A generalized soil- adjusted vegetation index. *Remote Sensing of Environment, 82*(2), 303-310. doi:10.1016/S0034-4257(02)00048-2

Gitelson, A. A., Kaufman, Y. J., & Merzlyak, M. N. (1996). Use of a green channel in remote sensing of global vegetation from EOS- MODIS. *Remote Sensing of Environment, 58*(3), 289-298. doi:10.1016/S0034-4257(96)00072-7

Gitelson, A. A., & Merzlyak, M. N. (1998). Remote sensing of chlorophyll concentration in higher plant leaves. *Advances in Space Research, 22*(5), 689-692. doi:10.1016/S0273-1177(97)01133-2

Gitelson, A. A., Merzlyak, M. N., & Chivkunova, O. B. (2001). Optical properties and nondestructive estimation of anthocyanin content in plant leaves. *Photochemistry and Photobiology, 74*(1), 38-45. doi:10.1562/0031-8655(2001)074<0038:OPANEO>2.0.CO;2

Gitelson, A. A., Zur, Y., Chivkunova, O. B., & Merzlyak, M. N. (2002). Assessing carotenoid content in plant leaves with reflectance spectroscopy. *Photochemistry and Photobiology, 75*(3), 272-281. doi:10.1562/0031-8655(2002)075<0272:ACCIPL>2.0.CO;2

Gitelson, A. A. (2004). Wide dynamic range vegetation index for remote quantification of biophysical characteristics of vegetation. *Journal of Plant Physiology, 161*(2), 165-173. doi:10.1078/0176-1617-01176

Gitelson, A. A., Gritz †, Y., & Merzlyak, M. N. (2003). Relationships between leaf chlorophyll content and spectral reflectance and algorithms for non- destructive chlorophyll assessment in higher plant leaves. *Journal of Plant Physiology, 160*(3), 271-282. doi:10.1078/0176-1617-00887

Gitelson, A. A., Kaufman, Y. J., & Merzlyak, M. N. (1996). Use of a green channel in remote sensing of global vegetation from EOS- MODIS. *Remote Sensing of Environment, 58*(3), 289-298. doi:10.1016/S0034-4257(96)00072-7

Gitelson, A. A., Kaufman, Y. J., Stark, R., & Rundquist, D. (2002). Novel algorithms for remote estimation of vegetation fraction. *Remote Sensing of Environment, 80*(1), 76-87. doi:10.1016/S0034-4257(01)00289-9

Gitelson, A. A., & Merzlyak, M. N. (1998). Remote sensing of chlorophyll concentration in higher plant leaves. *Advances in Space Research, 22*(5), 689-692. doi:10.1016/S0273-1177(97)01133-2

Gitelson, A. A., Viña, A., Ciganda, V., Rundquist, D. C., & Arkebauer, T. J. (2005). Remote estimation of canopy chlorophyll content in crops. *Geophysical Research Letters, 32*(8), n/a-n/a. doi:10.1029/2005GL022688

Gitelson, A., & Merzlyak, M. N. (1994). Quantitative estimation of chlorophyll- a using reflectance spectra: Experiments with autumn chestnut and maple leaves. *Journal of Photochemistry & Photobiology, B: Biology, 22*(3), 247-252. doi:10.1016/1011-1344(93)06963-4

Goel, N. S., & Qin, W. (1994). Influences of canopy architecture on relationships between various vegetation indices and LAI and fpar: A computer simulation. *Remote Sensing Reviews, 10*(4), 309-347. doi:10.1080/02757259409532252

Gómez-Candón, D., De Castro, A., & López-Granados, F. (2014). Assessing the accuracy of mosaics from unmanned aerial vehicle (UAV) imagery for precision agriculture purposes in wheat. *Precision Agriculture, 15*(1), 44-56. doi:10.1007/s11119-013-9335-4

Gong, P., Pu, R., Biging, G. S., & Larrieu, M. R. (2003). Estimation of forest leaf area index using vegetation indices derived from hyperion hyperspectral data. *Geoscience and Remote Sensing, IEEE Transactions on, 41*(6), 1355-1362. doi:10.1109/TGRS.2003.812910

Granados-Ramírez, R., Reyna-Trujillo, T., Gómez-Rodríguez, G., & Soria-Ruiz, J. (2004). Analysis of NOAA-AVHRR-NDVI images for crops monitoring. *International Journal of Remote Sensing, 25*(9), 1615-1627. doi:10.1080/0143116031000156855

Guan, K., Wu, J., Kimball, J. S., Anderson, M. C., Frolking, S., Li, B., . . . Lobell, D. B. (2017). The shared and unique values of optical, fluorescence, thermal and microwave satellite data for estimating large-scale crop yields. *Remote Sensing of Environment, 199*, 333-349. doi:10.1016/j.rse.2017.06.043

Gunawardena, A., & Fernando, T. (2016). Use of optical, thermal IR and radar satellite data to estimate above ground biomass in montane forests of Sri Lanka. Paper presented at the *37th Asian Conference on Remote Sensing, ACRS 2016, 2* 945-951.

Guoquan, D., & Zhengzhi, L. (1993). The apparent emissivity of vegetation canopies. *International Journal of Remote Sensing, 14*(1), 183-188. doi:10.1080/01431169308904329

Haboudane, D., Miller, J. R., Pattey, E., Zarco-Tejada, P. J., & Strachan, I. B. (2004). Hyperspectral vegetation indices and novel algorithms for predicting green LAI of crop canopies: Modeling and validation in the context of precision agriculture. *Remote Sensing of Environment, 90*(3), 337-352. doi:10.1016/j.rse.2003.12.013

Haboudane, D., Miller, J. R., Tremblay, N., Zarco-Tejada, P. J., & Dextraze, L. (2002). Integrated narrow-band vegetation indices for prediction of crop chlorophyll content for application to precision agriculture. *Remote Sensing of Environment, 81*(2-3), 416-426. doi:10.1016/S0034-4257(02)00018-4

Haboudane, D., Tremblay, N., Miller, J. R., & Vigneault, P. (2008). Remote estimation of crop chlorophyll content using spectral indices derived from hyperspectral data. *Geoscience and Remote Sensing, IEEE Transactions on, 46*(2), 423-437. doi:10.1109/TGRS.2007.904836

Hartman, G. L., Sinclair, J. B., & Rupe, J. C. (1999). Sudden death syndrome. *Compendium of soybean diseases* (Fourth ed., pp. 37-38). St. Paul, Minnesota: APS Press.

Hecker, C. A., Smith, T. E. L., Luz, R. D., & Wooster, M. J. (2013). *Thermal infrared spectroscopy in the laboratory and field in support of land surface remote sensing* doi:10.1007/978-94-007-6639-6_3

Heikkila, J., & Silven, O. (1997). *A four-step camera calibration procedure with implicit image correction* doi:10.1109/CVPR.1997.609468

Heliospectra. (2014). LED light spectrum 101: Absorption spectra. Retrieved from https://www.heliospectra.com/articles/led-light-spectrum-101-absorption-spectra/

Hodecker, B. E. R., Pita-Barbosa, A., de Barros, N. F., & Merchant, A. (2018). Water availability preceding long-term drought defines the tolerance of eucalyptus to water restriction. *New Forests, 49*(2), 173-195. doi:10.1007/s11056-017-9612-6

Huang, Y., Lan, Y., Ge, Y., Hoffmann, W. C., & Thomson, S. J. (2010a). Spatial modeling and variability analysis for modeling and prediction of soil and crop canopy coverage using multispectral imagery from an airborne remote sensing system. *Transactions of the ASABE, 53*(4), 1321-1329.

Huang, Y., Lan, Y., Ge, Y., Hoffmann, W. C., & Thomson, S. J. (2010b). Spatial modeling and variability analysis for modeling and prediction of soil and crop canopy coverage using multispectral imagery from an airborne remote sensing system. *Transactions of the ASABE, 53*(4), 1321-1329. doi:10.13031/2013.32582

Huete, A., Didan, K., Miura, T., Rodriguez, E. P., Gao, X., & Ferreira, L. G. (2002). Overview of the radiometric and biophysical performance of the MODIS vegetation indices. *Remote Sensing of Environment, 83*(1), 195-213. doi:10.1016/S0034-4257(02)00096-2

Huete, A. R. (1988). A soil-adjusted vegetation index (SAVI). *Remote Sensing of Environment, 25*(3), 295-309. doi:10.1016/0034-4257(88)90106-X

Huete, A. R., Liu, H. Q., Batchily, K., & van Leeuwen, W. (1997). A comparison of vegetation indices over a global set of TM images for EOS-MODIS. *Remote Sensing of Environment, 59*(3), 440-451. doi:10.1016/S0034-4257(96)00112-5

Hunt Jr., E. R., Doraiswamy, P. C., McMurtrey, J. E., Daughtry, C. S. T., Perry, E. M., & Akhmedov, B. (2013). A visible band index for remote sensing leaf chlorophyll content at the canopy scale. *International Journal of Applied Earth Observation and Geoinformation, 21*, 103-112. doi:https://doi.org/10.1016/j.jag.2012.07.020

Hunt, R. E., Daughtry, C. S. T., Eitel, J. U. H., & Long, D. S. (2011). Remote sensing leaf chlorophyll content using a visible band index. *Agronomy Journal, 103*(4), 1090-1099. doi:10.2134/agronj2010.0395

Idso, S., Jackson, R., Pinter, P., Reginato, R., & Hatfield, J. (1981). Normalizing the stress-degree- day parameter for environmental variability. *AGRIC.METEOROL, 24*(1), 45-55.

Izaguirre, A., Pu, P., & Summers, J. (1987). New development in camera calibration: Calibrating a pair of mobile cameras. *International Journal of Robotics Research, 6*(3), 104-116.

Jones, H. G., Serraj, R., Loveys, B. R., Xiong, L., Wheaton, A., & Price, A. H. (2009). Thermal infrared imaging of crop canopies for the remote diagnosis and quantification of plant responses to water stress in the field. *Functional Plant Biology, 36*(11), 978-989. doi:10.1071/FP09123

Jordan, C. F. (1969). Derivation of leaf- area index from quality of light on the forest floor. *Ecology, 50*(4), 663-666. doi:10.2307/1936256

Kaleita, A. L. (2006). *Fusion of remotely sensed imagery and minimal ground sampling for soil moisture mapping* Digital Repository @ Iowa State University.

Kang, L., Ji, C. Y., Kim, S. H., Ke, Q., Park, S. -., Kim, H. S., . . . Kwak, S. -. (2017). Suppression of the ß-carotene hydroxylase gene increases ß-carotene content and tolerance to abiotic stress in transgenic sweetpotato plants. *Plant Physiology and Biochemistry, 117*, 24-33. doi:10.1016/j.plaphy.2017.05.017

Kaufman, Y. J., & Tanré, D. (1992). Atmospherically resistant vegetation index (ARVI) for EOS-MODIS. *IEEE Transactions on Geoscience and Remote Sensing, 30*(2), 261-270. doi:10.1109/36.134076

Kelcey, J., & Lucieer, A. (2012a). Sensor correction of a 6-band multispectral imaging sensor for UAV remote sensing. *Remote Sensing, 4*(5), 1462-1493. doi:10.3390/rs4051462

Kelcey, J., & Lucieer, A. (2012b). Sensor correction and radiometric calibration of a 6- band multispectral imaging sensor for UAV remote sensing. *International Archives of the Photogrammetry, Remote Sensing and Spatial Information Sciences - ISPRS Archives, 39*, 393-398.

Kim, M. S., Daughtry, C. S. T., Chappelle, E. W., Mcmurtrey, J. E., & Walthall, C. L. (1994). (1994). The use of high spectral resolution bands for estimating absorbed photosynthetically active radiation (APAR. Paper presented at the *CNES, Proceedings of 6th International Symposium on Physical Measurements and Signatures in Remote Sensing,*

Kim, S. H., Ahn, Y. O., Ahn, M., Lee, H., & Kwak, S. (2012). Down-regulation of β- carotene hydroxylase increases β- carotene and total carotenoids enhancing salt stress tolerance in transgenic cultured cells of sweetpotato. *Phytochemistry, 74*, 69-78. doi:10.1016/j.phytochem.2011.11.003

Lamchin, M., Lee, W. -., Jeon, S. W., Wang, S. W., Lim, C. H., Song, C., & Sung, M. (2018). Long-term trend and correlation between vegetation greenness and climate variables in asia based on satellite data. *Science of the Total Environment, 618*, 1089-1095. doi:10.1016/j.scitotenv.2017.09.145

Le Maire, G., François, C., Soudani, K., Berveiller, D., Pontailler, J., Bréda, N., . . . Dufrêne, E. (2008). Calibration and validation of hyperspectral indices for the estimation of broadleaved forest leaf chlorophyll content, leaf mass per area, leaf area index and leaf canopy biomass. *Remote Sensing of Environment, 112*(10), 3846-3864. doi:10.1016/j.rse.2008.06.005

Leroux, L., Baron, C., Zoungrana, B., Traore, S. B., Lo Seen, D., & Begue, A. (2016). Crop monitoring using vegetation and thermal indices for yield estimates: Case study of a rainfed cereal in semi-arid west Africa. *IEEE Journal of Selected Topics in Applied Earth Observations and Remote Sensing, 9*(1), 347-362. doi:10.1109/JSTARS.2015.2501343

Link, J., Senner, D., & Claupein, W. (2013). Developing and evaluating an aerial sensor platform (ASP) to collect multispectral data for deriving management decisions in precision farming. *Computers and Electronics in Agriculture, 94*, 20-28. doi:https://doi.org/10.1016/j.compag.2013.03.003

Liu, F., Qin, Q., & Zhan, Z. (2012). A novel dynamic stretching solution to eliminate saturation effect in NDVI and its application in drought monitoring. *Chinese Geographical Science, 22*(6), 683-694. doi:10.1007/s11769-012-0574-5

Liu, H. Q., & Huete, A. (1995). Feedback based modification of the NDVI to minimize canopy background and atmospheric noise. *IEEE Transactions on Geoscience and Remote Sensing, 33*(2), 457-465. doi:10.1109/36.377946

Louhaichi, M., Borman, M. M., & Johnson, D. E. (2001). Spatially located platform and aerial photography for documentation of grazing impacts on wheat. *Geocarto International, 16*(1), 65-70. doi:10.1080/10106040108542184

Lück-Vogel, M., Mbolambi, C., Rautenbach, K., Adams, J., & van Niekerk, L. (2016). Vegetation mapping in the st lucia estuary using very high-resolution multispectral imagery and LiDAR. *South African Journal of Botany, 107*, 188-199. doi:http://dx.doi.org/10.1016/j.sajb.2016.04.010

Lukas, V., Novák, J., Neudert, L., Svobodova, I., Rodriguez-Moreno, F., Edrees, M., & Kren, J. (2016). The combination of UAV survey and landsat imagery for monitoring of crop vigor in precision agriculture. Paper presented at the *International Archives of the Photogrammetry, Remote Sensing and Spatial Information Sciences - ISPRS Archives, 41* 953-957. doi:10.5194/isprsarchives-XLI-B8-953-2016

Luo, D., Jin, H., Marchenko, S. S., & Romanovsky, V. E. (2018). Difference between near-surface air, land surface and ground surface temperatures and their influences on the frozen ground on the qinghai-tibet plateau. *Geoderma, 312*, 74-85. doi:10.1016/j.geoderma.2017.09.037

Lymburner, L., Beggs, P. J., & Jacobson, C. R. (2000). Estimation of canopy-average surface-specific leaf area using landsat TM data. *Photogrammetric Engineering and Remote Sensing, 66*(2), 183-191.

Mahlein, A. -., Rumpf, T., Welke, P., Dehne, H. -., Plümer, L., Steiner, U., & Oerke, E. -. (2013). Development of spectral indices for detecting and identifying plant diseases. *Remote Sensing of Environment, 128*, 21-30. doi:10.1016/j.rse.2012.09.019

Mahlein, A., Oerke, E., Steiner, U., & Dehne, H. (2012). Recent advances in sensing plant diseases for precision crop protection. *European Journal of Plant Pathology; Published in Cooperation with the European Foundation for Plant Pathology, 133*(1), 197-209. doi:10.1007/s10658-011-9878-z

Maimaitijiang, M., Ghulam, A., Sidike, P., Hartling, S., Maimaitiyiming, M., Peterson, K., . . . Fritschi, F. (2017). Unmanned aerial system (UAS)-based phenotyping of soybean using

multi-sensor data fusion and extreme learning machine. *ISPRS Journal of Photogrammetry and Remote Sensing, 134*, 43-58. doi:10.1016/j.isprsjprs.2017.10.011

Major, D. J., Baret, F., & Guyot, G. (1990). A ratio vegetation index adjusted for soil brightness. *International Journal of Remote Sensing, 11*(5), 727-740. doi:10.1080/01431169008955053

Manage soybean risks, SDS and SCN with ILeVO. (2016). Retrieved from http://www.crossroadstoday.com/story/34649679/manage-soybean-risks-sds-and-scn-with-ilevo

Mansouri, A., Marzani, F. S., & Gouton, P. (2005a). Development of a protocol for CCD calibration: Application to a multispectral imaging system. *International Journal of Robotics and Automation, 20*(2), 94-100.

Mansouri, A., Marzani, F. S., & Gouton, P. (2005b). Development of a protocol for CCD calibration: Application to a multispectral imaging system. *International Journal of Robotics and Automation, 20*(2), 94-100.

Martins, H. A., Birk, J. R., & Kelley, R. B. (1981). Camera models based on data from two calibration planes. *Computer Graphics and Image Processing, 17*(2), 173-180. doi:10.1016/0146-664X(81)90024-1

Matese, A., Toscano, P., Di Gennaro, S. F., Genesio, L., Vaccari, F. P., Primicerio, J., . . . Gioli, B. (2015). Intercomparison of UAV, aircraft and satellite remote sensing platforms for precision viticulture. *Remote Sensing, 7*(3), 2971-2990. doi:10.3390/rs70302971

McGwire, K. C., Weltz, M. A., Finzel, J. A., Morris, C. E., Fenstermaker, L. F., & McGraw, D. S. (2013). Multiscale assessment of green leaf cover in a semi-arid rangeland with a small unmanned aerial vehicle. *International Journal of Remote Sensing, 34*(5), 1615-1632. doi:10.1080/01431161.2012.723836

Mitchell, J. J., Glenn, N. F., Anderson, M. O., Hruska, R. C., Halford, A., Baun, C., & Nydegger, N. (2012). Unmanned aerial vehicle (UAV) hyperspectral remote sensing for dryland vegetation monitoring. Paper presented at the *2012 4th Workshop on Hyperspectral Image and Signal Processing, WHISPERS 2012, June 4, 2012 - June 7,* ASD; et al.; EXELI S; Golden Way Scientific; HySpex; Itres. doi:10.1109/WHISPERS.2012.6874315 Retrieved from http://dx.doi.org/10.1109/WHISPERS.2012.6874315

Moran, M. S., Jackson, R. D., Slater, P. N., & Teillet, P. M. (1992). Evaluation of simplified procedures for retrieval of land surface reflectance factors from satellite sensor output. *Remote Sensing of Environment, 41*(2-3), 169-184. doi:10.1016/0034-4257(92)90076-V

Nagler, P. L., Daughtry, C. S. T., & Goward, S. N. (2000). Plant litter and soil reflectance. *Remote Sensing of Environment, 71*(2), 207-215. doi:10.1016/S0034-4257(99)00082-6

Naidu, R. A., Perry, E. M., Pierce, F. J., & Mekuria, T. (2009). The potential of spectral reflectance technique for the detection of grapevine leafroll-associated virus-3 in two red-

berried wine grape cultivars. *Computers and Electronics in Agriculture, 66*(1), 38-45. doi:10.1016/j.compag.2008.11.007

Nemani, R., Pierce, L., Running, S., & Band, L. (1993). Forest ecosystem processes at the watershed scale: Sensitivity to remotely- sensed leaf area index estimates. *International Journal of Remote Sensing, 14*(13), 2519-2534. doi:10.1080/01431169308904290

Ngaki, M. N., Wang, B., Sahu, B. B., Srivastava, S. K., Farooqi, M. S., Kambakam, S., . . . Bhattacharyya, M. K. (2016). Tanscriptomic study of the soybean-fusarium virguliforme interaction revealed a novel ankyrin-repeat containing defense gene, expression of whose during infection led to enhanced resistance to the fungal pathogen in transgenic soybean plants. *PLoS ONE, 11*(10) doi:10.1371/journal.pone.0163106

Nijti, V., Johnson, J., Torto, T., Gray, L., & Lightfoot, D. (2001). Inoculum rate influences selection for field resistance to soybean sudden death syndrome in the greenhouse. *Crop Science, 41*(6), 1726-1731. doi:10.2135/cropsci2001.1726

Oerke, E. C., Steiner, U., Dehne, H., & Lindenthal, M. (2006). Thermal imaging of cucumber leaves affected by downy mildew and environmental conditions. *Journal of Experimental Botany; J.Exp.Bot., 57*(9), 2121-2132. doi:10.1093/jxb/erj170

Pearson, R. L., & Miller, L. D. (1972). (1972). Remote mapping of standing crop biomass for estimation of the productivity of the shortgrass prairie. Paper presented at the *Eighth Int. Symp. on Remote Sensing of Environment,* Ann Arbor, MI. 1357-1381.

Penuelas, J., Baret, F., & Filella, I. (1995). Semi-empirical indices to assess carotenoids/chlorophyll a ratio from leaf spectral reflectance. *Photosynthetica, 31*(2), 221-230.

Phatak, A. (2004). A user-friendly guide to multivariate calibration and classificationtion, T. næs, T. isaksson, T. fearn, T. davies: Chichester: NIR publications. *Chemometrics and Intelligent Laboratory Systems, 71*(1), 79-81. doi:http://dx.doi.org/10.1016/j.chemolab.2003.12.010

Pinter, P., Hatfield, J., Schepers, J., Barnes, E., Moran, M. S., Daughtry, C., & Upchurch, D. (2003). Remote sensing for crop management. *Photogrammetric Engineering and Remote Sensing; Photogramm.Eng.Remote Sens., 69*(6), 647-664. doi:10.14358/PERS.69.6.647

Pinty, B., & Verstraete, M. M. (1992). GEMI: A non-linear index to monitor global vegetation from satellites. *Vegetatio, 101*(1), 15-20. doi:10.1007/BF00031911

Prescott, B., & Mclean, G. F. (1997). Line- based correction of radial lens distortion. *Graphical Models and Image Processing, 59*(1), 39-47. doi:10.1006/gmip.1996.0407

Primicerio, J., Di Gennaro, S., Fiorillo, E., Genesio, L., Lugato, E., Matese, A., & Vaccari, F. (2012a). A flexible unmanned aerial vehicle for precision agriculture. *Precision Agriculture, 13*(4), 517.

Primicerio, J., Di Gennaro, S., Fiorillo, E., Genesio, L., Lugato, E., Matese, A., & Vaccari, F. (2012b). A flexible unmanned aerial vehicle for precision agriculture. *Precision Agriculture; an International Journal on Advances in Precision Agriculture, 13*(4), 517-523. doi:10.1007/s11119-012-9257-6

Qi, J., Chehbouni, A., Huete, A. R., Kerr, Y. H., & Sorooshian, S. (1994). A modified soil adjusted vegetation index. *Remote Sensing of Environment, 48*(2), 119-126. doi:10.1016/0034-4257(94)90134-1

Ren, H., & Zhou, G. (2014). Determination of green aboveground biomass in desert steppe using litter- soil-adjusted vegetation index. *European Journal of Remote Sensing, 47*(1), 611-625. doi:10.5721/EuJRS20144734

Ribeiro, I. O., Andreoli, R. V., Kayano, M. T., de Sousa, T. R., Medeiros, A. S., Guimarães, P. C., . . . de Souza, R. A. F. (2018). Impact of the biomass burning on methane variability during dry years in the amazon measured from an aircraft and the AIRS sensor. *Science of the Total Environment, 624*, 509-516. doi:10.1016/j.scitotenv.2017.12.147

Rodriguez, D., Fitzgerald, G., Belford, R., & Christensen, L. (2006). Detection of nitrogen deficiency in wheat from spectral reflectance indices and basic crop eco-physiological concepts. *Australian Journal of Agricultural Research; Aust.J.Agric.Res., 57*(7), 781-789. doi:10.1071/AR05361

Rodriguez-Moreno, F., Kren, J., Zemek, F., Novak, J., Lukas, V., & Pikl, M. (2017). Advantage of multispectral imaging with sub-centimeter resolution in precision agriculture: Generalization of training for supervised classification. *Precision Agriculture; an International Journal on Advances in Precision Agriculture, 18*(4), 615-634. doi:10.1007/s11119-016-9478-1

Rodríguez-Pérez, J. R., Riaño, D., Ustin, S., Carlisle, E., & Smart, D. R. (2007). Evaluation of hyperspectral reflectance indexes to detect grapevine water status in vineyards. *American Journal of Enology and Viticulture, 58*(3), 302-317.

Rondeaux, G., Steven, M., & Baret, F. (1996). Optimization of soil-adjusted vegetation indices. *Remote Sensing of Environment, 55*(2), 95-107. doi:10.1016/0034-4257(95)00186-7

Roujean, J. -., & Breon, F. -. (1995). Estimating PAR absorbed by vegetation from bidirectional reflectance measurements. *Remote Sensing of Environment, 51*(3), 375-384. doi:10.1016/0034-4257(94)00114-3

Rouse, J., Haas, R. H., Schell, J. A., Deering, D. W., & Harlan, J. C. (1974). *Monitoring the vernal advancement and retrogradation (greenwave effect) of natural vegetation.* (Technical Report No. 3). Remote Sensing Center, Texas A&M, College Station, TX: Texas A&M. Retrieved from NASA

Roy, K. W., Rupe, J. C., Hershman, D. E., & Abney, T. S. (1997). Sudden death syndrome of soybean. *Plant Disease, 81*(10), 1100-1111.

Rubio, E., Caselles, V., & Badenas, C. (1997). Emissivity measurements of several soils and vegetation types in the 8– 14, μm wave band: Analysis of two field methods. *Remote Sensing of Environment, 59*(3), 490-521. doi:10.1016/S0034-4257(96)00123-X

Salami, E., Barrado, C., & Pastor, E. (2014). UAV flight experiments applied to the remote sensing of vegetated areas. *Remote Sensing, 6*(11), 11051-11081. doi:10.3390/rs61111051

Sankaran, S., Khot, L. R., & Carter, A. H. (2015). Field-based crop phenotyping: Multispectral aerial imaging for evaluation of winter wheat emergence and spring stand. *Computers and Electronics in Agriculture, 118*, 372-379. doi:10.1016/j.compag.2015.09.001

Sankaran, S., Mishra, A., Ehsani, R., & Davis, C. (2010). A review of advanced techniques for detecting plant diseases. *Computers and Electronics in Agriculture, 72*(1), 1-13. doi:10.1016/j.compag.2010.02.007

Schmidt, C. (2007). *SIUC method of SDS scoring* Southern Illinois University Carbondale.

Sepulcre-Cantó, G., Gellens-Meulenberghs, F., Arboleda, A., Duveiller, G., De Wit, A., Eerens, H., . . . Defourny, P. (2013). Estimating crop- specific evapotranspiration using remote-sensing imagery at various spatial resolutions for improving crop growth modelling. *International Journal of Remote Sensing, 34*(9-10), 3274-3288. doi:10.1080/01431161.2012.716911

Sepulcre-Cantó, G., Zarco-Tejada, P. J., Jiménez-Muñoz, J. C., Sobrino, J. A., Soriano, M. A., Fereres, E., . . . Pastor, M. (2007). Monitoring yield and fruit quality parameters in open-canopy tree crops under water stress. implications for ASTER. *Remote Sensing of Environment, 107*(3), 455-470. doi:10.1016/j.rse.2006.09.014

Serrano, L., Peñuelas, J., & Ustin, S. L. (2002). Remote sensing of nitrogen and lignin in mediterranean vegetation from AVIRIS data: Decomposing biochemical from structural signals. *Remote Sensing of Environment, 81*(2), 355-364. doi:10.1016/S0034-4257(02)00011-1

Shrivastava, S., Singh, S. K., & Hooda, D. S. (2015). Color sensing and image processing-based automatic soybean plant foliar disease severity detection and estimation. *Multimedia Tools and Applications, 74*(24), 11467-11484. doi:10.1007/s11042-014-2239-0

Sims, D. A., & Gamon, J. A. (2002). Relationships between leaf pigment content and spectral reflectance across a wide range of species, leaf structures and developmental stages. *Remote Sensing of Environment, 81*(2), 337-354. doi:10.1016/S0034-4257(02)00010-X

Singh, M., Cheyne, S. M., & Ehlers Smith, D. A. (2018). How conspecific primates use their habitats: Surviving in an anthropogenically-disturbed forest in central Kalimantan, Indonesia. *Ecological Indicators, 87*, 167-177. doi:10.1016/j.ecolind.2017.12.041

Slaton, M. R., Raymond Hunt, E., & Smith, W. K. (2001). Estimating near- infrared leaf reflectance from leaf structural characteristics. *American Journal of Botany, 88*(2), 278-284. doi:10.2307/2657019

Smith, G. M., & Milton, E. J. (1999). The use of the empirical line method to calibrate remotely sensed data to reflectance. *International Journal of Remote Sensing, 20*(13), 2653-2662. doi:10.1080/014311699211994

Sobel, I. (1974). On calibrating computer controlled cameras for perceiving 3-D scenes. *Artificial Intelligence, 5*(2), 185-198. doi:10.1016/0004-3702(74)90029-0

Suárez, L., Zarco-Tejada, P. J., Sepulcre-Cantó, G., Pérez-Priego, O., Miller, J. R., Jiménez-Muñoz, J. C., & Sobrino, J. (2008). Assessing canopy PRI for water stress detection with diurnal airborne imagery. *Remote Sensing of Environment, 112*(2), 560-575. doi:https://doi.org/10.1016/j.rse.2007.05.009

Sutherland, I. E. (1974). Three-dimensional data input by tablet. *Proceedings of the IEEE, 62*(4), 453-461. doi:10.1109/PROC.1974.9449

Swain, K. C., Jayasuriya, H. P., & Salokhe, V. M. (2007). Suitability of low- altitude remote sensing images for estimating nitrogen treatment variations in rice cropping for precision agriculture adoption. *Journal of Applied Remote Sensing, 1*(1) doi:10.1117/1.2824287

Tamouridou, A. A., Alexandridis, T. K., Pantazi, X. E., Lagopodi, A. L., Kashefi, J., Kasampalis, D., . . . Moshou, D. (2017). Application of multilayer perceptron with automatic relevance determination on weed mapping using UAV multispectral imagery. *Sensors (Switzerland), 17*(10) doi:10.3390/s17102307

Tang, E., Hill, C. B., & Hartman, G. L. (2010). Carbon utilization profiles of fusarium virguliforme isolates. *Canadian Journal of Microbiology, 56*(12), 979-986. doi:10.1139/W10-085

Themistocleous, K., Papadavid, G., Christoforou, M., Agapiou, A., Andreou, K., Tsaltas, D., & Hadjimitsis, D. G. (2014). Use of remote sensing and UAV for the management of degraded ecosystems: The case study of overgrazing in randi forest, cyprus. Paper presented at the *2nd International Conference on Remote Sensing and Geoinformation of the Environment, RSCy 2014, April 7, 2014 - April 10, , 9229* et al.; Euro-agriwot; European Cooperation in Science and Technology (COST); Geosystems Hellas; Intergraph; Li-Cor. doi:10.1117/12.2069515 Retrieved from http://dx.doi.org/10.1117/12.2069515

Tilling, A. K., O'Leary, G. J., Ferwerda, J. G., Jones, S. D., Fitzgerald, G. J., Rodriguez, D., & Belford, R. (2007). Remote sensing of nitrogen and water stress in wheat. *Field Crops Research, 104*(1–3), 77-85. doi:https://doi.org/10.1016/j.fcr.2007.03.023

Tsai, R. (1987). A versatile camera calibration technique for high- accuracy 3D machine vision metrology using off-the-shelf TV cameras and lenses. *Robotics and Automation, IEEE Journal of, 3*(4), 323-344. doi:10.1109/JRA.1987.1087109

Tucker, C. J., Vanpraet, C. L., Sharman, M. J., & Van Ittersum, G. (1985). Satellite remote sensing of total herbaceous biomass production in the senegalese sahel: 1980– 1984. *Remote Sensing of Environment, 17*(3), 233-249. doi:10.1016/0034-4257(85)90097-5

Tucker, C. J. (1979). Red and photographic infrared linear combinations for monitoring vegetation. *Remote Sensing of Environment, 8*(2), 127-150. doi:10.1016/0034-4257(79)90013-0

Turner, D., Lucieer, A., Malenovsky, Z., King, D., & Robinson, S. (2014). Spatial co-registration of ultra-high resolution visible, multispectral and thermal images acquired with a micro-UAV over Antarctic moss beds. *Remote Sensing, 6*(5), 4003-4024. doi:10.3390/rs6054003

U.S. Geological Survey. (2017). Landsat 7. Retrieved from https://landsat.usgs.gov/landsat-7

Vina, A., Gitelson, A. A., Rundquist, D. C., Keydan, G., Leavitt, B., & Schepers, J. (2004). Remote sensing - monitoring maize (zea mays L.) phenology with remote sensing. *Agronomy Journal; Agron.J., 96*(4), 1139-1147.

Vincent, R. K. (1972). (1972). An ERTS multispectral scanner experiment for mapping iron compounds. Paper presented at the *Proc. 8th International Symposium on Remote Sensing of Environment,* Ann Arbor, Michigan. 1239-1239-1247.

Vincini, M., Frazzi, E., & D'Alessio, P. (2008). A broad- band leaf chlorophyll vegetation index at the canopy scale. *Precision Agriculture; an International Journal on Advances in Precision Agriculture, 9*(5), 303-319. doi:10.1007/s11119-008-9075-z

Wang, C., Li, W., Chen, S., Li, D., Wang, D., & Liu, J. (2018). The spatial and temporal variation of total suspended solid concentration in pearl river estuary during 1987–2015 based on remote sensing. *Science of the Total Environment, 618*, 1125-1138. doi:10.1016/j.scitotenv.2017.09.196

Wang, J., Shi, F., Zhang, J., & Liu, Y. (2006). A new calibration model and method of camera lens distortion. Paper presented at the *IEEE International Conference on Intelligent Robots and Systems,* 5713-5718. doi:10.1109/IROS.2006.282376

Wang, L., & Qu, J. J. (2007). NMDI: A normalized multi- band drought index for monitoring soil and vegetation moisture with satellite remote sensing. *Geophysical Research Letters, 34*(20), n/a-n/a. doi:10.1029/2007GL031021

Wang, X., Yang, W., Wheaton, A., Cooley, N., & Moran, B. (2010). Automated canopy temperature estimation via infrared thermography: A first step towards automated plant water stress monitoring. *Computers and Electronics in Agriculture, 73*(1), 74-83. doi:10.1016/j.compag.2010.04.007

Westphal, A., Xing, L., Abney, T. S., & Shaner, G. (2006). Diseases of soybean: Sudden death syndrome. *Purdue Extension BP-58-W,* (4)

Wooster, M. J., Roberts, G., Smith, A. M. S., Johnston, J., Freeborn, P., Amici, S., . . . Hudak, A. T. (2013). *Thermal remote sensing of active vegetation fires and biomass burning events* doi:10.1007/978-94-007-6639-6_18

Wrather, J. A., & Koenning, S. R. (2006). Estimates of disease effects on soybean yields in the united states 2003 to 2005. *Journal of Nematology, 38*(2), 173-180.

Wu, W. (2014). The generalized difference vegetation index (GDVI) for dryland characterization. *Remote Sensing, 6*(2), 1211-1233. doi:10.3390/rs6021211

Xia, L. (1994). A two-axis adjusted vegetation index (TWVI). *International Journal of Remote Sensing, 15*(7), 1447-1458. doi:10.1080/01431169408954176

Xing, L., & Westphal, A. (2009). Effects of crop rotation of soybean with corn on severity of sudden death syndrome and population densities of heterodera glycines in naturally infested soil. *Field Crops Research, 112*(1), 107-117. doi:10.1016/j.fcr.2009.02.008

Xu, H. R., Ying, Y. B., Fu, X. P., & Zhu, S. P. (2007). Near-infrared spectroscopy in detecting leaf miner damage on tomato leaf. *Biosystems Engineering, 96*(4), 447-454. doi:10.1016/j.biosystemseng.2007.01.008

Yakimovsky, Y., & Cunningham, R. (1978). A system for extracting three-dimensional measurements from a stereo pair of TV cameras. *Computer Graphics and Image Processing, 7*(2), 195-210. doi:10.1016/0146-664X(78)90112-0

Yang, C., Everitt, J. H., & Fernandez, C. J. (2010). *Comparison of airborne multispectral and hyperspectral imagery for mapping cotton root rot* doi:http://dx.doi.org/10.1016/j.biosystemseng.2010.07.011

Yuanjie Zheng, S., Lin, C., Kambhamettu, C., Jingyi Yu, C., & Sing, B. K. (2009). Single- image vignetting correction. *Pattern Analysis and Machine Intelligence, IEEE Transactions on, 31*(12), 2243-2256. doi:10.1109/TPAMI.2008.263

Zarco-Tejada, P., Ustin, S. L., & Whiting, M. L. (2005). Temporal and spatial relationships between within-field yield variability in cotton and high- spatial hyperspectral remote sensing imagery. *Agronomy Journal, 97*(3), 641-653. doi:10.2134/agronj2003.0257

Zarco-Tejada, P. J., Berjón, A., López-Lozano, R., Miller, J. R., Martín, P., Cachorro, V., . . . De Frutos, A. (2005). Assessing vineyard condition with hyperspectral indices: Leaf and canopy reflectance simulation in a row-structured discontinuous canopy. *Remote Sensing of Environment, 99*(3), 271-287. doi:10.1016/j.rse.2005.09.002

Zarco-Tejada, P. J., Miller, J. R., Morales, A., Berjón, A., & Agüera, J. (2004). Hyperspectral indices and model simulation for chlorophyll estimation in open-canopy tree crops. *Remote Sensing of Environment, 90*(4), 463-476. doi:10.1016/j.rse.2004.01.017

Zhang, C., & Kovacs, J. M. (2012). The application of small unmanned aerial systems for precision agriculture: A review. *Precision Agriculture, 13*(6), 693-712. doi:10.1007/s11119-012-9274-5

Zhang, H., Lan, Y., Suh, C. P. -., Westbrook, J., Clint Hoffmann, W., Yang, C., & Huang, Y. (2013). Fusion of remotely sensed data from airborne and ground-based sensors to enhance

detection of cotton plants. *Computers and Electronics in Agriculture, 93*, 55-59. doi:10.1016/j.compag.2013.02.001

Zhang, H., Wang, D., Ayars, J. E., & Phene, C. J. (2017). Biophysical response of young pomegranate trees to surface and sub-surface drip irrigation and deficit irrigation. *Irrigation Science, 35*(5), 425-435. doi:10.1007/s00271-017-0551-y

Zhao, C., Liu, L., Wang, J., Huang, W., Song, X., & Li, C. (2005). Predicting grain protein content of winter wheat using remote sensing data based on nitrogen status and water stress. *International Journal of Applied Earth Observations and Geoinformation, 7*(1), 1-9. doi:10.1016/j.jag.2004.10.002

Zhu, G., Ju, W., J, M. C., & Liu, Y.A novel moisture adjusted vegetation index (MAVI) to reduce background reflectance and topographical effects on LAI retrieval. *PLoS ONE, 9*(7), e102560. doi:10.1371/journal.pone.0102560

Appendix A - Vegetative Index Table

Table A.1 Vegetative Index Table

Index	Full Name	Formula	Bands Used	Reference
ARVI	Atmospherically Resistant Vegetation Index	$\frac{NIR-RB}{NIR-RB}$ $RB = Red - \gamma(Blue - Red)$	Blue/Red/NIR	(Kaufman & Tanré, 1992)
ARI	Anthocyanin Reflectance Index	$\frac{1}{R_{550}} - \frac{1}{R_{700}}$	Green/Red	(A. A. Gitelson et al., 2001)
BNDVI	Blue Normalized Difference Vegetation Index	$\frac{NIR - Blue}{NIR + Blue}$	Blue/NIR	
CAI	Cellulose Absorption Index	$0.5(R_{2.0} + R_{2.2}) - R_{2.1}$	NIR	(Nagler et al., 2000)
CAR	Chlorophyll Absorption Ratio	$\frac{(R_{700} - R_{500})670 + R_{670} + \left(R_{550} - \left((R_{700} - R_{500})670\right)550\right)}{\sqrt{((R_{700} - R_{500})670)^2}}$	Green/Red	(Broge & Leblanc, 2001)
CAR1	Chlorophyll Absorption Ratio	$CAR * \frac{R_{700}}{R_{670}}$	Green/Red	(Broge & Leblanc, 2001; M. S. Kim et al., 1994)
CCCI	Canopy Chlorophyll Content Index	$\frac{NDRE}{NDVI}$	Red/NIR	(Barnes et al., 2000; Rodriguez et al., 2006)
CI	Chlorophyll Index	$\frac{R_1}{R_2} - 1$	Green/NIR	(A. A. Gitelson et al., 2005)
CI-G	Chlorophyll Index-Green	$\frac{NIR}{Green} - 1$	Green/NIR	(A. A. Gitelson et al., 2003)
CI-RE	Chlorophyll Index Red Edge	$\frac{NIR}{RE} - 1$	NIR	(A. A. Gitelson et al., 2003)
CLSI	*Cercospora* Leaf Spot Index	$\frac{R_{698} - R_{570}}{R_{698} + R_{570}} + R_{734}$	Green/Red/NIR	(A. -. Mahlein et al., 2013)
CRI	Carotenoid Reflectance Index	$\frac{1}{R_{510}} - \frac{1}{R_{550}}$	Green	(A. A. Gitelson et al., 2002)
CVI	Chlorophyll Vegetation Index	$NIR\frac{Red}{Green^2}$	Green/Red/NIR	(Vincini et al., 2008)
DRRI	Difference Reflectance Ratio Index	$\frac{R_1 - R_2}{R_3}$	Any	(Ali et al., 2017)

DVI	Difference Vegetation Index	$R_1 - R_2$	Any	(Jordan, 1969)
EVI	Enhanced Vegetation Index	$2.5\frac{(NIR - Red)}{(NIR + 6Red - 7.5Blue + 1)}$	Blue/Red/NIR	(A. Huete et al., 2002; A. R. Huete et al., 1997; H. Q. Liu & Huete, 1995)
GDVI	Generalized Difference Vegetation Index	$\frac{R_{NIR}^n - R_{Red}^n}{R_{NIR}^n + R_{Red}^n}$	Red/NIR	(Wu, 2014)
GESAVI	Generalized Soil Adjusted Vegetation Index	$\frac{NIR - a * Red - b}{Red + Z}$	Red/NIR	(Gilabert et al., 2002)
GEMI	Global Environmental Monitoring Vegetation Index	$\eta(1 - 0.25\eta) - \frac{(Red - 0.125)}{(1 - Red)}$	Red/NIR	(Pinty & Verstraete, 1992)
GI	Greenness Index	$\frac{R_{550}}{R_{670}}$	Green/Red	(P. J. Zarco-Tejada et al., 2004; P. J. Zarco-Tejada et al., 2005)
GLI	Green Leaf Index	$\frac{2Green - Red - Blue}{2Green + Red + Blue}$	Blue/Green/Red	(Louhaichi et al., 2001)
GNDVI	Green Normalized Difference Vegetation Index	$\frac{NIR - Green}{NIR + Green}$	Green/NIR	(A. A. Gitelson et al., 1996; A. A. Gitelson & Merzlyak, 1998)
GVMI	Global Vegetation Moisture Index	$\frac{(NIR + 0.1) - (SWIR + 0.02)}{(NIR + 0.1) + (SWIR + 0.02)}$	NIR/SWIR	(Ceccato et al., 2002)
LCAI	Ligno-Cellulose Absorption Index	$100((ASTER6 - ASTER5) + (ASTER6 - ASTER8))$	NIR	(Daughtry et al., 2005)
LSAVI	Litter Soil Adjusted Vegetation Index	$\frac{1.5(1+L*CAI)(NIR-Red)}{NIR+Red+0.5+L*CAI}$ $CAI = 100(\frac{R_{2000}+R_{2200}}{2} - R_{2100})$	NIR	(Ren & Zhou, 2014)
MAVI	Moisture Adjusted Vegetation Index	$\frac{NIR - Red}{NIR + red + SWIR}$	Red/NIR/SWIR	(Zhu, Ju, J, & Liu,)
MCARI	Modified Chlorophyll Absorption Reflectance Index	$((R_{700} - R_{670}) - 0.2(R_{700} - R_{500}))\frac{R_{700}}{R_{670}}$	Green/Red/NIR	(Daughtry et al., 2000)
MCARI/MTVI2		$\frac{MCARI}{MTVI2}$	Green/Red/NIR	(Eitel et al., 2007; Haboudane et al., 2008)
MCARI1	Modified Chlorophyll Absorption in Reflectance	$1.2(2.5(R_{800} - R_{670}) - 1.3(R_{800} - R_{550}))$	Green/Red/NIR	(Haboudane et al., 2004)
MCARI2	Modified Chlorophyll Absorption in Reflectance	$\frac{1.2(2.5(R_{800} - R_{670}) - 1.3(R_{800} - R_{550}))}{\sqrt{(2R_{800} + 1)^2 - 6(R_{800} - 5R_{670}) - 0.5}}$	Green/Red/NIR	(Haboudane et al., 2004)

mND	Modified Normalized Difference	$\frac{R_{935} - R_{715}}{R_{935} + R_{715} - R_{405}}$	Blue/NIR	(Le Maire et al., 2008)
MNDVI	Modified Normalized Difference Vegetation Index	$NDVI * \frac{(SWIR_{max} - SWIR)}{(SWIR_{max} - SWIR_{\min})}$	Red/NIR/SWIR	(Nemani et al., 1993)
MNLI	Modified Non-Linear Vegetation Index	$(1 + L)(\frac{NIR^2 - Red}{NIR^2 + Red + L})$	Red/NIR	(Gong et al., 2003)
MSAVI	Improved SAVI	$0.5(2NIR + 1 - \sqrt{(2NIR + 1)^2 - 8(NIR - Red)}$	Red/NIR	(Qi et al., 1994)
mSR	Modified Simple Ratio	$\frac{R_{970} - R_{405}}{R_{715} - R_{405}}$	Blue/NIR	(Le Maire et al., 2008)
MSR	Modified Spectral Ratio	$\frac{R_{750} - R_{445}}{R_{705} + R_{445}}$	Blue/NIR	(Sims & Gamon, 2002)
mSR2	Modified Simple Ratio 2	$\frac{\frac{R_{800}}{R_{670}} - 1}{\sqrt{\left(R_{800}/R_{670}\right) + 1}}$	Red/NIR	(Chen, 1996)
mSR3	Modified Simple Ratio Index 3	$\frac{R_1 - R_2}{R_1 - R_3}$	Any	(Datt, 1999)
MSRpi	Modified Spectral Ratio Planar Index	$Calibrated\ index\ using\ mSR\ as\ a\ function\ of\ NDVI$	Blue/Red/NIR	(Rodriguez et al., 2006)
MTCI	MERIS Total Chlorophyll Index	$\frac{R_{750} - R_{710}}{R_{710} + R_{680}}$	Red/NIR	(Dash & Curran, 2004)
MTVI2	Second Modified Triangular Vegetation Index	$1.5(2.5(NIR - Red) - \frac{2.5(Red - Green)}{\sqrt{(2NIR + 1)^2 - 6NIR - 5\sqrt{Red} - 0.5}})$	Green/Red/NIR	(Haboudane et al., 2004)
MTVI3	Modified Triangular Vegetation Index	$1.2(1.2(R_{800} - R_{550}) - 2.5(R_{670} - R_{550}))$	Green/Red/NIR	(Rodríguez-Pérez et al., 2007)
NDLI	Normalized Difference Lignin Index	$\frac{\log(\frac{1}{R_{1754}}) - \log(\frac{1}{R_{1680}})}{\log\left(\frac{1}{R_{1754}}\right) + \log(\frac{1}{R_{1680}})}$	NIR	(Serrano et al., 2002)
NDNI	Normalized Difference Nitrogen Index	$\frac{\log(\frac{1}{R_{1510}}) - \log(\frac{1}{R_{1680}})}{\log\left(\frac{1}{R_{1510}}\right) + \log(\frac{1}{R_{1680}})}$	NIR	(Serrano et al., 2002)

NDREI	Normalized Difference Red Edge Index	$\frac{R_{790} - R_{720}}{R_{790} + R_{720}}$	NIR	(Barnes et al., 2000; A. Gitelson & Merzlyak, 1994; Rodriguez et al., 2006)
NDVI	Normalized Difference Vegetation Index	$\frac{NIR - Red}{NIR + Red}$	Red/NIR	(Rouse et al., 1974)
NGRDI	Normalized Green Red Difference Index	$\frac{Green - Red}{Green + Red}$	Green/Red	(C. J. Tucker, 1979)
NLI	Non-linear Vegetation Index	$\frac{NIR^2 - Red}{NIR^2 + Red}$	Red/NIR	(Goel & Qin, 1994)
NMDI	A Normalized Multi-Band Drought Index	$\frac{R_{860} - (R_{1640} - R_{2130})}{R_{860} + (R_{1640} - R_{2130})}$	NIR	(L. Wang & Qu, 2007)
OSAVI	Optimized Soil-Adjusted Vegetation Index	$(1.16)\frac{NIR - Red}{NIR + Red + 0.16}$	Red/NIR	(Rondeaux et al., 1996)
PI	Pigment Index	$BNDVI - GNDVI$	Blue/Green/NIR	(KSURF Invention Disclosure No. 2016-010, 2016)
PRI	Photochemical Reflectance Index	$\frac{R_{530} - R_{570}}{R_{530} + R_{570}}$	Green	(Fuentes & G., 2001; Gamon et al., 1992; GAMON & SURFUS, 1999)
PSSRa	Pigment Specific Simple Ratio a	$\frac{R_{800}}{R_{680}}$	Red/NIR	(Blackburn, 1998)
PSSRb	Pigment Specific Simple Ratio b	$\frac{R_{800}}{R_{635}}$	Red/NIR	(Blackburn, 1998)
PVI	Perpendicular Vegetation Index	$\frac{1}{\sqrt{a^2 + 1}}(NIR - a * Red - b)$	Red/NIR	(Baret & Guyot, 1991)
RDVI	Re-normalized Difference Vegetation Index	$\frac{R_{800} - R_{670}}{\sqrt{R_{800} + R_{670}}}$	Red/NIR	(Roujean & Breon, 1995)
RSR	Reduced Simple Ratio	$SR * \frac{(SWIR_{max} - SWIR)}{(SWIR_{max} - SWIR_{\min})}$	Red/NIR/SWIR	(Brown et al., 2000)
RVI	Ratio Vegetation Index	$\frac{NIR}{Red}$	Red/NIR	(Jordan, 1969; Pearson & Miller, 1972)
RVSI	Red-edge Vegetation Stress Index	$\frac{R_{714} + R_{752}}{2 - R_{733}}$	NIR	(Naidu et al., 2009)
SAVI	Soil Adjusted Vegetation Index	$(1.5)\frac{(NIR - Red)}{(NIR + Red + 0.5)}$	Red/NIR	(A. R. Huete, 1988)

SAVI2	Soil Adjusted Vegetation Index 2	$\frac{NIR}{Red + \frac{a}{b}}$	Red/NIR	(Major et al., 1990)
SARVI2	Soil and Atmosphere Resistant Vegetation Index	$\frac{25(NIR - Red)}{1 + NIR + 6Red - 7.5Blue}$	Blue/Red/NIR	(A. R. Huete et al., 1997)
SIPI	Structure Insensitive Pigment Index	$\frac{R_{800} - R_{455}}{R_{800} + R_{680}}$	Blue/Red/NIR	(Penuelas et al., 1995)
SLAVI	Specific Leaf Area Vegetation Index	$\frac{NIR}{Red + MIR2}$	Red/NIR/MIR	(Lymburner, Beggs, & Jacobson, 2000)
SRI or SR	Simple Ratio Index	$\frac{R_{800}}{R_{550}}$ or $\frac{NIR}{Red}$	Green/Red/NIR	(Jordan, 1969; Pearson & Miller, 1972)
TCARI	Transformed Chlorophyll Absorption in Reflectance Index	$3((R_{700} - R_{670}) - 0.2(R_{700} - R_{550}))\frac{R_{700}}{R_{670}}$	Green/Red	(Haboudane et al., 2002)
TCARI/OSAVI		$TCARI/OSAVI$	Green/Red/NIR	(Haboudane et al., 2002; P. J. Zarco-Tejada et al., 2004)
TCI	Triangular Chlorophyll Index	$1.2(R_{700} - R_{550}) - 1.5(R_{670} - R_{550}) * \sqrt{\frac{R_{700}}{R_{670}}}$	Green/Red/NIR	(Haboudane et al., 2008)
TGI	Triangular Greenness Index	$-0.5((\lambda r - \lambda b)(Red - Green) - (\lambda r - \lambda g)(Red - Blue))$	Blue/Green/Red	(Hunt Jr. et al., 2013; Hunt et al., 2011)
TSAVI	Transformed Soil Adjusted Vegetation Index	$\frac{\alpha(NIR - \alpha Red - b)}{Red + \alpha(NIR - b) + 0.08(1 + \alpha^2)}$	Red/NIR	(Baret et al., 1989; Baret & Guyot, 1991)
TVI	Transformed Vegetation Index	$\sqrt{\frac{NIR - Red}{NIR + Red} + 0.5}$	Red/NIR	(Deering et al., 1975)
TVI	Triangular Vegetation Index	$0.5(102(NIR - Green) - 200(Red - Green))$	Green/Red/NIR	(Broge & Leblanc, 2001)
TWVI	Two-axis Vegetation Index	$(1 + L)\frac{(NIR - Red - \Delta)}{(NIR + Red + L)}$	Red/NIR	(Xia, 1994)
VARI	Visible Atmospherically Resistant Index	$\frac{Green - Red}{Green + Red - Blue}$	Blue/Green/Red	(A. A. Gitelson et al., 2002; Naidu et al., 2009)
WDRVI	Wide Dynamic Range Vegetation Index	$\frac{a * NIR - Red}{a * NIR + Red}$	Red/NIR	(A. A. Gitelson, 2004)
WDVI	Weighted Difference Vegetation Index	$NIR - a * Red$	Red/NIR	(Clevers, 1991; Clevers & Verhoef, 1993)

I_{WB}	Water Band Index	$\frac{R_{950}}{R_{900}}$	NIR	(Xu, Ying, Fu, & Zhu, 2007)
WI	Water Index	$\frac{R_{900}}{R_{970}}$	NIR	(Naidu et al., 2009)

Appendix B - Preflight Checklist

Materials:

- Pilot's license – at least one person MUST have a license
- Phantom 4 Pro
    - Batteries (3)
    - Propellers (2 sets)
    - Plane
    - Remote
    - iPad or equivalent operating screen
    - iPad cable (or equivalent)
    - USB to mini USB converter
    - Registration card
- IRIS+
    - Plane
    - Remote
    - AA batteries (8 minimum)
    - Batteries (5.1 Ah, 6 max and/or 5.2 Ah, 2 max)
    - Registration card
- Matrice
    - Plane
    - Propellers (2 sets)
    - Batteries (6)
    - Remote
    - iPad or equivalent operating system
    - iPad cable (or equivalent)
    - All mounting materials
    - Registration card
- X-8
    - Plane
    - Remote
    - AA batteries (8 minimum)
    - Batteries
    - Registration card
- Cameras
    - FLIR VUE Pro R
    - α5100
    - GoPro
- Tri-color panels or thermal calibration station
    - Black panels
    - Grey panel
    - White panel
    - Wet bath
    - Humidity sensor
    - Gallon of water

    - Stand
    - myRIO
    - Batteries
    - Flash drive
    - Mounting hardware
    - Computer cable
- IR temperature gun
- ID Strips
- Campbell Scientific weather station
    - Wind vane
    - 12 V battery
- Laptop
- iPad
- Topcon (if ID points have not been marked)
    - Base
    - Rover
    - Base stand
    - Mounting pole
    - Tablet
- SD cards (extra)
    - Check cameras have SD cards
- Toolbag
- Fire extinguisher
- Sunscreen
- Hat
- Water bottle
- Lunch
- Notebook
- Pen/Pencil

<u>Before leaving:</u>

- Check the weather
- Check airspace make sure no restrictions are present (temporary restrictions may pop up)
- Get permission if necessary (contact ATC)
- Check DJI for updates (Matrice and Phantom)
    - **Do this the night before**
    - You will not be able to fly if updates are present
- Ensure all batteries are not damaged and have a full charge
    - Check the day before, it takes time to charge them
- SD cards are emptied and ready for new images
- Laptop battery charged
- iPad charged
- Correct apps downloaded and ready
- Offline maps ready

Arrival at the field:

- Determine flight area
- Check for high wires or other obstruction to flight
- Place ID strips
    - Each should have a different shape
    - Use Topcon GPS to gather waypoints
- Set out panels
- Set up each weather station
    - Begin collecting data before the flights
- Select landing zone

Before **EACH** flight:

- Ensure no personnel who are not directly participating are in the area
- Propellers are tight and in good condition, no nicks, cracks or warping of the blades should be present
- Aircraft is in good condition, no exposed wiring or body defects
- Check batteries are good, no cracks in body/no puffiness
- Batteries are hooked up correctly
- New, fully charged battery has been connected
- SD cards in camera/plane – space for images
- Remote battery level is good
- Camera battery level is good
- Camera secured
- Camera lens clean
- Remote connected to UAS
- Gimbal connected and operational
- Camera turned on
- Mission uploaded to UAS
- All locks removed
  Take-off and landing locations are clear

Appendix C - Post Flight Checklist

After **EACH** flight

- Ensure the system is disarmed before approaching
- Ensure no damage occurred during flight
- Remove battery
    - Check battery for damage, puffing, or cracks in the casing
    - Place it in an area where you will not confuse it with fully charged batteries

After all flights

- Remove propellers
- Remove all batteries
- Remove cameras
- Pack sUAS into cases, ensure all parts are present
- Pack cameras securely into the case
- Pick up weather stations, panels, and ID Strips
- Ensure everything is packed securely into the car

Appendix D - Lithium Battery Disposal

1. Use battery charger to discharge battery as much as possible.
2. Cut connectors (these are good to have on hand and can be used for replacements and repairs)
    a. Cut the leads at different lengths to avoid contact
3. Obtain a plastic five-gallon bucket. Make sure the bucket is non-conductive like ABS plastic!
    a. **Take EVERYTHING outside before continuing!**
4. Mix the 3 to 1 salt mixture in the bucket
    a. Make sure there is enough liquid to fully submerge the battery pack
    b. If you are using a coarse salt such as driveway or water softener salt, crush the granules first or allow time for the salt to dissolve enough to create an adequate salt solution. The solution should be VERY salty to taste
5. Snip the battery connector off of the end of the main leads
    a. **Cut the leads at different lengths to avoid contact**
6. Put on a pair of thick gloves and carefully cut a small slit in each foil cell pack on opposite sides and away from each other to allow electrical conductivity with the cell plates in the salt brine
    a. **BE SURE NO POLYMER COMES IN CONTACT WITH ANOTHER CELL OR A VERY HOT FIRE OR EXPLOSION WILL ENSUE!**
7. Make sure your salt-water bucket is **OUTSIDE** and away from anything flammable.
8. Carefully place the battery in your salt solution and let it sit for 24 hours. Stay clear of the bucket during this process. Although it is tempting to stand over top of it and stare, you could be injured if the pack bursts.
9. Expect some "fizzing" or a little foaming during the discharge. After 24 hours, the pack should be completely dead. Test it carefully with a multimeter or voltmeter if possible to verify that it reads zero volts.
10. Place battery in ammo box (Seaton 1057A) or give to Jon Zeller then contact campus hazardous waste disposal.
    a. http://www.k-state.edu/safety/environmental/hazardous-waste/